REVIEWS OF MODERN PHYSICS, VOLUME 79, JANUARY–MARCH 2007

Magnetic microtraps for ultracold atoms

József Fortágh and Claus Zimmermann

Physikalisches Institut, Universität Tübingen, Auf der Morgenstelle 14, 72076 Tübingen, Germany

(Published 1 February 2007)

Trapping and manipulating ultracold atoms and degenerate quantum gases in magnetic micropotentials is reviewed. Starting with a comprehensive description of the basic concepts and fabrication techniques of microtraps together with early pioneering experiments, emphasis is placed on current experiments on degenerate quantum gases. This includes the loading of quantum gases in microtraps, coherent manipulation, and transport of condensates together with recently reported experiments on matter-wave interferometry on a chip. Theoretical approaches for describing atoms in waveguides and beam splitters are briefly summarized, and, finally, the interaction between atoms and the surface of microtraps is covered in some detail.

DOI: 10.1103/RevModPhys.79.235 PACS number(s): 52.55.Lf, 39.20.+q, 39.25.+k, 03.75.Be

CONTENTS

I. INTRODUCTION

Trapping neutral particles in static magnetic fields is a well-known technique. It was first applied to neutrons (Kugler *et al.*, 1978; Paul, 1990), but since 1985 also atoms have been routinely trapped in the magnetic field of normal (Migdall *et al.*, 1985) and superconducting electromagnets (Hess *et al.*, 1987; Hijmans *et al.*, 1989). Ten years later, gases of magnetically trapped alkali-metal atoms have been cooled below the critical temperature for Bose-Einstein condensation. This Nobel Prize winning achievement started a tremendously successful new field in physics (Cornell and Wieman, 2002; Ketterle, 2002).

Magnetic traps provide potentials that act as a simple Dewar container for storing cold atoms at microkelvin temperatures and below. In addition to conventional traps made from macroscopic coils, the concept of magnetic microtraps has been introduced. These traps use miniaturized current conductors for generating the magnetic field of almost arbitrary geometry. Microtraps are in the spirit of early experiments on manipulating cold atoms with current carrying wires (Schmiedmayer, 1992), evanescent light fields (Dowling and Gea-Banacloche, 1996), and magnetic mirrors (Hinds, 1999). The initial motivation for the development of microtraps was the strong confinement that results from the miniaturization of the trap. However, by using chip technology, additional tools and devices can be integrated so that today microtraps are discussed in a far more general context. Promising areas of application include model systems for three- and one-dimensional quantum gases, disordered systems, quantum information processing with neutral atoms, integrated atom optics, matter-wave interferometry, precision force sensing, and studies of the interaction between atoms and surfaces.

The first proposal of a conservative three-dimensional magnetic trapping potential with miniaturized conductors was given by Weinstein and Libbrecht (1995). It was followed by the experimental realization of a three-dimensional microtrap based on linear conductors three years later (Fortágh, Grossman, Zimmermann, and Hänsch, 1998). A conceptually very similar trap based on permanent magnets had been demonstrated earlier in the same year (Vuletic *et al.*, 1998). Other experiments demonstrated the guiding of atoms using microscopic electromagnets (Denschlag, Cassettari, and Schmiedmayer, 1999b; Müller *et al.*, 1999; Dekker *et al.*, 2000; Key, Hughes, *et al.*, 2000) and trapping with microfabricated conductors on a chip (Reichel *et al.*, 1999; Cassettari, Hessmo, *et al.*, 2000). These and other experiments showed that steep traps with large energy separation between the bound quantum states should be possible. Highly elongated traps could be used as waveguides that carry quantized atomic matter waves in the transverse ground state similar to light waves in single-mode fibers. With atoms cooled to a few μK temperature the realization of such a scenario appeared to be feasible. Thus, the experimental challenge of the following years was the loading of ultracold gases into microtraps at temperatures and densities which are close to or even well within quantum degeneracy. This goal was achieved in 2001 in two experiments (Ott *et al.*, 2001; Hänsel, Hommelhoff, *et al.*, 2001a). Since then, the vision of integrated atom optics on a microchip has attracted an increasing number of research groups, adding new experiments and ideas to the field. Recently, degenerate Fermi gases have also been loaded into microtraps (Aubin *et al.*, 2006). Besides the realization of purely magnetic "on-chip" circuits for atomic matter waves it is also conceivable to combine magnetic microtraps with optical methods for detecting single atoms and for adding specialized potentials such as lattices, potential barriers, and single- or double-well potentials. Electrostatic forces are also discussed and have already been used to extend the tool box for designing micropotentials. Recently the first diffraction and interference experiments with Bose-Einstein condensates on a chip have been reported (Günther, Kraft, *et al.*, 2005; Shin, Sanner, *et al.*, 2005; Schumm, Hofferberth, *et al.*, 2005; Wang *et al.*, 2005; Jo *et al.*, 2006), finally making integrated atom interferometry an experimental reality. This adds to the vision of integrated "microatomics" as a new type of quantum technology.

In the last years several reviews on magnetic microtraps have been published focusing on various aspects (Hinds and Hughes, 1999; Folman *et al.*, 2002; Reichel, 2002). A special issue of the European Physical Journal, D, Vol. 35, 1–171 (2005), has also been devoted to this topic. In the present article, we give a comprehensive overview of magnetic microtraps that are generated with miniaturized current conductors. Closely related research on microtraps made from permanent magnets, electrostatic and electrodynamic traps, and integrated optical traps is not included; however, some references to these topics are given where necessary. In the following section, a basic description of magnetic microtraps is given together with various geometries that have been investigated experimentally or theoretically. These include atomic guides, beam splitters, double-well potentials, magnetic lattices, and specialized potentials such as conveyor belts and positioning systems for atomic ensembles. An overview of microfabrication techniques is given at the end of this section. Section III is devoted to theoretical work on atom guiding and beam splitting. Section IV reviews the experimental state of the art including various loading techniques for microtraps, generation of Bose-Einstein condensates and Fermi gases in microtraps, and first experiments on coherent manipulation and interferometry with matter waves on a chip. Interaction effects between ultracold atoms and the chip surface turned out to be an interesting topic in itself. A comprehensive understanding is important for future microtrap development. In Sec. V the current knowledge is summarized. We conclude the article with a brief outlook on possible applications and perspectives of microtraps as they are currently understood. They range from the physics of degenerate gases in low dimensions to single-particle control and finally culminate in the generation of entanglement and quantum computation. This highly challenging goal is certainly the most fascinating perspective and forms a strong motivation for future research. Bearing in mind the breathtaking speed at which the field of cold atomic gases is evolving, an optimistic view may well turn out to be a realistic view.

II. MAGNETIC MICROTRAPS: BASIC DESCRIPTION

A. Trapping atoms in magnetic fields

Paramagnetic atoms can be trapped by the force acting on their magnetic dipole moment $\vec{\mu}$ in inhomogeneous magnetic fields. Depending on the orientation of the dipole moment relative to the local magnetic field the atom is drawn into the region of high magnetic field ("high-field seekers") or low magnetic field ("low-field seekers"). Since a local magnetic field maximum cannot exist in free space (Ketterle and Pritchard, 1992), static magnetic traps can only trap low-field seekers in local magnetic field minima (Migdall *et al.*, 1985). High-field seekers can be guided along a current carrying wire in states with nonzero orbital angular momentum such that the centrifugal force prevents the atoms from falling onto the surface of the wire (Pron'ko and Stroganov, 1977; Blumel and Dietrich, 1991; Schmiedmayer, 1992, 1995a, 1995b; Hau *et al.*, 1995). Dynamic magnetic traps work for both high-field- and low-field-seeking states (Lovelace *et al.*, 1985; Cornell *et al.*, 1991; Spreeuw *et al.*, 1994; Xu *et al.*, 2001); still, such traps are shallow compared to other trap types.

In this article we focus our attention on magnetostatic traps—i.e., conservative potentials for low-field-seeking atoms. The atom moving inside the trap experiences a temporal change of the magnetic field direction. In the limit of slow atomic motion in a strong magnetic field, the magnetic moment adiabatically follows the orientation of the magnetic field. If this adiabatic condition is fulfilled, the interaction energy between the field $\vec{B}$ and the magnetic moment $\vec{\mu}$ is

$$U = -\vec{\mu}\cdot\vec{B}, \tag{1}$$

simplifies and can be written as a scalar function of the atomic position only.[1] For low-field-seeking states the trapping potential is thus proportional to the magnetic field modulus:

$$U(\vec{r}) = |\vec{\mu}|\cdot|\vec{B}(\vec{r})|. \tag{2}$$

The criterion for adiabaticity can be expressed by

$$d\omega_L/dt \ll \omega_L^2, \tag{3}$$

where the Larmor frequency ω_L for an atom of the total spin $\boldsymbol{F}$ is

$$\omega_L = g_F\mu_B|B|/\hbar\ . \tag{4}$$

Here g_F is the g factor of the spin state and μ_B is the Bohr magneton. If at some point of the trajectory of the atom's motion the adiabatic condition is not fulfilled, the magnetic moment can flip relative to the orientation of the magnetic field. The atom is then transformed into a high-field seeker and ejected from the trapping region ("Majorana spin flip").

In microtraps the magnetic field is generated with miniaturized elements. This allows extraordinarily steep traps because the magnetic field gradient scales quadratically with the inverse spatial extension of the element [cf. Eq. (8)]. Motivation for exploring microtraps was the prospect of making traps with an energy spacing for the trapped quantum states larger than the recoil energy that is transferred during absorption or emission of a photon (Lamb-Dicke regime). In fact this condition had already been met in the first experiments (Vuletic *et al.*, 1998) and proposals have been made for reaching the resolved sideband limit where the energy spacing exceeds the spectral width of a typical single-photon optical-dipole transition (Thywissen *et al.*, 1999; Reichel, 2002). However, this regime would require extremely miniaturized geometries such that the atoms start to interact with the surface of the conductors resulting in losses of atoms. Nevertheless, strong confinement is possible and bears interesting perspectives for low-dimensional physics (Thywissen *et al.*, 1999) and single-atom manipulation. In current experiments the confinement is usually rather moderate and emphasis is more on the construction of interesting potential geometries and temporal schemes for atomic manipulation. The capacity for constructing well-defined micropotentials with complex geometries may turn out to be a crucial advantage for the future development of atom optical devices.

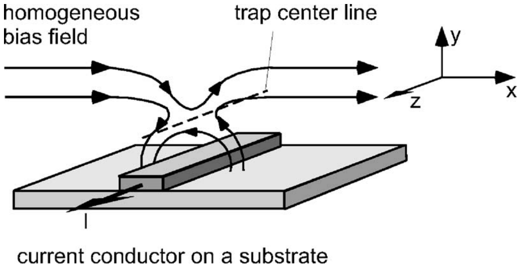

FIG. 1. A simple magnetic waveguide (side guide). A current conductor is placed in a homogeneous bias field resulting in a line of vanishing magnetic field (dashed line). This forms the center of a quadrupole waveguide for paramagnetic atoms.

B. Simple atom guides

The simplest microtrap geometry is a linear quadrupole waveguide, which confines the atoms along a straight line (Fortágh, Grossmann, Zimmermann, and Hänsch, 1998; Denschlag, Cassettari, and Schmiedmayer, 1999; Reichel *et al.*, 1999). It can be realized by a straight conductor placed in a homogeneous bias field B_{bias} that is perpendicular to the conductor (Fig. 1). This geometry is also referred to as a side guide and has been described by Frisch and Sergè (1933). There is no magnetic field component parallel to the conductor (z direction) and the field perpendicular to the conductor (x-y plane) changes its direction within space. For analyzing this geometry the conductor is assumed to be infinitesimally thin and infinitely long, carrying a current I. The total magnetic field is given by

$$\vec{B} = \begin{pmatrix} B_{\text{bias}} \\ 0 \\ 0 \end{pmatrix} + \frac{I\mu_0}{2\pi(x^2+y^2)}\begin{pmatrix} -y \\ x \\ 0 \end{pmatrix}. \tag{5}$$

This configuration exhibits a line of vanishing field parallel to the conductor at the position

---

[1] Following common use, we refer to the magnetic induction B as a "magnetic field." In vacuum the magnetic field H is related to the magnetic induction by $B = \mu_0 H$.

$$x_t = 0, \quad y_t = \frac{I\mu_0}{2\pi B_{\text{bias}}}. \tag{6}$$

Here μ_0 is the induction constant and the origin of the x and y coordinates coincides with the position of the conductor. Low-field-seeking atoms are trapped radially in the x-y plane around the line of vanishing magnetic field that forms the magnetic waveguide. The magnetic field modulus is conveniently written in cylindrical coordinates (r,φ) with the origin at the guide minimum:

$$|B(r,\varphi)| = \frac{I\mu_0}{2\pi r_0} \frac{r}{\sqrt{r^2 + r_0^2 + 2rr_0\cos(\varphi)}}. \tag{7}$$

The angle φ is defined relative to a direct line that connects the conductor and the trap center. The length of this line, i.e., the distance between conductor and the guide, is denoted by r_0. The gradient at the trap center is independent of φ:

$$b := \frac{d}{dr}|\vec{B}(\vec{r})|_{r=0} = \frac{2\pi}{\mu_0}\frac{B_{\text{bias}}^2}{I} = \frac{\mu_0}{2\pi}\frac{I}{r_0^2}. \tag{8}$$

Thus, to first order in r, the waveguide has cylindrical symmetry. This is to be expected from the translational symmetry of the configuration and the vanishing divergence of the magnetic field in free space. The trapping potential is linear in r with a slope that increases with decreasing current in the conductor. Since the waveguide approaches the wire with decreasing I, the assumption of an infinitesimally thin wire eventually breaks down in realistic scenarios for small distances. In many experiments the conductor has a rectangular cross section. Analytic expressions for the resulting field can be found by straightforward integration. In most cases the general expression can be simplified by assuming a conductor with a width w and a negligible height (Reichel, 2002). In this case the field is given by

$$B_x(x,y) = -\frac{\mu_0}{2\pi}\frac{I}{w}\left[\arctan\left(\frac{x+w/2}{y}\right) - \arctan\left(\frac{x-w/2}{y}\right)\right], \tag{9}$$

$$B_y(x,y) = \frac{\mu_0}{4\pi}\frac{I}{w}\ln\left(\frac{(x+w/2)^2+y^2}{(x-w/2)^2+y^2}\right). \tag{10}$$

For $x=0$, and using the notation r_0 for the distance between the conductor and the waveguide, the magnetic field gradient b in the center of the waveguide is

$$b = \frac{\mu_0}{2\pi}\frac{I}{r_0^2 + w^2/4}. \tag{11}$$

Consequently, the trap confinement saturates for distances comparable to the width of the conductor. Almost any microtrap can be traced back to the simple geometry of the side guide. Extensions to more complex geometries are described in Sec. II.D.

Adiabatic loading of atoms into a quadrupole waveguide potential was demonstrated by Fortágh, Grossmann, Zimmermann, and Hänsch (1998). Ballistic propagation of ultracold atoms in a vertically oriented side guide was described by Denschlag, Cassettari, Chenet, *et al.* (1999) and Denschlag, Cassettari, Schmiedmayer (1999). In the same work, guiding of high-field-seeking atoms is also reported. In this case, atoms orbit in a nonconservative potential around a current carrying wire without a bias field. The first demonstration of such Kepler guides goes back to the work of Schmiedmayer (1992, 1995a, 1995b).

C. Majorana losses

The assumption of adiabatic motion of the atomic spin is violated at the center of a linear quadrupole waveguide because of the vanishing magnetic field at the center [cf. Eqs. (3) and (4)]. Here the atoms undergo Majorana spin flips and are lost from the trap. This hole at the trap center is usually fixed by adding an additional homogeneous offset field B_{off} that is parallel to the waveguide axis. Now the total magnetic field is finite also at the trap center and Majorana flips are strongly suppressed. Near the minimum, the magnetic field modulus now reads

$$|\vec{B}(\vec{r})| = \sqrt{b^2r^2 + B_{\text{off}}^2} = B_{\text{off}} + \frac{1}{2}b^2r^2/B_{\text{off}} + \cdots, \tag{12}$$

and the leading term of the potential becomes quadratic with position. The waveguide minimum is formed by a harmonic potential with a radial oscillation frequency of

$$\omega = b\sqrt{\frac{\mu}{mB_{\text{off}}}} = \frac{B_{\text{bias}}^2}{I}\frac{2\pi}{\mu_0}\sqrt{\frac{\mu}{mB_{\text{off}}}}. \tag{13}$$

Such a waveguide is often referred to as a harmonic waveguide. If the waveguide is axially terminated by a harmonic confinement, an Ioffe trap is formed.

Gravity can have a significant impact on the total trapping potential. The gravitational acceleration g shifts the minimum of a harmonic trap by g/ω^2 but does not change the shape of the potential. To minimize this gravitational sag, microtraps are usually oriented horizontally with a strong radial confinement parallel to gravity. For a trap frequency of 1 kHz the gravitational sag ($\sim$250 nm) is already smaller than the width of the trap ground state (for ^{87}Rb $\sim$340 nm). A quadrupole trap becomes asymmetric under the influence of gravity but the position of its center does not change.

In conventional Ioffe traps with oscillation periods of several milliseconds and Larmor frequencies at the trap center on the order of a MHz residual Majorana flips are negligible. In microtraps, however, the trap frequency can be much higher while the Larmor frequency ($\propto B_{\text{off}}$) cannot be increased arbitrarily due to the limited trap depth. Majorana spin flip losses may thus become relevant in limiting the lifetime.

Majorana spin flips have been studied in detail by Sukumar and Brink (1997). For the well-justified simplification in which the nuclear spin is neglected and the total spin is given by only a single electron, the spin-flip transition rate for a single atom in the ground state of a harmonic trap is

$$\Gamma \simeq \frac{\pi\omega}{2} \exp(-E_0/2\hbar\omega), \tag{14}$$

with

$$E_0 = 2\mu B_{\text{off}} + \hbar\omega. \tag{15}$$

This expression is valid for $\mu B_{\text{off}} \gg \hbar\omega$. Using Eq. (13) the offset field B_{off} can be expressed as a function of the trap oscillation frequency ω, yielding

$$\Gamma(\omega) \simeq \frac{\pi}{2\sqrt{e}}\omega \exp\left(-\frac{\hat{\omega}^3}{\omega^3}\right). \tag{16}$$

Here, the critical frequency

$$\hat{\omega} := \left(\frac{\mu^2 b^2}{\hbar m}\right)^{1/3} \tag{17}$$

contains the magnetic field gradient b as the only experimental parameter (Fortágh *et al.*, 2004). For a given trap frequency, the longest lifetimes are obtained for the largest gradients. In other words, the ground-state quality factor $Q = \omega/\Gamma$ drops exponentially if the trap frequency ω approaches the critical frequency $\hat{\omega}$. For rubidium in the $F=2$, $m_F=2$ hyperfine ground state and a magnetic field gradient $b = 10^4$ T/m, which is close to the largest experimentally achieved value so far, $\hat{\omega}$ amounts to $2\pi \times 1.3$ MHz. For a thermal gas in the limit $k_B T \gg 2\hbar\omega$, a decay rate of

$$\Gamma_{\text{the}} = \pi\omega \frac{\hbar\omega}{k_B T} \exp\left(-\frac{E_0}{k_B T}\right) \tag{18}$$

is found (Sukumar and Brink, 1997). Here T is the temperature of the gas and k_B is Boltzmann's constant.

If the nuclear spin is taken into account, Majorana transitions can also occur between different low-field-seeking hyperfine states, for example, the rubidium states $F=2$, $m_F=2$ and $F=2$, $m_F=1$. A mixture of atoms in these two states decays rapidly due to spin changing collisions (Weiner *et al.*, 1999). In some experiments with particularly light atoms such as lithium this decay channel may become an important effect (Silber *et al.*, 2005). In a quadrupole waveguide the decay for single atoms in low-lying quantum states has been studied theoretically (Hinds and Eberlein, 2000). The Q factor is smallest here for the ground state ($Q=7.8$) and increases for states with higher energy. There are no studies yet on the Majorana decay of gases in the degenerate regime. For recent theoretical work on the dynamics of single fermions and bosons in magnetic waveguides we refer the reader to Lesanovsky and Schmelcher (2004, 2005a, 2005b).

Besides Majorana spin flips there are other intrinsic loss mechanisms specific to microtraps. Tunneling may cause losses for particular realizations of the harmonic trapping potential (Thywissen *et al.*, 1999). In contrast to Majorana spin flips, tunneling is largest for the highest-energy bound state. Nevertheless, in the majority of experiments this loss is negligibly small. Losses due to the interaction of atoms with the microtrap surface are discussed in Sec. V.

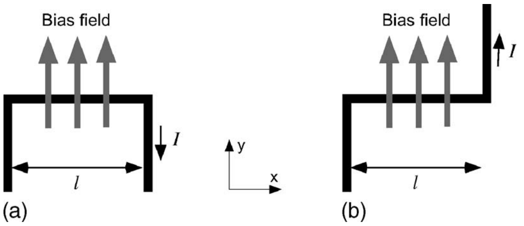

FIG. 2. Wire layout for a U trap (a) with a quadrupole potential and a Z trap (b) with a harmonic potential (Ioffe trap).

D. Advanced trap geometries

1. Z- and U-shape traps

A simple waveguide as described above confines the atoms only in the radial direction. In this idealized case, where the potential is generated by the magnetic field of an infinitely long wire, a bias, and an offset field, the axial motion is free. In real experiments with wires of finite length the axial potential depends critically on the wire termination. For planar geometries there are two qualitatively different cases (Fig. 2). At both ends the conductor can be bent either in the same direction (U shape) or in opposite directions (Z shape). The latter results in an elongated three-dimensional harmonic trapping potential with a nonzero field at the minimum (Ioffe trap). Conversely, the symmetry of the U-shaped trap requires a point of vanishing magnetic field, resulting in a spherical quadrupole trap centered between the terminating ends. A thermal gas can be stored in such a trap; however, a Bose-Einstein condensate would rapidly decay because of Majorana spin flips. Z- and U-shape geometries are used in a large number of experiments for the axial termination of microtrap waveguides and for intermediate trapping as part of the loading procedure of microtraps. Experimental realizations are described among others by Denschlag, Cassettari, Chenet, *et al.* (1999), Reichel *et al.* (1999), Cassettari, Chenet, *et al.* (2000), Folman *et al.* (2000), and Haase *et al.* (2001).

The magnetic field of bent conductors can be calculated by combining the analytic expression for the field of wires with finite length. A wire placed along the z axis and ranging from $-l/2$ to $l/2$ still generates a circular field with vanishing z component, but the field strength is now given by

$$B(\vec{r}) = \frac{\mu_0}{4\pi}\frac{I}{\sqrt{x^2+y^2}}\left(\frac{z+l/2}{\sqrt{x^2+y^2+(z+l/2)^2}} - \frac{z-l/2}{\sqrt{x^2+y^2+(z-l/2)^2}}\right). \tag{19}$$

For a specific trap configuration the field contributions

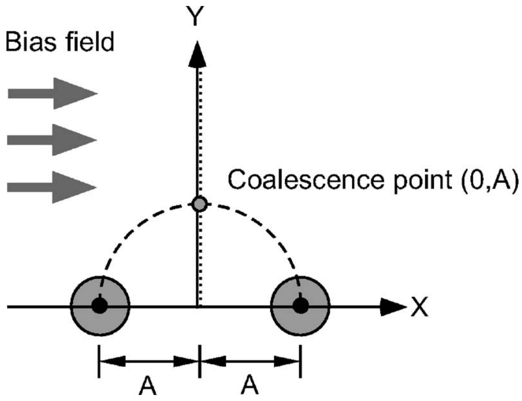

FIG. 3. Atom guide using two current carrying wires and a bias field. With the bias field increasing, two guiding regions move towards each other along y (dotted line) until they coalesce at $y=A=d/2$ with d being the distance between the two wires. They then separate along the dashed semicircle. Adapted from Hinds *et al.*, 2001.

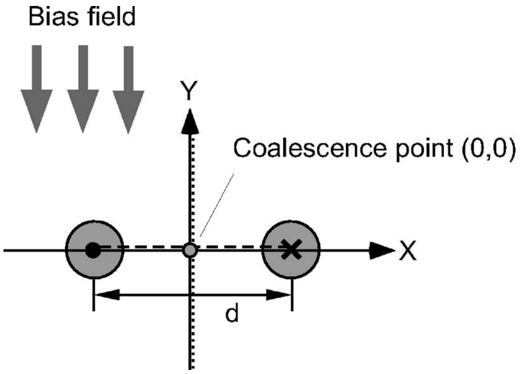

FIG. 4. Two wires with opposite currents in a vertical bias field.

of individual wire segments are best superposed numerically.

Guiding potentials can be closed at both ends by using additional "pinch wires" as well. These are oriented perpendicular to the waveguide axis. If the conductors are microfabricated in a single plane, the crossing of conductors is unavoidable. By exploiting the field of such a crossing, potential wells and barriers can be constructed in certain orientations of the offset field relative to the pinch wire (Reichel *et al.*, 2001). It is also possible to fabricate pinch wires in different layers of a chip, for instance, on the backside of the substrate-such that a direct conductor crossing is avoided. The currents in the conductors are then decoupled, and the arrangement allows larger flexibility (Günther, Kemmler, *et al.*, 2005).

2. Double-wire guides

The next step toward more complex waveguide geometries is shown in Fig. 3. The magnetic field of two parallel wires separated by a distance d, carrying parallel, equal currents I, is combined with a bias field B_{bias}, which is parallel to the plane of the wires (Hinds *et al.*, 2001). This configuration features two lines of vanishing magnetic field, i.e., two linear quadrupole waveguides which can be made harmonic by superimposing an axial offset field. The positions of the quadrupole guides depend on the value of the bias field B_{bias} and a critical field

$$B_0 = \frac{\mu_0 I}{\pi d}. \tag{20}$$

For $B_{\text{bias}} < B_0$ the guides lie in the symmetry plane between the conductors, with the coordinates $x=0$ and

$$y = \frac{d}{2}\frac{B_0}{B_{\text{bias}}}\left[1 \pm \sqrt{1-\left(\frac{B_{\text{bias}}}{B_0}\right)^2}\right]. \tag{21}$$

In this regime the gradient amounts to

$$b = \frac{2B_0}{d}\sqrt{1-\left(\frac{B_{\text{bias}}}{B_0}\right)^2}\left[1 \mp \sqrt{1-\left(\frac{B_{\text{bias}}}{B_0}\right)^2}\right]. \tag{22}$$

For $B_{\text{bias}}=B_0$ the two waveguides merge and form a hexapole waveguide. In the regime $B_{\text{bias}}>B_0$ the hexapole falls apart into two quadrupole waveguides, each approaching one of the wires on a semicircular trajectory. The coordinates of the waveguide centers are

$$x = \frac{d}{2}\frac{B_0}{B_{\text{bias}}}\left[\pm\sqrt{\left(\frac{B_{\text{bias}}}{B_0}\right)^2 - 1}\right], \tag{23}$$

$$y = \frac{d}{2}\frac{B_0}{B_{\text{bias}}}. \tag{24}$$

The field gradient is now the same in both waveguides:

$$b = \frac{2B_{\text{bias}}}{d}\sqrt{\left(\frac{B_{\text{bias}}}{B_0}\right)^2 - 1}. \tag{25}$$

This configuration has been used by Shin, Sanner, *et al.* (2005) to split a Bose-Einstein condensate (Sec. IV.C).

If just wires are operated without a bias field, the waveguide is centered between two conductors. A small horizontal (vertical) bias field now displaces this waveguide vertically (horizontally). Such an experimental scenario was realized by Müller *et al.* (1999): Two parallel conductors with cross sections of $100\times100\ \mu\text{m}^2$, electroplated on a substrate at a spacing of 100 μm, were used for transporting atoms between two vacuum chambers along a total guiding distance of 10 cm. To turn off the flux of atoms, a small bias field was applied. The bias field displaced the waveguide center towards the substrate that blocked the guide.

A waveguide is also obtained if the current in one of the wires is inverted (Thywissen *et al.*, 1999; Cassettari, Chenet, *et al.*, 2000). The bias field is now oriented perpendicular to the plane of the wires (Fig. 4). For large current values two linear quadrupole waveguides exist, one on each side of the wire plane at $x=0$,

$$y = \pm \frac{d}{2}\sqrt{\frac{I}{I_0} - 1}. \tag{26}$$

Guiding of ultracold atoms using this scheme on a microfabricated chip was demonstrated by Dekker *et al.* (2000). With decreasing current I in each of the wires the waveguides approach the wire plane along the y axis and merge at $y=0$ for a critical current of

$$I_0 := \frac{\pi B_{\text{bias}} d}{2\mu_0}. \tag{27}$$

In the regime $I > I_0$, the gradient at the trap center is

$$b = \frac{2\pi B_{\text{bias}}^2}{\mu_0 \, I}\sqrt{\frac{I}{I_0} - 1}. \tag{28}$$

For $I < I_0$ the quadrupoles separate again and move in the wire plane each toward one of the wires.

Such a geometry is particularly suitable for bringing atoms close to the surface of a substrate in a controlled way. On the other hand, if realized with two freestanding wires or wires attached to the edges of a slit, the hexapole that forms at $I = I_0$ offers interesting possibilities for constructing a trap with rather boxlike radial potential ($\sim r^4$).

3. Continuous transformation of trap geometries

The double-wire geometry with a bias field is one example of how traps can be continuously transformed by varying the bias field or the currents in the wires. Such transformations are exploited for manipulating atomic ensembles in microtraps. At small bias field, for instance, atoms could be loaded into the distant waveguide at large y (Fig. 3). By increasing the bias field the atomic cloud approaches the wires and is then split into two parts at the coalescence point. If the two parts are phase-coherent objects such as Bose-Einstein condensates, an interferometer may be realized by recombining the two parts after some holding time (cf. Secs. III.C and IV.C). This scheme could also be useful for loading tightly confining waveguides with thermal atoms from a magneto-optical trap (MOT). In this case the bias field would be increased further beyond the critical point such that the two parts are compressed into the increasingly steeper traps close to the two wires.

In the first experimental realization of a surface microtrap (Fortágh, Grossmann, Zimmermann, and Hänsch, 1998) the atoms were loaded with a similar scheme. The apparatus combines a wire with a pair of coils in anti-Helmholtz configuration (Fig. 5). In the vicinity of the center between the coils the total magnetic field is approximately given by the superposition of the spherical quadrupole field that is generated by the coils and the circular field of the wire:

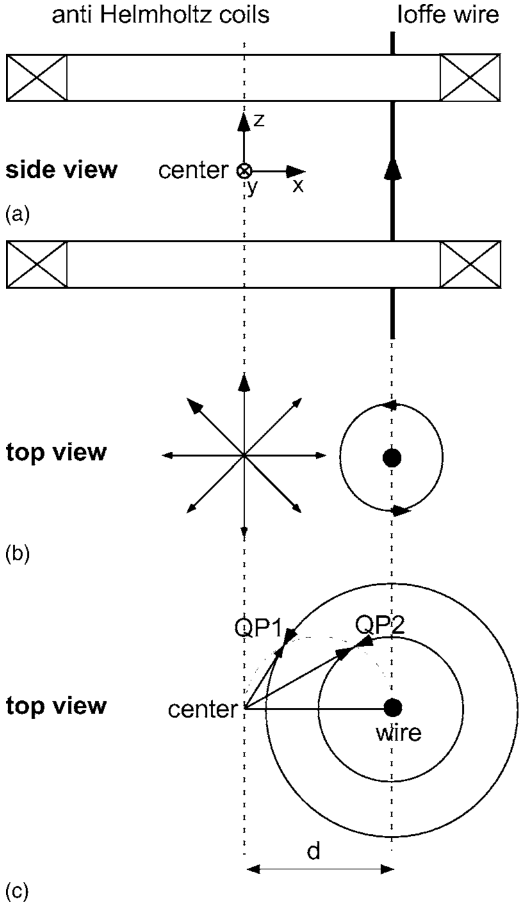

FIG. 5. Transformation of a quadrupole trap into an Ioffe trap. (a) The setup consists of a pair of coils operated in the anti-Helmholtz configuration and a Ioffe wire. (b) The spherical quadrupole field generated by the coils is superimposed with the circular field of the wire. (c) In the symmetry plane between the coils two spherical quadrupole minima appear (QP1 and QP2). With increasing current in the wire the two minima approach each other on a semicircular trajectory and merge eventually to form an Ioffe trap.

$$\vec{B}(\vec{r}) = \frac{\mu_0}{2\pi}\frac{I}{(x-d)^2 + y^2}\begin{pmatrix} -y \\ x-d \\ 0 \end{pmatrix} + \frac{1}{2} b_z \begin{pmatrix} x \\ y \\ 2z \end{pmatrix}. \tag{29}$$

Here d is the distance between the wire and the midpoint between the coils and I is the current in the wire (Fortágh *et al.*, 2000). The spherical quadrupole generated by the coils is characterized by the magnetic field gradient $b_z = dB_z/dz$ along the symmetry axis of the coils (z axis). The total field features two spherical quadrupoles. Having a small but finite current in the wire, the quadrupole generated by the coils (QP1) is almost unaffected but a second quadrupole (QP2) appears close to the wire. With increasing current the two quadrupoles approach each other on a circular trajectory. Their positions are best described in polar coordinates with the origin halfway between the wire and the center between the coils (Fig. 6). The two quadrupole traps appear si-

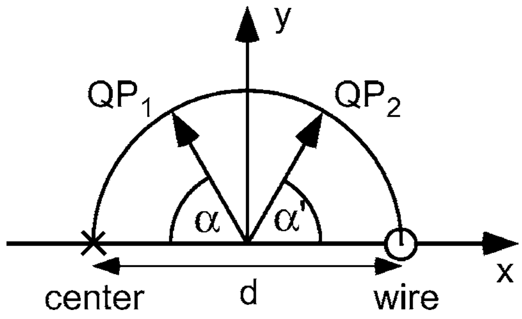

FIG. 6. Position of the spherical quadrupole minima for the geometry in Fig. 5. The center of the quadrupole generated by the coils is at $y=0$ and $x=-d/2$. The wire is at $y=0$ and $x=d/2$. Adapted from Fortágh *et al.*, 2000.

multaneously on a semicircle with a radius of $d/2$ at angles

$$\alpha = \alpha' = \arcsin(I/I_0). \tag{30}$$

Here I_0 is a critical current defined as

$$I_0 := \frac{1}{2}\frac{\pi}{\mu_0} b_z d^2. \tag{31}$$

At $I=I_0$ both quadrupoles merge and the gradient of the field modulus in the x direction vanishes. The leading term of the x component of the magnetic field is then given by the curvature

$$\frac{d^2}{dz^2}|B| = \frac{b_z}{d}. \tag{32}$$

The gradients in the y and z directions are both equal to b_z. For $I>I_0$ an Ioffe trap is formed with a harmonic trapping potential and finite offset field. For $I<I_0$ the quadrupoles are separated and the trap depth is limited by a saddle point between them. While increasing the current from zero to I_0 the position of this saddle point moves from the wire to the position of the Ioffe trap on a straight line. The coordinates of the saddle point are

$$x_s = d - q/\sqrt{2}, \quad y_s = q/\sqrt{2}, \tag{33}$$

where

$$q := \sqrt{\mu_0 I/\pi b_z} \tag{34}$$

is the distance between the saddle point and the wire. The magnetic field at the saddle point amounts to

$$B = \frac{b_z}{2}(d - \sqrt{2}q). \tag{35}$$

The gradient of the quadrupole trap starting from the wire (QP2) is given by

$$b_q = \frac{b_z}{2}\frac{d^2}{q^2}. \tag{36}$$

Its center is separated from the wire by q^2/d.

Atoms that have been initially loaded into the center quadrupole of the coils (QP1) can be adiabatically transferred into the Ioffe trap by slowly increasing the current I in the wire. In the Ioffe trap, the atoms can be cooled by forced evaporation before they are moved further in QP2 to the surface of the microtrap.

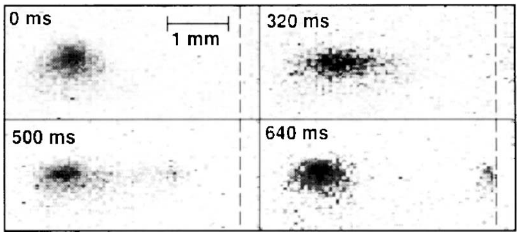

FIG. 7. Absorption images at various stages of the adiabatic transfer of atoms into the microtrap. The microtrap is generated at the surface of a thin wire (90 μm diameter) carrying a current of 1.4 A. The thin wire (indicated by the dashed line) is attached to the surface of the Ioffe wire (1.4 mm diameter, to the right of the dashed line). Atoms are initially loaded into the spherical quadrupole trap QP1 with zero current in the Ioffe wire. Within the next 320 ms, the trap is adiabatically transferred into the Ioffe trap ($I=9.5$ A). The microtrap is loaded from QP2 within the following 320 ms when the current in the Ioffe wire is reduced to zero. Here 14% of the atoms is loaded into the microtrap. The rest goes back to QP1 and is visible to the left. From Fortágh, Grossmann, Hänsch, and Zimmermann, 1998.

An early realization of this transfer is shown in Fig. 7. Here a microtrap is formed at a thin wire (90 μm diameter) that is attached to the surface of the Ioffe wire. The thin wire is parallel to the Ioffe wire and is at the position where the semicircle of the quadrupole trajectories reaches the Ioffe wire (cf. Fig. 5). The thin wire is driven by a current; thus, its field adds to the field of the Ioffe wire. This way, the microtrap can be loaded adiabatically from QP2 by reducing the current in the Ioffe wire to zero. The experiment was done with 6×10^6 atoms (^{87}Rb, $n\sim7\times10^9$ cm^{-3}, $T\sim32$ μK) from which 14% were adiabatically loaded and compressed into the microtrap (Fortágh, Grossmann, Zimmermann, and Hänsch, 1998). Inverting the current in the Ioffe wire compresses the cloud further towards the thin wire. If the upper coil is slowly turned off, the atoms remain trapped; the vertical confinement is given by the magnetic field of the lower coil and gravity. The potential minimum is now at a position of finite magnetic field such that Majorana transitions are suppressed.

Ioffe traps as described above are used in several experiments for adiabatically loading atoms into microtraps (Ott *et al.*, 2001; Fortágh *et al.*, 2003; Lin *et al.*, 2004). An advanced version of this Ioffe trap was described by Silber *et al.* (2005).

4. Guides with integrated bias field

Experimentally it is often favorable to avoid an external bias field. If the bias field is generated on the chip, it is far better controlled, resulting in more precise knowledge of the trap geometry. Quadrupole traps and Ioffe traps generated by miniaturized conductors without external fields have already been proposed in the pioneer-

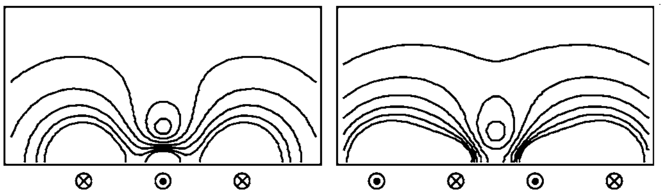

FIG. 8. Configurations for atom guides with internal bias field. From Cassettari, Chenet, *et al.*, 2000.

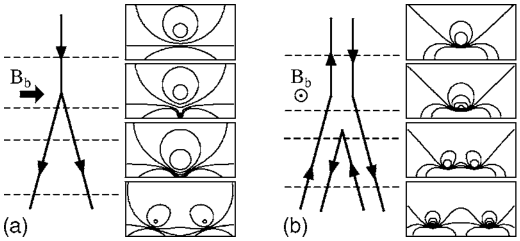

FIG. 9. Y junctions based on (a) a single-wire and (b) a double-wire geometry. From Cassettari, Chenet, *et al.*, 2000.

ing work of Weinstein and Libbrecht (1995). These geometries have been developed under the restricting assumption that all conductors are placed in a single plane at the surface of the substrate. Today, three-dimensional geometries are also used with conductors in different layers, allowing conceptually simpler ways for constructing versatile and flexible trap configurations.

Two simple configurations that avoid external bias fields are the three- and four-wire waveguides (Thywissen *et al.*, 1999; Cassettari, Chenet, *et al.*, 2000) as shown in Fig. 8. In the first case the two equal and parallel currents in the outer conductors generate the bias field for the center conductor. The position of the resulting waveguide is

$$x = 0, \quad y = \frac{d}{2}\sqrt{\frac{1}{2\beta - 1}}. \tag{37}$$

Here d is the separation between the two outer conductors, $\beta = I_{\text{outer}}/I_{\text{inner}}$ is the ratio between the currents of the outer and inner conductors, and the origin of the x and y coordinates coincides with the position of the inner conductor. The radial gradient is given by

$$b = b_h \frac{y^2}{d^2}\frac{4(2\beta - 1)^2}{\beta} = b_h \frac{2}{1 + (2y/d)^2}. \tag{38}$$

The reference value

$$b_h = \frac{\mu_0}{2\pi}\frac{I_{\text{inner}}}{y^2} \tag{39}$$

is equal to the gradient of a simple single wire trap (side guide) in a homogeneous bias field. The largest gradient is obtained in the limit of small y. Then, $b \simeq 2b_h$ and the gradients from the outer wires increase the trap steepness by a factor of 2.

With unbalanced currents in the outer conductors I_1 and I_3 the trap position can be controlled in the plane perpendicular to the wire (Günther, Kemmler, *et al.*, 2005). With the three conductors equally separated by a distance d and a current I_2 in the inner conductor, the trap position is given by

$$x = \frac{d}{2}\frac{I_1 - I_3}{I_1 + I_2 + I_3}, \quad y = \frac{d}{2}\frac{[4I_1I_3 - (I_1 + 2I_2 + I_3)^2]^{1/2}}{I_1 + I_2 + I_3}. \tag{40}$$

The four-wire waveguide allows for somewhat tighter confinement (Thywissen *et al.*, 1999). Having the origin of the x and y coordinates between the two inner conductors, the coordinates of the waveguide read

$$x = 0, \quad y = \frac{d}{2}\sqrt{\frac{\alpha - \beta}{\beta - 1/\alpha}}. \tag{41}$$

Here $\beta = I_{\text{outer}}/I_{\text{inner}}$ is the ratio of the currents with both inner and outer conductors carrying the currents I_{inner} and I_{outer}, respectively. $\alpha = d_{\text{outer}}/d$ is the ratio of the separations between the outer conductors d_{outer} and the inner conductors d. The radial gradient is given by

$$b = \frac{\mu_0}{2\pi}\frac{I_{\text{inner}}}{d^2}\frac{15}{\beta(\alpha^2 - 1)^2}\sqrt{(\alpha\beta - 1)^5\left(1 - \frac{\beta}{\alpha}\right)}. \tag{42}$$

The outer wire current that maximizes the gradient is

$$\beta_{\max} = u(1 + \sqrt{1 + u^2/2}), \tag{43}$$

with

$$u = (3\alpha^2 - 1)/8\alpha. \tag{44}$$

For equally spaced wires ($\alpha = 3$) the gradient is maximized for $\beta = 2.44$ and is

$$b_{\max} = 4.16\frac{\mu_0}{2\pi}\frac{I_{\text{inner}}}{d^2}. \tag{45}$$

Guiding of atoms in a four-wire guide on a chip was demonstrated by Dekker *et al.* (2000). A nonplanar four-wire guide was realized by Key, Hughes, *et al.* (2000) and Key, Rooijakkers, and Hinds (2000): The four wires are at the corner of a square, centered around the hollow core of a silica fiber through which the atoms are guided.

5. Y junctions and "optical" couplers

Y junctions as shown in Fig. 9 have been proposed and realized for splitting and deflecting waveguide potentials (Denschlag, Cassettari, Chenet, *et al.*, 1999; Cassettari, Hessmo, *et al.*, 2000; Müller *et al.*, 2001; Kraft *et al.*, 2005). The equipotential surface of a Y junction made from a single-wire splitting is shown in Fig. 10. The junction features one main input waveguide and two output waveguides. On the input side a fourth "blind" waveguide emerges from the plane of the wires and joins the other three waveguides at the coalescence point. The distance of the input waveguide and the blind waveguide from the surface is

$$y_{\pm} = \tfrac{1}{2}(d_{\text{split}} \pm \sqrt{d_{\text{split}}^2 - d^2}), \tag{46}$$

with d being the distance between the outgoing wires and

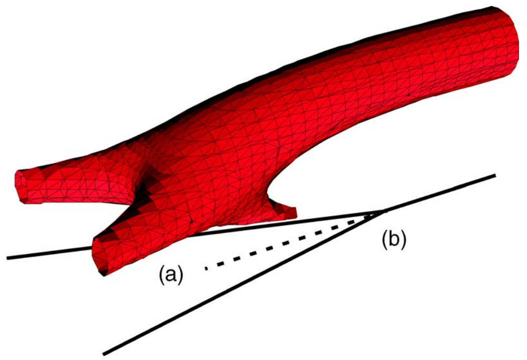

FIG. 10. (Color online) Equipotential surface of a Y junction made from a single-wire splitting. From Cassettari, Chenet, *et al.*, 2000.

$$d_{\text{split}} = \frac{\mu_0}{\pi} \frac{I}{B_{\text{bias}}}. \tag{47}$$

The two input waveguides merge at $d = d_{\text{split}}$ such that the coalescence point is not at the geometric position of the wire splitting [cf. Eq. (21)]. This Y junction is the simplest example of a switch for a guided atomic beam. By switching the current from one of the outgoing wires into the other, the atomic flux can be switched between the two outputs.

Beam splitters based on a Y-shaped free-standing wire were demonstrated by Denschlag, Cassettari, Chenet, *et al.* (1999). Beam splitting on a Y-shaped chip conductor was demonstrated by Cassettari, Chenet, *et al.* (2000) and Cassettari, Hessmo, *et al.* (2000). Depending on the current ratio between the two arms of the Y junction, a thermal atomic beam was deflected into one of the two output ports (Fig. 11). The splitting ratio was varied between 15% and 85%. The arm carrying higher current was preferred due to the larger transverse size of the guiding potential. By analyzing the atomic distribution, the back reflection at the splitting point was estimated to be less than 20%.

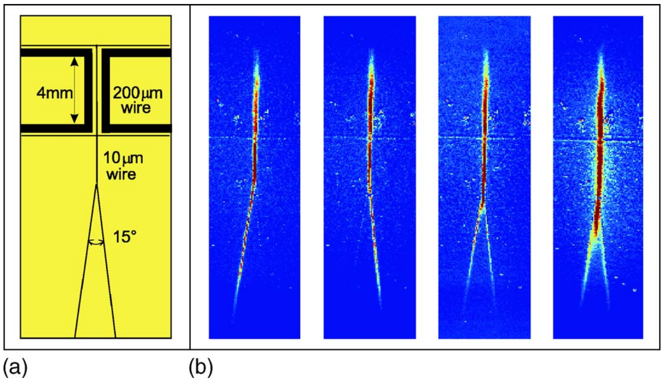

FIG. 11. (Color online) Y junction on a chip: (a) Chip schematic. The two large U-shaped, 200 μm wide wires are used to load atoms into the 10 μm wide Y-shaped guide. (b) Fluorescence images of guided atoms. In the first two images, the current is driven through a single arm of the Y junction, thereby guiding atoms either to the left or to the right. The last two images were taken for two different radial confinements with equal currents in the two arms of the Y junction. The expansion in the waveguide was driven by the thermal velocity distribution of the atoms. From Cassettari, Hessmo, *et al.*, 2000.

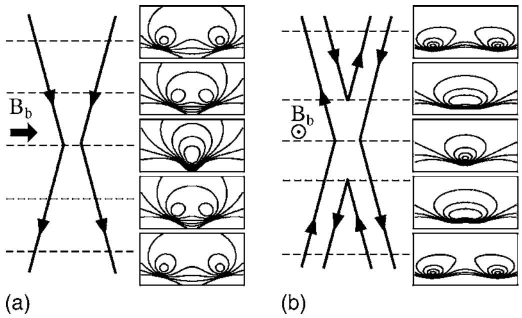

FIG. 12. X junctions and optical couplers for matter-waveguides. Depending on the strength of the bias field two approaching guides can completely merge their potentials. If the bias field is sufficiently large and a residual barrier is left, the atoms may escape the waveguide by quantum tunneling. From Cassettari, Chenet, *et al.*, 2000.

If both arms of the Y junction are activated, the currents in the two outgoing wires are necessarily reduced relative to the current in the incoming arm, leading to an increased radial confinement in the outgoing channels. For the construction of a coherent matter-wave beam splitter this restriction could be problematic and a double-wire guide geometry as shown in Fig. 9(b) might be favorable. The blind waveguide is now absent, and the two adjustable currents allow for the matching of the guide confinement at the splitting point.

Another geometry that has been studied theoretically by Stickney and Zozulya (2003) consists of two wires in a parallel bias field (Fig. 12). The wires approach, but do not touch each other. For a wire separation $d < d_{\text{split}}$ the two waveguides merge and form a junction with four ports. The critical distance d_{split} can be controlled with the bias field. If the closest distance between the two waveguides is larger and close to d_{split}, the atoms may tunnel between the waveguides similar to optical couplers in fiber optics. Such couplers are more tolerant to nonadiabatic effects, but more sensitive to nonlinearities due to atomic interaction (see Sec. III). Similar optical couplers can also be constructed with pairs of wires [Fig. 12(b)].

The X junction for guided thermal atoms has been demonstrated by Müller *et al.* (2000) using two square conductors (100 μm wide) with equal and parallel currents in a bias field. One of the arms was loaded with atoms. Depending on the current distribution in the wires, the ratio of atom numbers in the two output ports was varied between 100/0% and 15/85%, respectively. The splitting ratio also depends on the bias field and the bending of the conductors, as these parameters determine the overlap of the waveguides.

A conceptually similar magnetic switch realized by Müller *et al.* (2001) is shown in Fig. 13. Atoms entering the center guide between two primary wires are de-

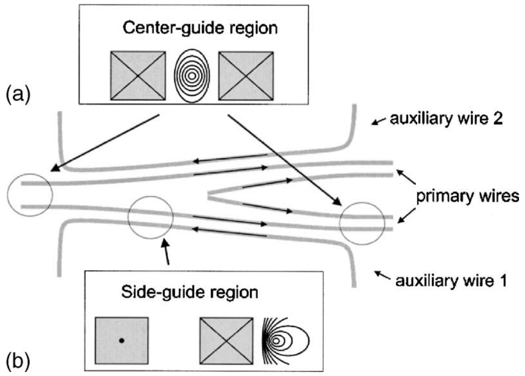

FIG. 13. Switch schematic (not to scale). Insets (a) and (b) show the magnetic field contour lines for each region. The switch starts and ends with a center guide (a). In the middle of the switch, atoms are transferred from a center guide to a side guide (b). Depending on which one of the two auxiliary wires 1 and 2 is turned on, the atoms exit port 1 or 2, respectively. From Müller *et al.*, 2001.

flected into one of the side guides depending on which one of the auxiliary wires is activated. In the region where the auxiliary wires recede the side guides are transformed back into center guides. Switching between the two output ports is possible by activating the corresponding auxiliary wire.

6. Magnetic lattices

Periodic potentials are formed by sets of parallel conductors (Opat *et al.*, 1992; Drndic *et al.*, 1999; Lau *et al.*, 1999). Such magnetic lattices are interesting for diffraction of matter waves (Günther, Kraft, *et al.*, 2005), but also for the construction of conveyor belts (Hinds and Hughes, 1999; Reichel *et al.*, 2001; Günther, Kemmler, *et al.*, 2005) and for the construction of massively parallel arrays of atom interferometer circuits (Zobay and Garraway, 2000).

The magnetic field of $2N+1$ infinitely long and infinitesimal thin parallel conductors oriented along the x direction and separated by a distance d with alternating currents I between neighboring wires (Fig. 14) is given by the components

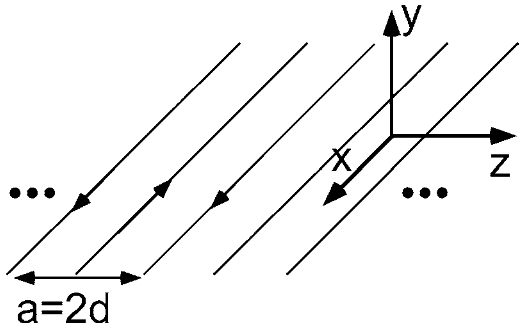

FIG. 14. Magnetic lattice with alternating currents in neighboring wires.

$$B_z = K \sum_{n=-N}^{N} (-1)^n \frac{y/d}{(y/d)^2 + (z/d-n)^2}, \tag{48}$$

$$B_y = -K \sum_{n=-N}^{N} (-1)^n \frac{z/d-n}{(y/d)^2 + (z/d-n)^2}, \tag{49}$$

with

$$K := \frac{\mu_0 I}{2\pi d}. \tag{50}$$

The y direction is defined as perpendicular to the lattice plane; the z direction is rectangular to the lattice wires but in the plane of the lattice. For an infinite number of wires ($N \to \infty$) the sums can be evaluated as

$$B_z = 2\pi K \frac{\cos kz \sinh ky}{\cosh 2ky - \cos 2kz}, \tag{51}$$

$$B_y = -2\pi K \frac{\cosh ky \sin kz}{\cosh 2ky - \cos 2kz}. \tag{52}$$

The wave vector k corresponds to the lattice constant $a := 2d$ as

$$k := \frac{2\pi}{a} = \frac{2\pi}{2d} = \frac{\pi}{d}. \tag{53}$$

In the limit for large distances form the lattice plane $y \gg a$, the expressions simplify to

$$B_z \cong 2\pi K \cos kz \exp(-ky), \tag{54}$$

$$B_y \cong -2\pi K \sin kz \exp(-ky), \tag{55}$$

and

$$|B(z,y)| \cong 2\pi K \exp(-ky). \tag{56}$$

The magnetic field modulus drops off exponentially with the distance from the wire plane. This feature has been exploited for the construction of magnetic mirrors (Hinds, 1999).

With a bias field in the z direction, quadrupole channels appear close and parallel to every second wire. For negative values of y (i.e., inside the substrate) another set of linear quadrupoles appears, shifted by half a lattice constant. For a basic harmonic waveguide that is brought close to a lattice with alternating currents these linear quadrupoles appear as side effects: The bias and the offset field are unavoidably introduced by the field of the harmonic waveguide. Nevertheless, such a potential can be used for the diffraction of a condensate from a magnetic lattice (Günther, Kraft, *et al.*, 2005).

The field of a realistic lattice with a finite number of wires must be evaluated numerically. Fringe effects, which are qualitatively different for an *even* or an *odd* number of wires, have to be taken into account. For a finite lattice the amplitude of the periodic potential varies slowly along the lattice according to an envelope that peaks at both ends of the lattice. For a lattice with an odd number of wires the envelope exhibits a vanishing gradient at the center of the lattice and a finite curvature, while for an even number the gradient is finite and the curvature vanishes. Fringe effects can be partly compensated by additional compensation wires at both ends.

If two lattices (with alternating currents) are combined with a periodicity different by a factor of 2 and opposite currents for wires at the same position, out-of-plane quadrupole waveguides occur even without bias field (Zobay and Garraway, 2000). With increasing bias field new waveguides appear and approach the plane coming in from $y=\infty$. At a critical field the waveguides merge pairwise and form a set of hexapole waveguides. An offset field along the direction of the wires (x direction) transforms the quadrupole guides into stable harmonic waveguides. This way, tightly confining waveguides may form very close to the surface. They could be loaded by continuously increasing the bias field. As proposed by Zobay and Garraway (2000), the possibility to merge two traps can be exploited for the construction of an array of atom interferometers.

7. Adiabatic potentials

Adiabatic potentials arise whenever two or more internal atomic states that experience different potentials for the atomic center-of-mass motion are coupled by a resonant external field. The new adiabatic potential arises from the diagonalized Hamiltonian consisting of the bare potentials and the coupling term (Rubbmark *et al.*, 1981; Zobay and Garraway, 2001, 2004; Courteille *et al.*, 2006; Lesanovsky *et al.*, 2006). In a static magnetic field B_{dc} the different spin states of an atom can be coupled by an oscillating magnetic field $B_{\mathrm{rf}\perp}\cos(\omega_{\mathrm{rf}}t)$, which has a polarization perpendicular to the static field. The frequency for resonant coupling is given by the Larmor frequency ω_L as in Eq. (4). In a typical magnetic trap, ω_L is in the radio-frequency (rf) range.

The spatial variation of the static magnetic field in a trap allows for localized coupling (Fig. 15). The frequency of the coupling field determines the location of the resonant coupling, and the magnitude of its projection perpendicular to the static field determines the energy splitting of the new eigenstates. By analogy, an Ioffe-Pritchard magnetic trap can be considered as the anticrossing of binding and antibinding states of a quadrupole potential that are split by the static magnetic offset field perpendicular to the quadrupole axis. The conditions for adiabatic following of the dressed potential are given by the Landau-Zener theory, as described in the references above.

From the more general theory (Courteille *et al.*, 2006; Lesanovsky *et al.*, 2006) one can derive a simple expression in terms of magnetic fields which describes the rf-induced adiabatic potentials in the special case that a single-frequency component is applied:

$$V_{m_F}(\mathbf{r}) = m_F\sqrt{(\mu_B g_F B_{\mathrm{dc}}(\mathbf{r}) - \hbar\,\omega_{\mathrm{rf}})^2 + (\hbar\Omega)^2}. \tag{57}$$

Here m_F is the magnetic quantum number of an atom with the total spin F, g_F is the g factor, μ_B is the Bohr magneton, and $\hbar$ is the reduced Planck's constant. The linearly polarized radio-frequency field couples the atomic sublevels $|F,m_F\rangle \leftrightarrow |F,m_F'\rangle$, with $m_F'=m_F\pm1$, and the strength of the coupling is given by the resonant Rabi frequency $\Omega=(\mu_B g_F/4\hbar)B_{\mathrm{rf}\perp}\sqrt{F(F+1)-m_F m_F'}$ (Ketterle and van Druten, 1996). Note the analogy between Eqs. (12) and (57).

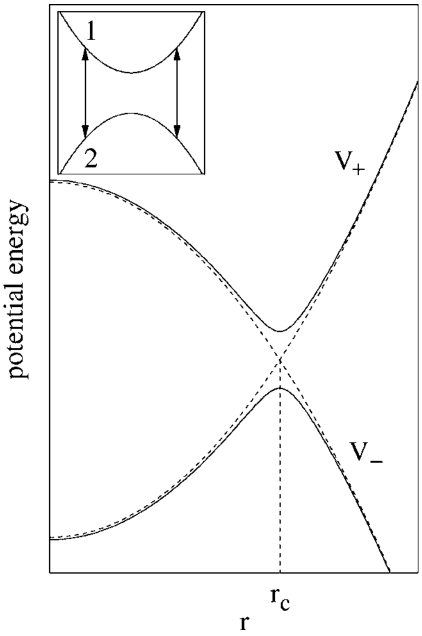

FIG. 15. Schematic of field-induced adiabatic potentials $V_\pm$ for $(\omega_{\mathrm{rf}} > \omega_L)$. Dashed curves show the harmonic bare potentials crossing at r_c. Inset: coupling of bare potentials at $\pm r_c$ by rf radiation (arrows). From Zobay and Garraway, 2004.

Radio-frequency-induced adiabatic potentials are commonly used in evaporative cooling. In this situation the applied radio frequency ω_{rf} is larger than ω_L, the Larmor frequency in the center of the trap (Fig. 15). The center-of-mass motion of low-energy atoms will follow the adiabatic potential V_-, while atoms with sufficiently large energy will adiabatically leave the trap. Cooling is initiated by reducing the radio frequency. An opposite scenario was considered by Zobay and Garraway (2001, 2004). If the frequency of the rf is continuously increased from a value smaller than ω_L to above ω_L, atoms will be transferred into the adiabatic potential V_+. This approach has been pioneered experimentally by Colombe *et al.* (2004) and used by Schumm *et al.* (2005b) and Jo *et al.* (2006) to split a condensate initially prepared in a single-well into a double-well potential (Sec. IV.C). Resonators for atoms have also been demonstrated using this approach (Bloch *et al.*, 2001). Radio-frequency- and microwave-induced adiabatic potentials represent a powerful tool for structuring the magnetic potential of microtraps and for the coherent manipulation of matter waves. Since the static magnetic field of the trap defines the local quantization axis for the atomic spin, the frequency, magnitude, as well as the orientation of the oscillating field are crucial for determining the shape of the resulting adiabatic potential. Ring-shaped and double-well potentials have been proposed by Lesanovsky, Schumm, *et al.* (2006) and Lesanovsky, Hoffenberth, *et al.* (2006). Potential shaping by multifrequency rf fields and periodic potentials based on rf combs have been described by Courteille *et al.* (2006).

8. Conveyor belts and three-dimensional positioning on a chip

A variety of trap geometries have been studied recently including rotatable traps, colliders for atomic clouds, barriers, and double-well potentials (Rosenbusch *et al.*, 2000a; Zobay and Garraway, 2000; Estève *et al.*, 2005; Günther, Kemmler, *et al.*, 2005a; Hommelhoff *et al.*, 2005; Kraft *et al.*, 2005). An overview of microtraps based on planar conductor geometries has been given by Davis (2002). Alternatives to flat or round conductors, such as V- and U-shaped conductors, have been proposed by Liu *et al.* (2002). Even helical structures have been tested (Richmond *et al.*, 2002). The latter features a guiding potential that drops exponentially towards the center and leaves the axis of the guiding tube almost field-free. This offers interesting possibilities for spectroscopic applications. Ring traps are possible with solenoids in axial bias fields (Rooijakkers, 2004). By changing the strength of the bias field, the ring can be loaded by exploiting continuous transformation of a spherical quadrupole trap. In the following we describe the realizations of conveyor belts for atoms and three-dimensional positioning systems in more detail.

As an alternative to ballistic propagation, time varying microtraps can be exploited for controlling the atomic motion. By regulating the currents in the conductors, trap geometries can be changed while the atoms are trapped. A pioneering example is a conveyor belt for atoms that has been proposed and demonstrated with thermal clouds (Hänsel, Reichel, Hommelhoff, and Hänsch, 2001b) as well as with condensates (Hänsel, Hommelhoff, *et al.*, 2001). It was developed under the restricting condition of placing all conductors in a single plane and thus avoiding three-dimensional geometries. The center part is a single-wire harmonic waveguide with an external bias and offset field (Fig. 16). The axial potential is modulated by two additional conductors on each side of the center wire. They are periodically patterned with segments oriented parallel and perpendicular to the center wire. The principle of operation is best understood by first looking at the effect of one of the conductors. The field of the perpendicular segments lowers (raises) the offset field locally, resulting in a series of potential wells (barriers). A similar bucket chain is obtained by driving the current in the other conductor, however at a position shifted by half a period. By alternating the current between the two conductors a moving bucket chain is obtained which can be loaded with atoms. The currents are adjusted according to $(I_{M1}, I_{M2}) = I_0(\cos\phi, -\sin\phi)$, with $\phi(t)$ being a function that determines the position of the bucket chain. For $\phi(t) = \omega t$ the buckets continuously move in one direction with a speed given by the frequency ω at which the current alternates.

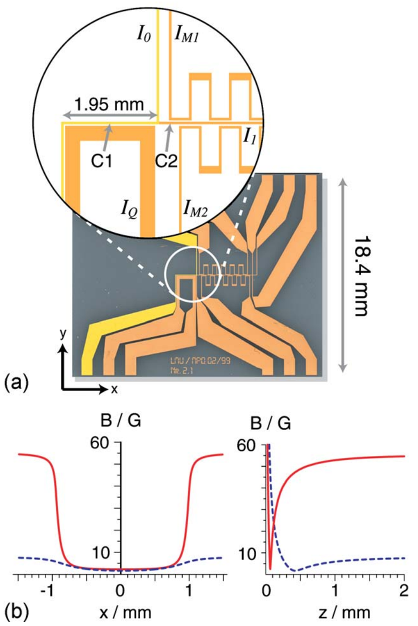

FIG. 16. (Color online) Wire layout of the atomic conveyor belt by Reichel *et al.* (1999) and Hänsel *et al.* (2001). Inset: The relevant part of the conductor pattern. I_0, I_1, I_{M1}, and I_{M2} create the various magnetic potentials for trapping and transport. Adapted from Hänsel *et al.*, 2001.

This scheme was realized with 50-μm-wide (7-μm-thick) gold conductors electroplated on an aluminum nitride substrate. The structure was insulated with an epoxy layer and then coated with a reflective silver layer acting as a mirror for operating a mirror MOT (Sec. IV.A).

A cloud of about 10^5 ^{87}Rb atoms is transferred from the mirror MOT into the first bucket of the conveyor belt at a temperature of 30 μK. By alternating the current with a period of several tens of milliseconds, transport is possible at a speed of a few cm/s. The currents in the center wire and outer wires are 2 A and 1 A, respectively, and I_0 is 1 A. During transport the trapping frequencies in each individual bucket vary by about a factor of 3, giving rise to parametric heating of the cloud. Simultaneously, the position of the buckets undergoes vertical variations of about 0.2 mm. The measured temperature increase can be kept at a level of 5 μK for velocities not faster than 1 cm/s. By optimizing the bias field, the offset field, and the currents I_{M1} and I_{M2} for each axial position, the variation of the trapping frequencies can be kept below 4% and the vertical position shift can be suppressed to below 30 μm (Hommelhoff *et al.*, 2005). With this optimized setup it was possible to transport a rubidium condensate with 3000 atoms at a speed of 1.6 cm/s. An advanced long-distance conveyor belt (6 cm linear distance) based on a dual-layer chip technology has been described by Long *et al.* (2005). Smooth operation of the conveyor was demonstrated using thermal atoms that were translated by distances of up to 24 cm. A further promising idea for a very smoothly operating single-layer conveyor belt has been partially tested with thermal atoms (Hinds, 1999; Rosen-

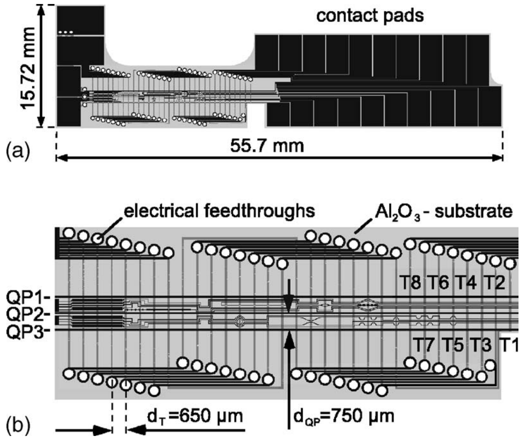

FIG. 17. Chip for three-dimensional positioning of atomic clouds. (a) Schematic plot of the dual-layer microstructure with conductors at both surfaces of the substrate and contact pads on the top. (b) Central part of the chip. Indicated are the conductors QP1, QP2, and QP3 on the top producing the three-wire guide and the transport wires $T1-T8$ on the back surface of the chip. The eight transport wires are periodically repeated underneath the chip. Electrical connection between the separate blocks of $T1-T8$ is achieved by running the wires through laser cut holes from underneath to the top surface of the chip and back. The additional wire pattern between QP1 and QP2 as well as between QP2 and QP3 can be used for generating additional microtraps as described by Kraft *et al.* (2005). From Günther, Kemmler, Kraft, *et al.*, 2005.

busch *et al.*, 2000b). It is based on a set of parallel wires which are placed in a rotating bias field. The resulting set of parallel quadrupole waveguides synchronously moves along the surface. The existence of the moving potential was experimentally verified by scattering of cold thermal atoms.

Using dual-layer technology, alternative geometries are accessible which allow for precise three-dimensional positioning of a condensate on a chip. The scheme introduced by Günther, Kemmler, *et al.* (2005) is based on a three-wire guide with integrated bias field (see Sec. II.D.4). The axial confinement is accomplished by pairs of parallel and equidistant transport wires (37 in total, 32) on the backside of the substrate (Fig. 17). They are oriented perpendicular to the axis of the waveguide and generate an inhomogeneous offset field with local maxima at the position of the wires. Eight neighboring wires form a group. These groups are periodically repeated along the waveguide axis. This way, the scheme can be scaled to arbitrarily long waveguides with a maximum number of eight independent currents. An individual bucket is generated by activating the first and fourth currents such that potential barriers occur at positions the first and fourth wires of each group. The bucket is moved to the next axial position by ramping up currents 2 and 5 while ramping down currents 1 and 4. This scheme is flexible and has the advantage of smooth transport. By optimizing the currents in the transport wires, the axial trapping frequency of an individual bucket remains unchanged during the transport. Variations of the radial frequencies can be compensated by controlling the currents in the three-wire guide. The lateral (horizontal) variation of the trap center during transport remains below 1.3 μm. A detailed discussion of the field configuration can be found in Günther, Kemmler, *et al.* (2005). Transporting thermal clouds does not require this optimization. Thermal atoms can adiabatically follow slight potential changes; thus, the variation of the radial and axial trapping frequencies by 7% and 14%, respectively, during a nonoptimized transport is tolerable. Another advantage of this geometry is that all magnetic fields are generated on-chip and no external fields are required. External fields generated by macroscopic elements are usually hard to control with a high precision due to geometric uncertainties and temporal drifts. The exclusive use of microfabricated on-chip electromagnets facilitates the generation of a stable and reproducible field geometry. In addition to the transport along the axial direction, fully three-dimensional (3D) positioning is possible by controlling the currents in the three-wire guide. The experiment was carried out with electroplated gold conductors on both sides of a 250-μm-thick aluminum oxide substrate. The conductors are 100 μm wide and 6 μm thick and sustain a maximum continuous current of 1.35 A. The three waveguide conductors are each separated by 750 μm, and the comb of transport wires on the back side of the substrate has a period of 650 μm. The total length of the comb is 20.15 mm. The corresponding wires of the different groups are connected at the front side of the substrate. Contact is made through laser cut holes of 400 μm diameter and electroplated gold on the inner surface of the holes. For transport and positioning the currents in the center wire and the outer conductors of the waveguide are typically 0.85 and 0.235 A, respectively. The transport wires carry a current of 0.6 A. The buckets are generated 300 μm above the surface with trapping frequencies of $(\omega_a,\omega_r)=2\pi\times(16,140)$ s^{-1}. Transport along the axis was tested with a thermal cloud of 1.5×10^5 ^{87}Rb atoms at a temperature of 6 μK. The cloud was accelerated over 500 ms to a velocity of 2.6 mm/s with a maximum acceleration of 8.2 mm/s^2. Then it was moved for 250 ms at a constant speed of 2.6 mm/s before stopping by an inverted acceleration ramp. After a total time of 1.25 s the cloud arrived at rest (without sloshing). The total distance of transport was thereby 1.95 mm. Positioning of a condensate is best achieved by moving a thermal cloud slightly above the critical temperature and subsequently generating a condensate by a short pulse of forced evaporation. Sloshing and shape oscillations of the condensate are minimized this way.

The precision and 3D capability of such a positioning system can be exploited for stopping the center-of-mass motion of the condensate, such as, for example, a residual sloshing inside the trap in an arbitrary direction. Since the sloshing motion is usually excited at some stage during the experiment by some unwanted but recurring effect, it occurs with a reproducible phase. Once the amplitude and phase of the sloshing are measured, the trap minimum can be shifted to the turning point of the sloshing oscillation where the condensate comes to rest. The residual motion can be reduced to below 0.1 mm/s (Günther, Kemmler, *et al.*, 2005) with this method. Such conditions provide a good starting point for releasing clouds of nonthermal atoms into waveguides in the quasi-1D regime with a well-controlled energy. In the same work, the high precision of spatial positioning was utilized for demonstrating a direction sensitive magnetic field microscope.

E. Microfabrication techniques

Microtraps are typically made by microfabricating electric conductors on a substrate by standard lithographic methods. While this method is favorable for structures on the scale of several 100 nm up to 100 μm, larger structures are usually made by using normal copper or gold wires or even metal bars that have been shaped by standard machining. Such millimeter-sized conductors are often used for generating the bias field or for creating intermediate traps used during the loading procedure. For making simple guides with strong confinement it is sufficient to cement a thin copper wire onto some surface or at the edge of a bar (Fortágh, Grossmann, Zimmermann, and Hänsch, 1998). Reasonable traps with wire diameters of down to 50 μm can be realized this way without going through the involved procedure of lithographic microfabrication. Similarly, microtraps have also been demonstrated with wires embedded in a mirror surface (Jones, Vale, Sahagun, Hall, and Hinds, 2003). Recently, a microtrap was created with a standard milling machine by machining grooves into a silver film (Vale *et al.*, 2004). The most important fabrication techniques, however, use electroplating or evaporative deposition. Various examples have been reported in Drndic *et al.* (1998), Key, Hughes, *et al.* (2000), Reichel *et al.* (2001), Fortágh, Ott, Schlotterbeck, *et al.* (2002), Reichel (2002), Fortágh *et al.* (2003), Jones, Vale, Sahagun, Hall, and Hinds (2003), Estève *et al.* (2004), Groth *et al.* (2004), Lin *et al.* (2004), Vale *et al.* (2004). Advanced techniques of microfabrication can be adopted from material sciences. A very good, practical introduction to microtrap fabrication has been given by Lev (2003). Before looking at two of the production methods in more detail we introduce the thermal properties of miniaturized current conductors. The thermal properties of the conductors are important to the success of using miniaturized geometries in order to obtain strongly confining traps.

1. Thermal properties of microstructures

The maximum current density supported by a conductor before it melts depends on its thermal coupling to the environment. Since microtraps are operated in vacuum at temperatures where thermal radiation is negligible, the dissipated heat is essentially removed by conduction to the substrate. The temperature distribution in the conductor can be derived by solving the equation of heat transport

$$\dot{T} = \frac{1}{\rho_m C}(\lambda \nabla^2 T + \eta). \tag{58}$$

Here ρ_m is the mass density of the conductor, C is the specific heat capacity per unit volume, λ is the thermal conductivity, and η is the source term. For Ohmic heating the source term takes the form $\eta = \rho_{\mathrm{el}} j^2$, where ρ_{el} is the electric resistivity and j is the current density. For a cylindrical conductor with radius r_0, surrounded by a heat reservoir at the temperature T_0, the steady-state radial temperature distribution is given by $T(r) = (\rho_{\mathrm{el}}/4\lambda) j^2 (r_0^2 - r^2) + T_0$. Henceforth, the temperature dependence of the resistivity is neglected. Assuming the temperature difference ΔT between the center and surface of the conductor, the current density j responsible for ΔT scales inversely with the wire radius r_0: $j = \sqrt{(4\lambda/\rho \Delta T)}(1/r_0)$. This inverse scaling is the reason why miniaturized conductors are fundamentally advantageous for generating strong magnetic confinement. At the surface of a cylindrical wire of radius r_0, for example, the magnetic field, the gradient, and the curvature scale as $B(r_0) \propto j r_0$, $\nabla B(r_0) \propto j$, and $\nabla^2 B(r_0) \propto j/r_0$, respectively. Thus miniaturization and the corresponding increase of the maximum tolerable current density increase the maximum achievable magnetic confinement. Similar arguments apply for only partially embedded conductors, such as conductors fabricated on a substrate. A flat conductor of width w produces its largest magnetic field gradient at a distance which is comparable to the width. Accordingly, $B(w) \propto j$, $\nabla B(w) \propto j/w$, and $\nabla^2 B(w) \propto j/w^2$ (Drndic *et al.*, 1998). In general, the optimization of the conductor geometry is a complex problem. The thermal properties of the conductor, substrate, interfaces, boundary conditions, etc., have to be taken into account.

Heat transport from a thin microfabricated metal layer to a substrate has been analyzed by Groth *et al.* (2004). Using a simple two-dimensional model, two distinct time scales, a fast and a slow time scale, were identified which are relevant in heat removal from the metal wire. The model was successfully used in the quantitative analysis of experimental data shown in Fig. 18. Heat transport from a thin metal layer of width w and height h to the substrate takes place on a short time scale

$$\tau_{\mathrm{fast}} = C_W h/(k - h j^2 \alpha \rho_{\mathrm{el}}). \tag{59}$$

Here C_W is the heat capacity per volume of the wire, ρ_{el} is the cold resistance, and α is the linearly approximated temperature coefficient of the resistance. τ_{fast} is essentially determined by the thermal conductance k of the interface between the wire and substrate. The thermal conductance of the metal is considered here to be infinite. It is in fact several orders of magnitude larger than the thermal conductance of the insulating layer (interface) between the metal and substrate. Tests of gold conducting layers of a few micrometer thickness resulted in τ_{fast} being on the order of a microsecond. The gold layers were deposited on different substrates such as sap-

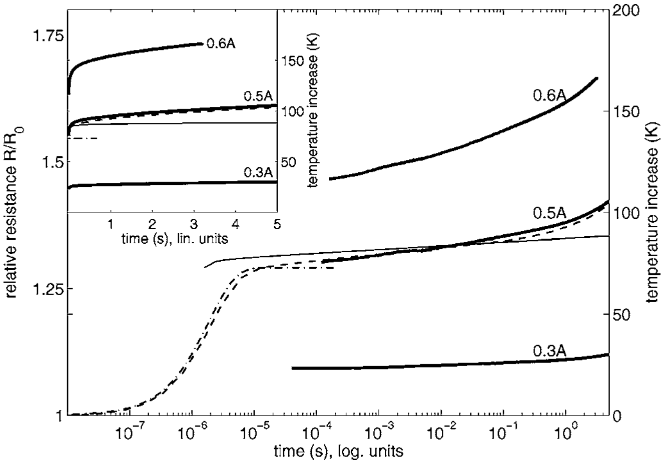

FIG. 18. Temperature evolution of a 5 μm wide and 1.4 μm thick wire mounted on a 700 μm thick Si substrate with a 500 nm SiO$_2$ insulating layer (interface). The thick solid curves show measured data for 0.6, 0.5, and 0.3 A current pulses. In one case (0.5 A) the theoretical predictions (without fitting parameters) are also shown. The initial fast temperature increase (thin dash-dotted curve) occurs on a microsecond time scale. The analytical model for the heat transport through the substrate (thin solid curve) holds only as long as the approximation of an infinite plane substrate is valid. A two-dimensional numerical model (dashed curve) accurately reproduces the measurements. Adapted from Groth *et al.*, 2004.

phire, GaAs, and Si, all covered by a SiO$_2$ insulating interface. The temperature difference between the wires and the substrate evolves as

$$\Delta T_{\mathrm{fast}}(t) = \frac{h\rho_{\mathrm{el}} j^2}{k - hj^2\alpha\rho_{\mathrm{el}}}(1 - e^{-t/\tau_{\mathrm{fast}}}) \tag{60}$$

and saturates almost instantaneously. A small temperature difference between the conductor and substrate is preferable. Therefore, the insulating layer should be as thin as possible. Best results were reported for the thinnest tested SiO$_2$ insulating layer (20 nm). At a current density of $j = 10^7$ A/cm^2, the asymptotic temperature difference was 50 K. Once ΔT_{fast} saturated, the wire warms up on a time scale which is determined by the total heat dissipation and thermal properties of the substrate. In the two-dimensional model, the substrate is considered as an infinite half-space having a thermal conductivity λ and a heat capacity per volume C. The linear heat source (wire) is placed on the surface. The temperature increase of the substrate just below the heat source is given by the incomplete Γ function

$$\Delta T_{\mathrm{slow}} = \frac{hw\rho_{\mathrm{el}} j^2}{2\pi\lambda}\Gamma\left(0, \frac{Cw^2}{4\pi^2\lambda t}\right) \approx \frac{\rho_{el} Ij}{2\pi\lambda}\ln\left(\frac{4\pi^2\lambda t}{Cw^2}\right). \tag{61}$$

The temperature dependence of the electric resistance ρ_{el} is neglected. From Eq. (61), it follows that wider wires warm up faster than narrow wires for equal current density. Furthermore, heat transport is faster in Si compared to other substrates ($\lambda_{\mathrm{GaAs}} \approx \lambda_{\mathrm{sapphire}} \approx \lambda_{\mathrm{Si}}/3$). The optimal substrate has a large heat conductivity and heat capacity and is in good thermal contact with the wire. Si substrates with thin oxide surface layers showed the best thermal properties as well as good surface quality. For thin substrates, heat transport from the substrate to other heat sinks must be taken into account.

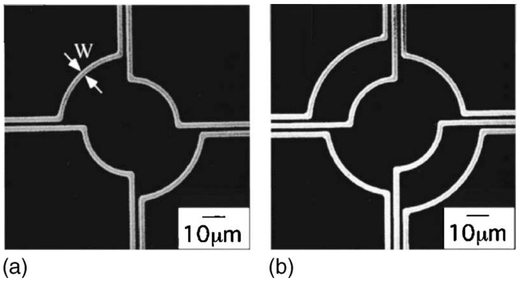

FIG. 19. Scanning electron microscopy images of microconductors with geometries for trapping atoms as suggested by Weinstein and Libbrecht (1995) and fabricated by Drndic *et al.* (1998). The gold wires ($w = 3$ μm and $h = 1$ μm) are fabricated on sapphire substrates. (a) Two half loops. (b) Three concentric half loops. From Drndic *et al.*, 1998.

2. Electroplated microstructures

Microstructures following the trap geometry suggested by Weinstein and Libbrecht (1995) were fabricated by Drndic *et al.* (1998) (Fig. 19). The wire geometry was initially defined on a sapphire substrate (0.5 mm thick and 2.5 cm in diameter) using photolithography. Subsequently, a layer of 100–400 nm Au was evaporated on the top of a 5 nm Cr adhesion layer. The gold wire was then electroplated up to 3 μm thickness. The outstanding electrical properties of the fabricated wires were demonstrated by measuring the maximum tolerable current density under experimentally realistic conditions: in vacuum at room temperature and at cryogenic temperatures of 100 and 20 K. An extended wire pattern with parallel conductor segments of 20 μm width, 3 μm height, and 24 μm period, covering a substrate area of 2×2 mm^2, tolerated a maximum current density of 10^8 A/cm^2 at 20 K temperature (dc operation). This value exceeds the typical critical current densities of superconductors, e.g., Nb, NbTi, or Nb$_3$Sn. The maximum current density of superconducting devices made of niobium wires on silicon substrates was measured to be 2.5×10^6 A/cm^2 at 4.2 K.

The process of fabricating thin copper wires with high length to width ratios and good conducting properties was reported by Fortágh, Ott, Schlotterbeck, *et al.* (2002). Parallel copper conductors 3 μm thick, with widths ranging from 3 to 30 μm and separated by 1 μm, were produced with a total length of 25 mm (Fig. 20). Initially, a high-quality optical mask was prepared by electron beam lithography which was then employed to transfer the wire pattern to a sapphire substrate (750 μm thick). In order to guarantee good adhesion and provide a contact layer for subsequent galvanic processing, the substrate was coated with a thin metallic layer (7 nm Cr followed by 120 nm Cu) by thermal evaporation. The

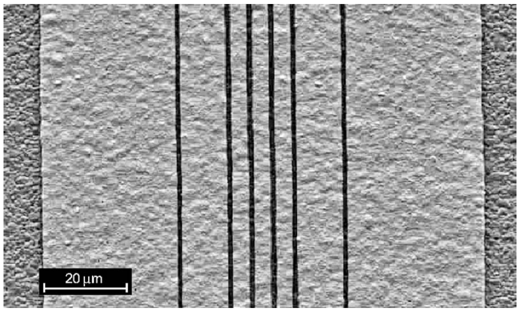

FIG. 20. Electron micrograph of a typical microstructure, showing a segment of the electroplated wire geometry. The wire widths are 30, 11, and 3 μm, and the nominal separation between wires is 1 μm. The image shows the grained structure of the electroplated wires, which is here partially due to the roughness of the sapphire substrate (~500 nm). From Fortágh, Ott, Schlotterbeck, *et al.*, 2002.

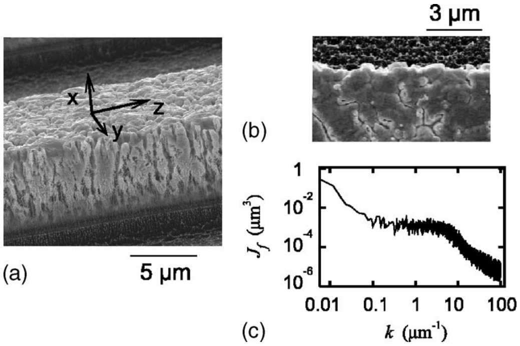

FIG. 21. Imperfections of the geometry of an electroplated wire. (a) Scanning electron microscopy (SEM) image from the side and (b) from the top. (c) J_f is the spectral density of the spatial fluctuation of the wire edge as derived from the SEM image. From Estève *et al.*, 2004.

wire production itself was done in a conventional galvanic bath using the technique of pulsed electroplating. A test structure with a 1.6 μm copper layer was used to determine the critical current at which the conductors are thermally damaged. The measurements were carried out at room temperature, in air with the microstructure mounted on a copper heat sink. Maximum current densities of 3.1×10^6, 4.8×10^6, and 6.5×10^6 A/cm^2 have been reached for the 30, 11, and 3 μm conductors, respectively. The maximum current density increased with decreasing width, because the geometry of the thin wire provides more efficient heat transfer to the substrate. The resistance of the 30, 11, and 3 μm wide conductors increased by a factor of 2.5, 2.3, and 1.5, respectively, before the thermal damage. At small imperfections, which may be caused by unintentional variation of the conductor cross section or by reduced adhesion of the substrate, the temperature is expected to exceed the average value and leads to breakdown. The role of small imperfections is most pronounced in the smallest of the wires that explains the reduced critical resistance at breakdown.

Electroplating results in a grained structure of the conductor. This has relevant consequences such as distortions of the magnetic trapping potential at close distances to the current carrying wire (Sec. V.D.2). Figure 21 illustrates the rough geometry and spectral distribution of spatial variations of the wire edge (Estève *et al.*, 2004). Nevertheless, spatial modulations of the magnetic field which are related to the roughness of the current carrying wire average out for distances large enough compared to the characteristic length scale of the roughness. Thus at large distances to the conductor (typically a few hundred microns) electroplated structures produce smooth magnetic potentials and are suitable for the manipulation of atomic clouds. Electroplating allows the production of structures on the centimeter scale. Such microstructures combine the advantages of large currents and precise geometry. Applications such as carrier chips, conveyor belts, and for positioning of atomic clouds using electroplated microstructures are described in the previous section.

3. Evaporated thin films

The fabrication of high-quality microstructures using lithography and evaporation of metal films has been characterized by Groth *et al.* (2004). On substrates of Si and GaAs covered with a SiO$_2$ insulation layer, 1 to 100 μm wide conductors with thickness ranging from 1 to 5 μm have been fabricated. To allow the evaporation of thick metal layers, up to 5 μm thick films of image-reversal photoresist were deposited onto the substrates. The resist was exposed to UV light through an electron-beam-patterned mask. After developing the resist structure, a Ti adhesion layer (35 nm) and a thick Au layer (1–5 μm) were deposited. The gold-covered photoresist was removed in a lift-off procedure using acetone and isopropanol solvents. Some of the chips were covered with a thin protection layer of Si$_3$N$_4$. Finally, the chips were cut or cleaved to the desired dimension of 25×30 mm^2. The resulting gold surface is smooth (grain size <80 nm) as illustrated in Fig. 22. The roughness depends on the adhesion properties and substrate roughness. Better results have been obtained on Si and GaAs than on sapphire. The wires on the chip were defined by micron-sized grooves on the otherwise uniform gold surface. Current and voltage characteristics of the chips have been tested in vacuum (10^{-6} mbar). Si and GaAs substrates tolerated >300 V across a gap of 10 μm, sapphire >500 V. Current densities of more than 10^7 A/cm^2 have been measured. The chip surface also represents a high-quality mirror, used for the operation of a mirror MOT (Sec. IV.A.2).

III. THEORETICAL WORK ON INTEGRATED ATOM OPTICS

A number of theoretical studies have been published which refer to, or are inspired by, the possibilities provided by magnetic microtraps. However, theoretically studied scenarios can often be realized also with other

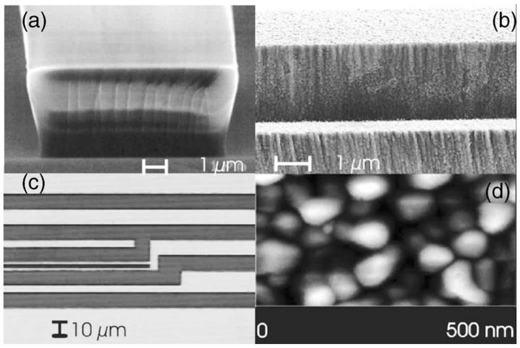

FIG. 22. Microscope images of chip details, during and after the fabrication. (a) Scanning electron microscopy image of the photoresist structure. Its thickness is 4.5 μm; the undercut is 0.6 μm. (b) Scanning electron microscopy image of a typical fabricated wire. (c) 1, 5, and 10 μm wide gold wires on a fully fabricated chip. (d) Atomic force microscopy picture of the gold surface. The grain size is 50–80 nm. From Groth *et al.*, 2004.

trap types such as optical dipole traps or optical lattices. Here, we summarize only some works which are particularly important for magnetic microtraps. Basic questions are concerned with the propagation of atoms in straight or bent waveguides and in beam splitters such as Y junctions and optical couplers. Such scenarios are closely related to the splitting of an atomic wave function in a double-well potential which can be exploited for the construction of a temporal interferometer. The publications reviewed in this section mainly treat the dynamics of single atoms. Interaction comes into play only as an additional effect. Until now, there were no experiments made with single atoms in microtraps due to the lack of suitable single-atom detectors. Considerable effort is currently invested in the development of on-chip single-atom detection (for references see Sec. VI). Thus a new class of single-atom experiments can be expected in the near future. In view of this development a summary of the basic theoretical approaches is presented here.

A. Adiabatic propagation of noninteracting atoms in straight waveguides

The physics of atomic matter waves in waveguides can be described by the Schrödinger equation. In principle, solutions for an arbitrary geometry can be obtained numerically. However, despite the computational capability of modern computers it is still difficult to treat the general problem. Simplifications are necessary.

Jaaskelainen and Stenholm (2002b) studied the wave propagation of noninteracting atoms in a simplified 2D geometry with only one axial and one radial degree of freedom. The results provide some qualitative insights into the relevant effects and conditions for which simplifications are possible in the fully 3D case. The analysis starts with a Schrödinger equation in a two-dimensional configuration space. The Cartesian x and y coordinates are transformed into a frame with the path length s along the valley of minimum potential energy and the distance ξ transverse to the minimum path. Furthermore, the solution $\Psi(s,\xi,t)=\Sigma_n \phi_n(s,t)\,\eta_n(s,\xi)$ is expanded in a set of transverse eigenfunctions $\eta_n(s,\xi)$ and a set of unknown longitudinal wave functions $\phi_n(s,t)$. The transverse functions satisfy a one-dimensional Schrödinger equation with s as a parameter. To a good approximation, the transverse potential is harmonic and the transverse functions $\eta_n(s,\xi)$ can be taken as harmonic oscillator states. With these definitions, a one-dimensional Schrödinger-type equation is derived for each of the longitudinal states $\phi_n(s,t)$. The equation contains additional terms which couple the longitudinal states. The coupling is associated with temporal changes of the potential which appear after changing into the reference frame of the moving atom. Bending of the atom's trajectory induces Coriolis-type pseudoforces which couple transverse states of different parity. Curvature changes of the transverse potential, such as bottleneck restrictions or spatial expansions, induce transitions between states of equal parity. In the case of bottleneck restriction coupling occurs if the adiabaticity condition

$$\frac{(2\pi)^2\hbar}{m\lambda\omega_0^2}\frac{\Delta\omega}{L} \ll 1 \tag{62}$$

is violated. The left term is the so-called Massey parameter. Here m and λ are the mass of the atom and the characteristic longitudinal de Broglie wavelength associated with the motion along the atom's trajectory. The ratio $\Delta\omega/L$ is a measure of the change of the transverse trapping frequency $\Delta\omega$ over a typical distance L. Extended numerical tests reveal that the adiabatic approximation is valid only if another condition is also fulfilled. It originates from the transverse dispersion of a wave packet that enters a range in the guide where the transverse confinement rapidly relaxes. If the wave packet spread is slower than the opening of the potential (in the atom's frame), adiabaticity is not fulfilled. The condition can be quantified as

$$\frac{2\pi}{L\lambda\omega_0}\left(1-\frac{1}{\sqrt{1+\Delta\omega/\omega_0}}\right) < 1. \tag{63}$$

In close analogy to classical fiber optics, the condition can also be expressed in terms of the Fresnel number N:

$$Ng(\Delta\omega/\omega_0) < 1, \tag{64}$$

with

$$N = \frac{\hbar}{mL\lambda\omega_0} \tag{65}$$

and the function

$$g(\Delta\omega/\omega_0) = \frac{2\pi m}{\hbar}\left(1-\frac{1}{\sqrt{1+\Delta\omega/\omega_0}}\right). \tag{66}$$

Comparison between the full numerical solution and solutions obtained with the adiabatic approximation shows that adiabaticity can be achieved even when the Massey parameter is larger than unity, provided that the Fresnel number is sufficiently small; i.e., the changes occur over a length scale larger than the Rayleigh length. According to time-reversal symmetry, adiabatic behavior is the same for expansion and bottlenecks.

The same approach can be applied to a terminated waveguide with a rapidly decreasing transverse confinement at its end. Transverse oscillator energy is redistributed into kinetic energy of the released particle if the Fresnel number of the opening is larger than unity. For $N<1$ the released wave packet is simply given by the solution of the free Schrödinger equation with initial conditions set by the wave packet inside the waveguide. Analytic expressions for this case have been given by Jaaskelainen and Stenholm (2002a). By using such an abrupt ending waveguide the excitation of transverse states inside the waveguide could be monitored by absorption imaging of the released wave packet after some time of flight during which the shape of the wave packet expands to a detectable size.

With a similar approach adiabatic propagation of noninteracting atoms is treated also in bent waveguides (Bromley and Esry, 2003, 2004).

B. Beam splitters and "optical" couplers

A beam splitter formed by two approaching wires in a parallel bias field [Fig. 12(a)] has been studied in a fully 3D calculation by Stickney and Zozulya (2003). A propagating atomic wave packet is described by the Gross-Pitaevskii equation which includes the atom-atom interaction as a nonlinear term in a Schrödinger-type equation. The starting assumption for a solution is written as a plane wave with wave vector k_p propagating in the axial direction (z coordinate) with a slowly varying amplitude $\phi(T,\vec{R})$ that depends on time T and position $\vec{R}$ measured in the atom's reference frame. Furthermore, a number of assumptions are made. First, the kinetic energy of the wave packet's center-of-mass motion is taken to be larger than the transverse energy spacing of the trapping potential. This condition can be expressed in terms of the radius of the radial ground state a_0 and the wave vector k_p as $k_p a_0 \gg 1$. With this assumption, small changes of the group velocity during passage of the beam splitter can be neglected. Second, it is assumed that $k_p L \gg 1$ with L being the characteristic spatial scale of the wave packet. In this case, reflection due to a change in the shape of the potential is exponentially small. More importantly, however, the second derivative of the amplitude with respect to z is assumed to be small and is neglected. Third, the kinetic energy associated with the expansion of the wave packet due to the repulsive atomic interaction should be small compared to the radial energy spacing of the trap. This ensures that atomic interaction cannot induce radial excitations of the wave packet. Finally, the interaction should not significantly change the phase and length of the wave packet while it passes the beam splitter. Inserting all this into the Gross-Pitaevskii equation results in an equation for the envelope:

FIG. 23. Schematic view of the splitting region. Parameter β_x increases from the lower left to the upper right passing through $\beta_x=1$ in the center when two waveguides merge into one. From Stickney and Zozulya, 2003.

$$i\frac{\partial}{\partial t}\psi(x,y,t)=\left[-\frac{1}{2}\nabla_\perp^2+U(x,y,t)+P|\psi|^2\right]\psi(x,y,t). \tag{67}$$

Time and coordinates are normalized to the inverse of some fixed characteristic radial trapping frequency ω_0 and the corresponding radial ground-state radius $a_0=(\hbar\omega_0/M)^{1/2}$. The beam splitter is described by the reduced potential $U=V/\hbar\omega_0$ with V being the beam splitter potential as seen from the moving wave packet. The parameter P describes the atomic interaction and contains the scattering length a_s, the atom number N, and the length of the wave packet L_{BEC}. It can be approximated by $P\approx 4\pi a_s N/L_{\mathrm{BEC}}$. The wave function $\psi(x,y,t)$ is normalized to unity with respect to the radial coordinates x and y. For a slowly propagating wave packet, the temporal change of potential $U(x,y,t)$ is also slow. In this adiabatic limit the equation can be analyzed with a fixed $U(x,y,\beta)$ taken for a given value of β that parametrizes the local cross section of the beam-splitter geometry (Fig. 23).

The spectrum and eigenfunctions of transverse modes can be determined numerically for different β, i.e., for different positions along the beam splitter. In Fig. 24 the result is shown for ^{87}Rb in the $m_F=-1$ hyperfine low-

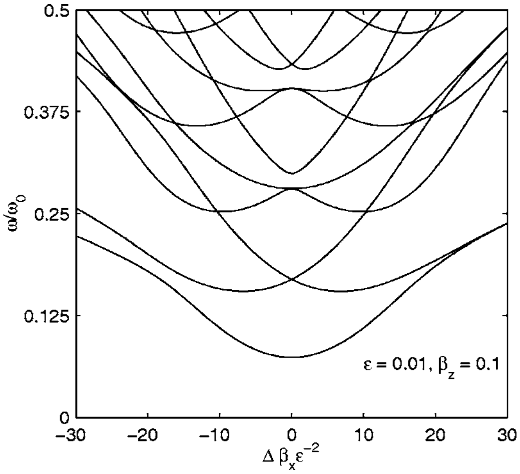

FIG. 24. Several lowest eigenfrequencies of the splitting region versus transverse bias field for $\varepsilon=0.01$ and $\beta_z=0.1$. From Stickney and Zozulya, 2003.

field-seeking state. The beam splitter is made of two wires with a separation d, a bias field of 20 G, an offset field of 2 G, and a critical separation $d_{\mathrm{split}}=25\ \mu\mathrm{m}$ at which the two waveguides merge. The parameter $\Delta\beta_x := \beta_x - 1 = d/d_{\mathrm{split}} - 1$ expresses the separation between the wires and changes sign at the coalescence point. The reference frequency ω_0 is specified by the radius of the transverse ground state in terms of the dimensionless parameter $\varepsilon := 2a_0/d_{\mathrm{split}} = 8\times10^{-3}$, while the atomic interaction is neglected ($P=0$). Negative $\Delta\beta_x$ correspond to that side of the junction where two channels are vertically stacked (Fig. 23). For positive $\Delta\beta_x$ the trap consists of two horizontally arranged channels. At $\Delta\beta_x=0$ the four channels meet at the coalescence point and form a linear hexapole. In the limit of large and positive $\Delta\beta_x$ the energies of the modes are pairwise degenerate, which reflects the symmetry of the two channels. The wave functions can be written as a symmetric and an antisymmetric superposition of the individual wave functions in the two channels. Following the energy curves in Fig. 24 one finds that the symmetric ground state at large and positive $\Delta\beta_x$ is mapped to the ground state of the upper channel at negative $\Delta\beta_x$. The antisymmetric partner is mapped to the first excited state in the upper channel. For an adiabatic passage from negative to positive $\Delta\beta_x$ atoms in the ground state of the upper channel would be coherently decomposed into a symmetric superposition of individual wave packets in both channels at the output side of the junction (positive $\Delta\beta_x$). The general mapping behavior can be summarized as follows: an input mode maps onto the lowest available output mode with the same parity along the x axis (which is the direction parallel to the surface and perpendicular to the guide axes). The adiabatic condition can be written as $L_0\varepsilon^2\omega_0/v \gg 1$, with v and L_0 being the axial velocity of the wave packet and the characteristic length of the beam splitter, respectively. If the ground state of the lower channel is used as input (negative $\Delta\beta_x$), atoms are transferred to the first exited symmetric state at the output (positive $\Delta\beta_x$). During this passage other modes are crossed. An expanded view of the spectrum reveals that some of these crossings are in fact avoided crossings. For small input velocities the mapping becomes incomplete and distorted due to Landau-Zener coupling between the modes. The appearance of anticrossings makes the analysis of the mapping properties for higher modes progressively more complex.

While the nonlinearity has no pronounced effects in the splitting process it becomes important for recombining two wave packets (Stickney and Zozulya, 2002). As wave packets come in from positive $\Delta\beta_x$ in the ground states of the left and right channels, they leave the beam splitter in the first two modes of the upper channel at negative $\Delta\beta_x$. In the adiabatic limit and for sufficiently small nonlinearity, one can restrict the analysis to two modes present at the input and their behavior during the adiabatic passage. From the above wave equation two coupled differential equations for the two mode amplitudes can be derived and integrated with the result shown in Fig. 25. The relative population of the lowest mode in the output channel is plotted for various phase differences of the two input waves. With increasing atomic interaction the population of the lowest mode grows at the expense of the population in the higher-lying output mode. This effect becomes more pronounced with an increase in the length of the splitting region, i.e., for better adiabaticity. A stability analysis of the equations shows an instability with positive growth rate for $\Delta\beta_x$ above a critical value which depends on P. A simplified model reveals the physical origin of the instability by identifying a mode with an excitation frequency that decreases with increasing $\Delta\beta_x$. The instability occurs when the frequency reaches zero and the mode becomes soft. Further increase in $\Delta\beta_x$ makes this mode unstable.

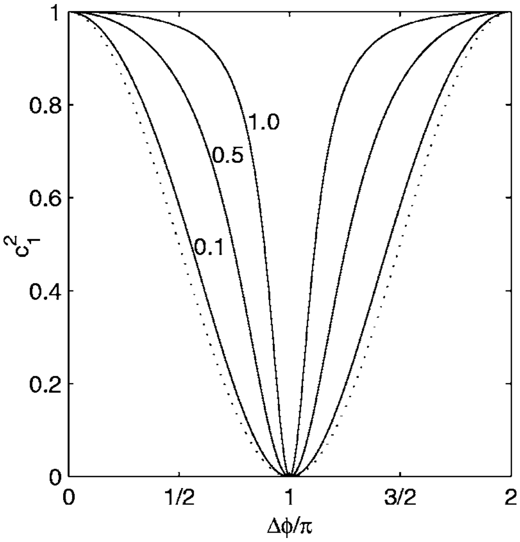

FIG. 25. Output population of the lowest mode $(0,0)_u$ as a function of the relative phase shift for several values of the nonlinearity parameter P. From Stickney and Zozulya, 2003.

The analysis can also apply to an optical coupler (Fig. 26). The passage starts with a large and positive $\Delta\beta_x$. If the minimum separation between wires is reached, $\Delta\beta_x$ stops and eventually returns to large and positive values. It turns out that the optical configuration is far more tolerant to a large rate of change of $\Delta\beta_x$. Adiabaticity is still fulfilled in a regime where the modes in a Y junction

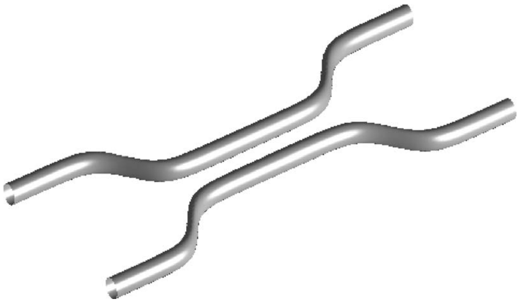

FIG. 26. Schematic view of the splitting region for an optical coupling case. From Stickney and Zozulya, 2003.

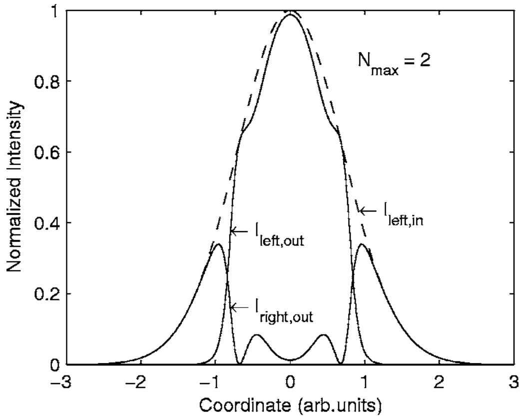

FIG. 27. Input and output intensities in the left and right arms of the beam splitter. From Stickney and Zozulya, 2003.

already undergo strong nonadiabatic transitions. However, the coupler is far more sensitive to the nonlinearity. Figure 27 shows the shape of a wave packet sent in along the left guide of the coupler (dashed line). The shape of the two output wave packets is strongly distorted (solid lines). The low-density wings undergo complete transfer into the right waveguide but the transfer for higher densities at the center is suppressed due to the higher values of the nonlinearity. The effect sets in if the nonlinearity P is comparable to the relative frequency splitting between the two modes due to tunnel coupling.

The optical coupler has also been analyzed by Bortolotti and Bohn (2004). The interatomic interaction is neglected but the nonadiabatic coupling between the different adiabatic transverse modes is treated in detail with methods known from scattering theory. Far from the coupling zone the wave functions are easily found as the product of the transverse modes and longitudinal plane waves. At the boundary of the coupling zone these input and output states must be matched to the nontrivial solutions inside the coupling zone. Once the full solutions are found it is possible to generate a scattering matrix, which contains the coupling between the input and output states. For solving this matching problem the only required information is the value of the logarithmic derivative b. It contains the relevant information on the wave function and its derivative at the boundary of the scattering zone. Thus, one has to find solutions inside the coupling zone with b constant. This is done with the R-matrix method that seeks for solutions with constant b at the boundary. For a given energy the linearly independent eigenfunctions are characterized by their b values, which are found with the variational method. It leads to a set of eigenchannels with eigenvalues b. With this method nonadiabatic coupling is described as well as reflection due to diffraction which occurs if the waveguide potential spatially varies on a scale similar or shorter than the longitudinal de Broglie wavelength of the wave packet. Nonadiabatic mode mixing can be thought of as radial sloshing of the wave packet, but even if the excited mode is energetically inaccessible they still can affect the phase of the ground mode. An adequate description of a Mach-Zehnder interferometer must therefore fully include nonadiabatic coupling. Some results are shown in Fig. 28.

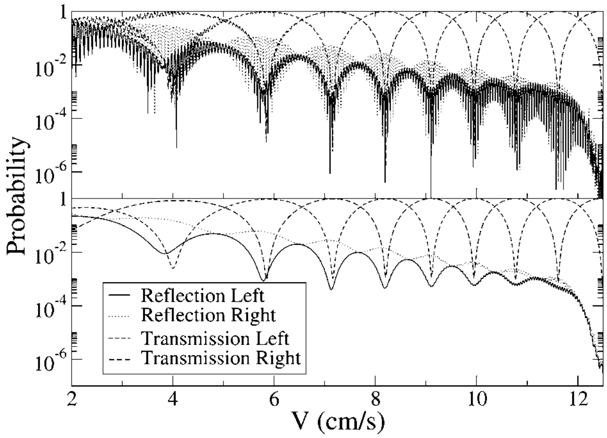

FIG. 28. Probability for exit in the various arms of the beam splitter vs incident atom velocity. This assumes that the atoms have entered in the lowest mode of the left arm. The velocities shown correspond to atom energies below the second threshold, thus suppressing higher-mode excitations. The bottom panel is a 26 μK Gaussian convolution of the one above. From Bortolotti and Bohn, 2004.

Results are presented for the optical coupler under the somewhat extreme conditions of a 2 μm long coupling zone, an offset field of 1 G, a wire separation of 200 nm, and a bias field that varies from 22.5 G outside the coupling zone to 21.3 G at the center of the coupler where the two waveguides are closest. With increasing velocity of wave packet entering at the left the input channel, reflection, and transmission into all four ports vary strongly. For small velocities diffraction leads to pronounced reflection, which is stronger for backscattering into the right input port. Transmission into the two output ports varies strongly with velocity such that it should be possible to find the proper conditions for 50% beam splitting. The analysis also reveals maxima of the mode energies near the boundary of the coupling zone. They are caused by the bending of the waveguide in which longitudinal energy is transferred into transverse energy. This halts the motion in the longitudinal direction. For very slow input velocities the barrier may totally reflect the wave packet. For long couplers the nonadiabatic coupling and reflection effects are efficiently reduced.

A third approach (Jaaskelainen and Stenholm, 2003) is based on the one described above for adiabatic propagation in linear waveguides. It also starts with the adiabatic modes of the beam-splitter potential. The full solution is constructed by a linear superposition of radial modes with coefficients that vary with the position along the axial direction and also in time. For these coefficient functions a differential equation is derived and solved for a simplified two-dimensional model that neglects one of the two radial dimensions. The propagation of longitudinal wave packets can be analyzed with this model.

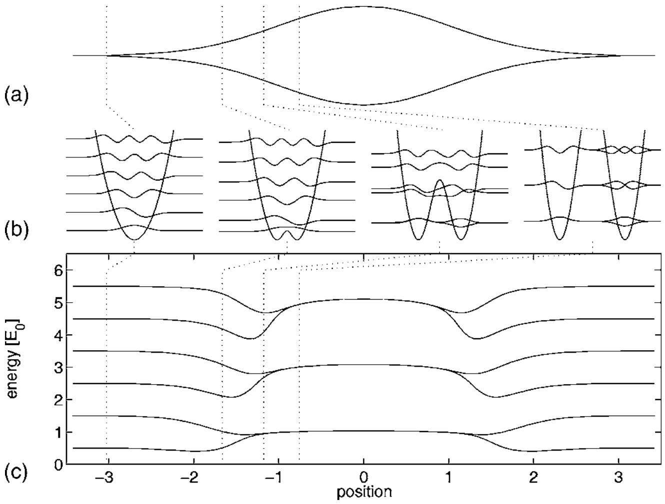

FIG. 29. Guided matter-wave Mach-Zehnder interferometer. (a) Two beam splitters are combined to form the interferometer. (b) Transverse eigenfunctions of the guiding potentials in various places along the first beam splitter. When the two outgoing waveguides are separated far enough so that no tunneling between left and right occurs, the symmetric and antisymmetric states become pairwise degenerate. (c) Energy eigenvalues for the lowest transverse modes as they evolve along the interferometer. From Anderson and Kasevich, 2002.

Insight into the multimode behavior of a matter-wave Mach-Zehnder interferometer can be obtained by a theoretical analysis of a two-dimensional model geometry as shown in Fig. 29 (Andersson *et al.*, 2002). The transverse modes in the input channel can be classified by their parity. Neighboring states with different parity form pairs which become degenerate in the regime of the interferometer where the two channels are well separated. For an adiabatic passage through the interferometer and in the absence of asymmetric perturbations no transitions between the transverse states occur and the interferometer can be decomposed into a superposition of independent two-state interferometers. The occupation of the two states in the output channel of each interferometer depends on the relative phase shift accumulated during the passage. An even phase shift of $(2n)\pi$ restores the initial situation while an odd phase shift $(2n+1)\pi$ swaps the population of the two input states. The phase shift, however, is dispersive; i.e., it depends on the wave vector of the longitudinal motion. At first glance, a thermal wave packet consisting of a large spectrum of longitudinal momentum states is not expected to generate a discernible interference pattern. There is, however, a rephasing effect that may be exploited for recovering interference. It is based on the different longitudinal velocity of transverse modes in the exit channel. If in a two-state interferometer the acquired phase transfers some population from the lower to the higher transverse state, the required energy is taken from the longitudinal motion and this transverse part of the wave packet is slowed by the interferometer. Similarly, transverse pairs with a different longitudinal velocity may be accelerated, gaining longitudinal energy at the expense of transverse energy. A wave packet that does not show interference structure immediately after the interferometer may thus develop fringes after some rephasing time. For the two-dimensional test model a visibility of 30% is derived for a thermal pulse at a temperature of 200 μK, a radial trapping frequency of $2\pi \times 16$ kHz, a length difference between the two arms of 2 μm, and a rephasing time after exiting the interferometer of 20 ms. For a realistic three-dimensional potential similar qualitative behavior is expected. A quantitative analysis has not yet been done.

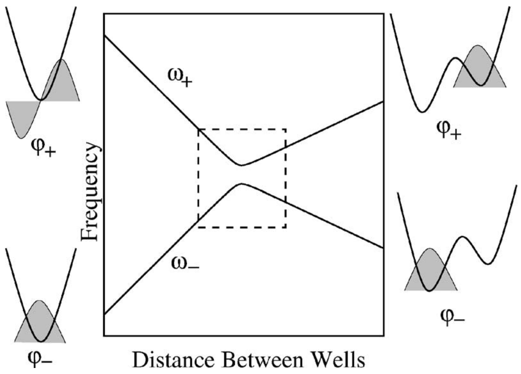

FIG. 30. The eigenfrequencies of the local modes as functions of the distance between the two wells of a double-well trap. An avoided crossing is shown inside the dashed box. Two corresponding eigenmodes of a single-well potential are shown on the left. The eigenmodes, in the limit when the wells are far apart, are shown on the right. These eigenmodes are localized in either the left or right potential wells. From Stickney and Zozulya, 2004.

C. Temporal interferometer

As an alternative to the ballistic interferometers described in the previous section an atom may be placed in a trap that can be continuously transformed into a double-well potential. If the ground state of a single well is split by a slowly growing potential barrier, the two parts may subsequently be exposed to external effects which shift the phase in the two wells differently. A potential gradient would be one example. After some exposure time during which a phase difference is accumulated the barrier is slowly removed and the two parts recombine. For a phase shift of odd multiples of π the population is completely transferred into the first excited state of the single-well potential. For even multiples the ground state is restored. Other values for the phase shift lead to a coherent superposition of the two states.

Of particular importance is the influence of an external potential gradient during splitting and recombination (Zobay and Garraway, 2000; Stickney and Zozulya, 2004). Such a gradient is generated by gravity and can only be avoided if the trap is very carefully balanced. When the trapping potential is split the gradient may lower the energy of one of the wells (Fig. 30). An adiabatic transition between the two geometries maps the initial single-well ground state to the lower-energy ground state of the double-well potential. An initially excited state in the single well is mapped to the higher-energy ground state of the double-well potential. If it is desired to split the initial state into two parts, the transformation of the potential must be sufficiently fast and nonadiabatic. A coherent superposition is now possible, and its generation can be described as a Landau-Zener transition at an avoided crossing. An analytic model for the transition probabilities was presented by Stickney and Zozulya (2004). The visibility of the interference fringes is calculated for various gradients. The result is that the visibility drops with increasing gradient. A reasonable contrast is obtained if the acceleration a, characteristic of the gradient, obeys

$$a < \sqrt{\frac{\hbar\omega}{m}\frac{1}{T}}. \tag{68}$$

T is the characteristic time of the transformation into the double well, m is the mass of the atom, and ω is the eigenfrequency of the initial well. For rubidium in a trap with $\omega = 2\pi \times 200$ Hz that is split into a double well within 8 ms the maximum acceptable gradient is 0.1 $\mathrm{m/s^2}$. The tolerance for asymmetric gravitational potential is thus very small.

The coupling at the avoided crossing can also be exploited for measuring the population distribution in the initial single-well trap (Zobay and Garraway, 2000). An adiabatic passage through the anticrossing will spatially separate the population of the ground and excited states such that they can be detected simply by spatial imaging.

In another work the temporal transformation curve is analyzed and optimized for minimum excitation into higher states (Hänsel *et al.*, 2001a). For a realistic geometry it has been found that the excitation probability is less than 0.1% for a sufficiently slow separation process that lasts at least 30 ms.

IV. QUANTUM-DEGENERATE GASES IN MICROTRAPS

A. Loading Bose-Einstein condensates and Fermi gases into microtraps

Microtraps become increasingly interesting if they can be loaded with atoms at a very low temperature comparable to the energy splitting of the trapped quantum states. A convenient method for selectively occupying trapped quantum states is to start with a degenerate quantum gas, e.g., with a Bose-Einstein condensate or a degenerate Fermi gas. Quantum gases can be loaded directly into a microtrap, e.g., from another magnetic or optical potential by means of optical tweezers. Alternatively, ultracold gases can be cooled to quantum degeneracy inside microtraps using standard techniques of forced evaporation or sympathetic cooling (Hess, 1986; Masuhara *et al.*, 1988; Ketterle and van Druten, 1996). In this case it is sufficient to load an optically precooled atomic cloud into the microtrap. Optical cooling is usually done at a relatively large distance from the chip surface, either in a conventional MOT or in a "mirror MOT." The atoms are subsequently trapped in a magnetic trap and transferred into the microtrap.

Microtraps provide excellent conditions for evaporative cooling. The atomic cloud can be compressed by increasing the magnetic field gradients of the microtrap [cf. Eq. (8)]. During adiabatic compression, the temperature increases without loss of phase-space density ($n\lambda^3 = \mathrm{const}$). Simultaneously, the elastic collision rate $\gamma = \sigma n v$ increases in a harmonic trap proportionally to the square of the temperature ($\gamma \propto T^2$). This results in a fast thermalization of the cloud, and cooling is possible on a short time scale. Here n is the density, λ is the thermal wavelength, v is the mean relative velocity, and σ is the scattering cross section. The gain resulting from adiabatic compression is ultimately limited by density-dependent two- and three-body loss mechanisms (Boesten *et al.*, 1996; Fedichev *et al.*, 1996; Moerdijk *et al.*, 1996; Burt *et al.*, 1997; Esry *et al.*, 1999; Söding *et al.*, 1999; Weiner *et al.*, 1999). In practice, the trap is often relaxed to moderate confinement after the condensate is generated in order to reduce the density and increase the condensate lifetime (Hänsel *et al.*, 2001; Ott, Fortágh, Kraft, *et al.*, 2003a). Besides the well-established technique of radio-frequency evaporation, surface evaporation has also been successfully demonstrated (Reichel *et al.*, 1999). Thereby, energetic atoms are removed from the cloud by collision with the nearby chip surface. Harber *et al.* (2003) succeeded to cool a cloud of rubidium by this means below the critical temperature of Bose-Einstein condensation. Evaporative cooling of fermionic atoms also requires the preparation of spin mixtures. Alternatively, the fermionic gas may be cooled by thermal coupling to a bosonic gas, as reported in recent experiments.

In the following we review three different approaches for loading atoms into microtraps and related experiments on producing quantum-degenerate gases.

1. Loading by magnetic transfer

Adiabatic magnetic transfer is a method for loading ultracold clouds of atoms at constant phase space density ($n\lambda^3 = \mathrm{const}$) into the microtrap. Thereby, a large volume magnetic trap, to begin with loaded with atoms from a MOT, is transformed continuously into a tightly confining potential of the microtrap (Fortágh, Grossmann, Zimmermann, and Hänsch, 1998; Vuletic *et al.*, 1998). Subsequent efficient evaporative or sympathetic cooling allows for the preparation of large samples of degenerate quantum gases. This loading method sets almost no constraints on the chip surface which carries the current conductors. Even stacked combinations of chips and three-dimensional structures can be loaded.

An adiabatic transfer scheme allowing 100% transfer efficiency has been introduced by Ott *et al.* (2001) and Fortágh *et al.* (2003). The experimental setup is shown in Fig. 31. The standard six-beam magneto-optical trap is operated between the MOT coils. It is spatially separated from the microtrap, which is mounted between the

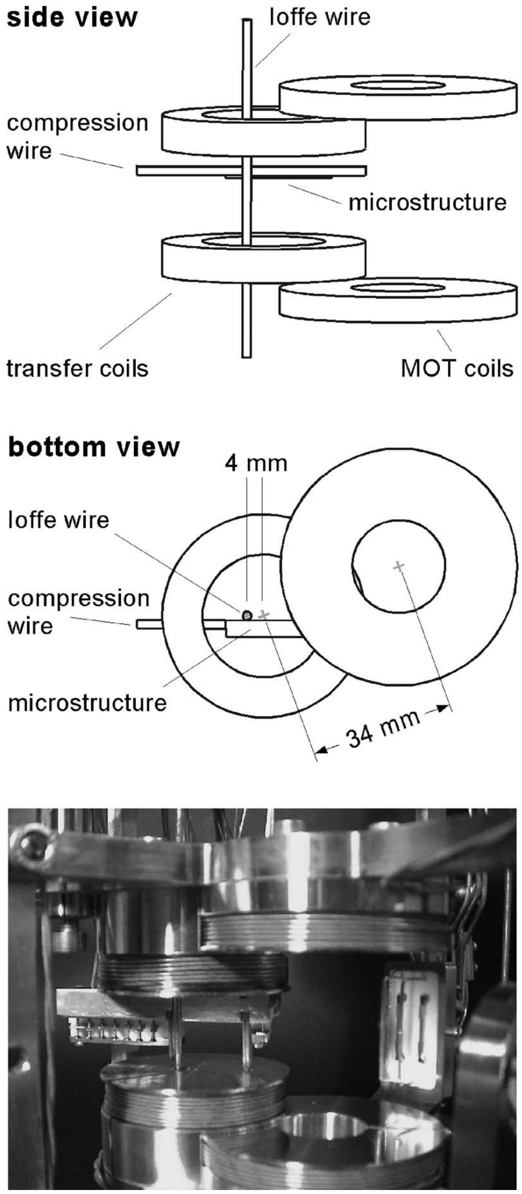

FIG. 31. Trap setup for an optimized adiabatic transfer of atoms into the microtrap (to scale). The compression wire and microstructure are rigidly connected to a heat sink between the transfer coils. The photograph shows the trap setup and dispenser source behind the MOT coils. The complete setup is mounted to a vacuum flange and operated in a vacuum chamber at a pressure of 10^{-11} mbar. From Fortágh *et al.*, 2003.

transfer coils. This separation guarantees an undisturbed operation of the MOT and allows for high flexibility in mounting different microtraps which can be loaded by the same adiabatic transfer scheme. Chips with microfabricated conductors are mounted upside down below the compression wire with the microtrap formed below the microstructure. As described in Sec. II.D.3, an Ioffe trap is generated by combining the magnetic fields of the transfer coils and the Ioffe wire. The trap position can be shifted vertically by varying the current ratio in the transfer coils. The compression wire and at least one of the microfabricated conductors of the chip are aligned parallel to the symmetry axis of the Ioffe trap.

The atoms are precooled in the MOT and then magnetically stored in the field of the MOT coils. Next, the trap center is shifted to the transfer coils by increasing the current in these and simultaneously decreasing the current in the MOT coils. Due to the geometrical overlap of MOT and transfer coils, the center of the quadrupole trap moves on a straight line from one pair of coils to the other. The quadrupole trap is then (or simultaneously with the previous step) transformed into a large-volume Ioffe trap by raising the current in the Ioffe wire above the critical value [Eq. (31)]. The transfer to the microtrap is accomplished by lowering the current in the upper coil. This shifts the trap center towards a microwire on the chip, which takes over the role of the upper coil. The transfer is completed by activating the compression wire. It generates a bias field for the microwire such that the microwire and the compression wire together establish a strong radial confinement. The axial confinement is still due to the Ioffe trap, i.e., the lower transfer coil and the Ioffe wire. They both can be turned off after the axial confinement has been taken over by suitable microwires on the chip. Similarly, the compression wire can be replaced by on-chip conductors for generating the bias field (Günther, Kemmler, Kraft, *et al.*, 2005).

The MOT is loaded within 25 s from pulsed dispenser sources (Fortágh, Grossmann, Hänsch, and Zimmermann, 1998; Fortágh *et al.*, 2003) with 3×10^{8} ^{87}Rb at a temperature of 50 μK. After 10 ms of polarization gradient cooling and optical pumping into the $|F=2,m_F=2\rangle$ ground-state magnetic sublevel a cloud of 2×10^{8} atoms at a temperature of 60 μK is stored in the spherical quadrupole trap formed by the MOT coils (axial gradient of 45 G/cm). The adiabatic transfer to the transfer coils (axial gradient of 58 G/cm) takes place within 1 s. During the transfer the current in the Ioffe wire is increased to a maximum value of 13 A, such that the cloud is loaded into a harmonic trapping potential with $(\omega_a,\omega_a)=2\pi\times(14{,}110)$ s^{-1}and $B_{\mathrm{off}}=0.4$ G. Here the cloud is cooled for 20 s by radio-frequency evaporation to a temperature of 5 μK (frequency ramp from 10 to 2 MHz). Subsequently, the thermal cloud of 2×10^{7} atoms is adiabatically transferred into the microtrap by reducing the current in the upper transfer coil. The compression into the microtrap lasts 1 s and is completed by activating the compression wire (Fig. 32). The compression heats the cloud by a factor of 7, leading to strongly enhanced elastic scattering with a rate of several hundred collisions per second. After a second stage of forced evaporation for 5 s, condensation is achieved with up to 1×10^{6} atoms at a critical temperature between 500 nK and 1 μK, depending on the radial confinement which can range from $\omega_r=2\pi\times200$ to $2\pi\times2000$ s^{-1}.

The method of adiabatic transfer has also been used in experiments by Lin *et al.* (2004) to load atoms into a microtrap. The cloud is initially stored in the large-volume spherical quadrupole trap between the MOT

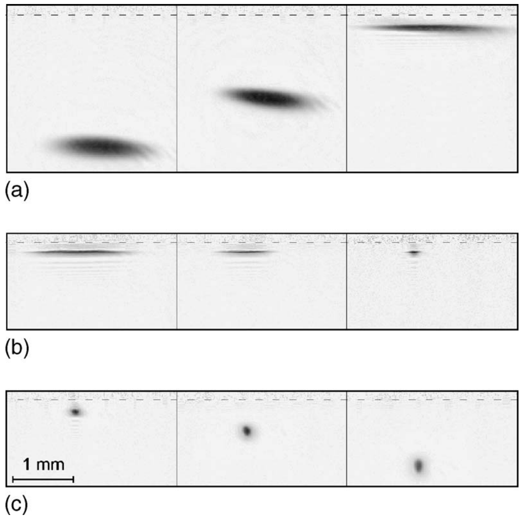

FIG. 32. Absorption images of the adiabatic magnetic transfer into the microtrap and cooling towards Bose-Einstein condensation. The dashed line indicates the surface of the microstructure. (a) Transfer and compression of the Ioffe trap into the microtrap. (b) rf cooling in the microtrap. The image on the right side shows the condensate in the trap. (c) Release of the condensate. Images taken after 5, 10, and 15 ms time of flight (left to right). From Ott *et al.*, 2001.

coils and is compressed toward a microstructure using the magnetic field of a small coil behind the chip. At the same time, the quadrupole is converted into an Ioffe trap similar to the procedure described above.

Another magnetic transfer scheme has been reported by Schwindt *et al.* (2005). It is based on the mechanical translation of magnetic field coils, carrying ultracold atoms form the optical trapping region to the microtrap.

A mixture of quantum degenerate ^{87}Rb and ^{6}Li gas has been produced by means of sympathetic cooling in an Ioffe trap similar to the one described above (Silber *et al.*, 2005). Atoms of bosonic ^{87}Rb and fermionic ^{6}Li are prepared simultaneously in a six-beam MOT. A subsequent spin-polarizing pulse pumps rubidium into the $|F=2,m_F=2\rangle$ and lithium into the $|F=3/2,m_F=3/2\rangle$ hyperfine state. The cloud is then loaded into the magnetic-quadrupole trap of the MOT coils and adiabatically transferred into the Ioffe trap. Evaporative cooling of rubidium is initiated by applying a microwave ramp coupling the hyperfine states $|F=2,m_F=2\rangle \rightarrow |F=1,m_F=1\rangle$ of rubidium but not interacting with lithium atoms. Standard rf evaporation is not suitable for efficient cooling of this mixture because it removes rubidium and lithium atoms at the same time. Bose-Einstein condensation is reached within 15 s with about 1.2×10^{6} ^{87}Rb atoms in a trap with oscillation frequencies of $(\omega_a,\omega_r)=2\pi\times(50.1,206)\ \mathrm{s}^{-1}$. The lithium cloud contains initially 2×10^{7} atoms and is cooled by thermalizing collisions with the rubidium gas. For cooling ramps longer than 25 s, Fermi degeneracy is reached with 2×10^{5} ^{6}Li atoms at a temperature of $T_F\simeq2.4\ \mu$K. This temperature is well above the critical temperature for Bose-Einstein condensation. By monitoring the thermalization time between the two species the interspecies s-wave scattering length has been determined to be $|a|=20^{+9}_{-6}a_B$. Fermi degeneracy was detected by observing the saturation of the release energy for small temperatures.

The preparation of a mixture of Bose-condensed ^{87}Rb atoms and Fermi degenerate ^{40}K atoms in a chip trap has been reported by Aubin *et al.* (2006). Initially, 2×10^{7} ^{40}K and 10^{9} ^{87}Rb atoms are prepared in a MOT. The atoms are transferred into a purely magnetic trap. Subsequently, the atoms are transported into a Z trap located at 200 μm distance to the chip surface. The trap is characterized by the potassium oscillation frequencies $(\omega_a,\omega_r)=2\pi\times(42.6\pm0.7,823\pm7)\ \mathrm{s}^{-1}$. The cloud loaded into the microtrap consists of 2×10^{5} ^{40}K and 2×10^{7} ^{87}Rb double-spin-polarized atoms at a temperature of $\sim$300 μK. Forced evaporation of rubidium is initiated by applying a radio-frequency ramp from 30 to 3.61 MHz. The rf selectively removes the fastest rubidium atoms whereas the potassium atoms, with smaller Zeeman splittings, are not ejected but cooled by thermalizing with the rubidium cloud. Due to the tight confinement, the sympathetic cooling is extremely efficient. Fermi degeneracy is reached within just 6 s. It has been observed that Fermi degeneracy is not reached for faster cooling ramps although the rubidium gas can be cooled down to condensation within 2 s. This indicates that the ^{40}K-^{87}Rb mixture rethermalizes more slowly than the ^{87}Rb gas itself. Fermi degeneracy is detected by observing saturation of the release energy for small temperatures and also by fitting the Fermi distribution function to the shape of the cloud (Fig. 33). A temperature as low as $k_BT/E_F=0.09\pm0.05$ is reached with 4×10^{4} ^{40}K atoms.

2. Loading from a mirror MOT

The mirror MOT is a variant of the standard magneto-optical trap. It collects atoms close to a reflecting surface (Reichel *et al.*, 1999). The mirror MOT is generated by two counterpropagating pairs of laser beams, with one pair reflected at the chip surface (Fig. 34). The MOT center is defined by a spherical magnetic quadrupole field and the overlap region of the four laser beams. The reflected beams are aligned at an angle of 45° with the mirror such that one of the beams is aligned parallel to the quadrupole axis. The loading of the microtrap starts with a MOT phase for collecting atoms, followed by a compressed MOT phase in which the cloud is moved toward the chip surface where a magnetic quadrupole field is generated by a U-shaped wire on the chip plus a bias field (U-MOT). This matches the atomic density distribution to the geometry of the microtrap. After subsequent standard polarization gradient cooling and optical pumping, the light is turned off such that the cloud is stored in the magnetic field of the microtrap alone. Optimized loading was reported by using a large-scale U-shaped wire below the chip, for operating the U-MOT as well as for initial magnetic trapping

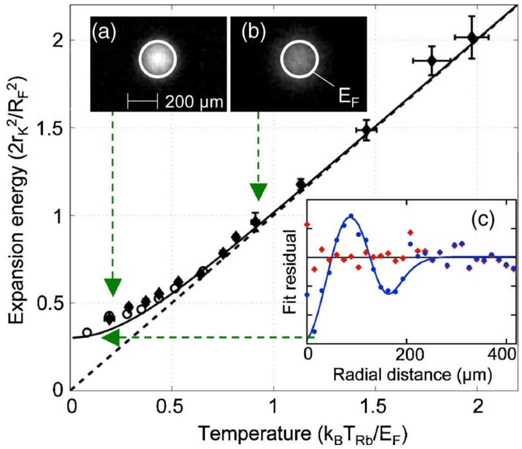

FIG. 33. (Color online) Observation of Fermi statistics. The quantity r_K^2 is proportional to expansion energy and is plotted versus the temperature of the ^{87}Rb reservoir. The vertical axis is scaled using $R_F^2 = E_F(\omega_r^{-2} + \tau^2)/m_K$, where τ is the expansion time before imaging. The temperature is also scaled by the Fermi energy E_F (typically $k_B \times 1.1$ μK) of each ^{40}K cloud. Gaussian fits of data taken with both thermal (diamonds) and Bose-condensed (circles) ^{87}Rb are compared to Gaussian fits of an ideal Fermi distribution (solid line) and a Boltzmann distribution valid for classical particles (dashed line). Absorption images are shown for (a) $k_BT/E_F = 0.35$ and (b) 0.95, including a white circle indicating the Fermi energy E_F. (c) The fit residuals of a radially averaged cloud profile show a strong systematic deviation when assuming Boltzmann (circles) instead of Fermi (diamonds) statistics. A degenerate Fermi cloud is flatter at its center than a Boltzmann distribution and drops off more sharply near its edge. Adapted from Aubin *et al.*, 2006.

(Folman *et al.*, 2000). This combines advantages of the mirror MOT with subsequent magnetic transfer to the microtrap. Experimentally, this elegant method of the mirror MOT is more compact and requires less auxiliary magnetic field design. Since the surface of the chip must act as a mirror for the cooling laser, the method is not always applicable.

In the first realization by Reichel *et al.* (1999), the mirror MOT was loaded 2.2 mm below the chip surface, collecting 5×10^6 ^{87}Rb atoms within 4 s from a rubidium vapor. Subsequently, the MOT center was moved toward the chip surface by shifting the center of the magnetic quadrupole field (Fig. 34). At a distance of 1.1 mm from the surface, the magnetic field of the coils was replaced by the quadrupole field produced by a U-shaped wire on the chip and an external bias field. Further reduction of the cloud-surface distance to 0.3 mm was achieved by reducing the current in the U wire and simultaneously increasing the laser detuning. By suddenly blocking the laser, 2×10^6 atoms were stored in the magnetic microtrap. The loading was optimized in a later experiment by applying standard techniques of polarization gradient cooling and optical pumping prior to magnetic storage (Reichel *et al.*, 2001). Losses from the MOT were observed for distances to the mirror surface which were smaller than 2 mm (Reichel, 2002).

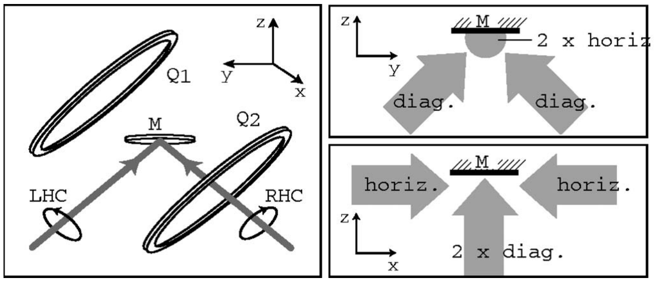

FIG. 34. The mirror MOT. Left: perspective view indicating circular polarization of the diagonal beams incident on the mirror M and the orientation of the quadrupole coils $Q1$ and $Q2$. The horizontal beams (perpendicular to the drawing plane) are not shown. Right: Projections on the y-z and x-z planes, illustrating the geometry of the laser beams. From Reichel *et al.*, 2001.

These experiments were carried out in a glass cell with the inner dimensions $30 \times 30 \times 110$ mm^3. At the moderate vacuum of $\sim 10^{-9}$ mbar the pressure-limited trap lifetime was 5 s. The mirror MOT was operated with laser beams of 8.5 mm $1/e^2$ diameter and a total laser power of 20 mW distributed among the four beams. The rubidium background vapor was produced by a resistively heated dispenser. For generating Bose-Einstein condensates (Hänsel *et al.*, 2001), the loading of the mirror MOT was further enhanced by light-induced desorption of rubidium (Anderson and Kasevich, 2001; Atutov *et al.*, 2003): During the MOT phase, illumination of the glass cell with a halogen light bulb temporarily increased the rubidium pressure and thus the number of atoms in the mirror MOT. A cloud of 3×10^6 ^{87}Rb atoms in the $|F=2, m_F=2\rangle$ state, at a temperature of 45 μK and a peak density of 5×10^{10} cm^{-3}, was subsequently loaded into a purely magnetic potential of a Z trap $[(\omega_a, \omega_r) = 2\pi \times (28, 220)$ s$^{-1}]$. In order to increase the elastic collision rate, the trap was compressed to $(\omega_a, \omega_r) = 2\pi \times (17, 6200)$ s^{-1} within 300 ms. Subsequent cooling for 900 ms by forced evaporation using a linear radio-frequency ramp from 30 to 8 MHz reduced the number of atoms to 5×10^5. An additional exponential rf ramp cooled the cloud further to a temperature of 6 μK within 800 ms. In order to avoid three-body recombination losses the trap was then relaxed to $(\omega_a, \omega_r) = 2\pi \times (20, 3900)$ s^{-1}. With a final 300 ms long rf sweep, condensation was reached with 1.1×10^4 atoms at a critical temperature of 670 nK. Faster condensation was observed by compressing the thermal cloud after the first 900 ms of cooling into an even tighter trap with $(\omega_x, \omega_y, \omega_z) = 2\pi \times (300, 3400, 3500)$ s^{-1}. A subsequent rf ramp of 500 ms duration cooled the gas below the critical temperature. Hänsel *et al.* (2001) reported further reduction of the entire evaporation time for Bose-Einstein condensation to below 700 ms.

The technique of mirror MOT has been used by a large number of research groups. Related publications are given by Reichel *et al.* (1999, 2001), Cassettari, Chenet, *et al.* (2000), Cassettari, Hessmo, *et al.* (2000), Hänsel *et al.* (2001), Hänsel, Reichel, *et al.* (2001a), Jones, Vale, Sahagun, Hall, and Hinds (2003), Kasper *et al.* (2003), Krüger *et al.* (2003), Schneider *et al.* (2003), Vale, Sahagun, Hall, Eberlein, *et al.* (2003), Holmes *et al.* (2004), and Vale *et al.* (2004).

Folman *et al.* (2002) combined a mirror MOT with a macroscopic U-shaped wire underneath the reflecting chip surface. The wire was driven with currents up to 20 A. After loading a cloud of 10^8 lithium atoms into the MOT at a few millimeters distance to the chip surface, the spherical quadrupole field of the external coils was replaced by the field of the macroscopic U wire to generate the magnetic field for the MOT (U-MOT). Subsequently, the U wire was used to magnetically trap the cloud at a distance of 2 mm to the surface. The current in the macroscopic wire was then reduced and the cloud was loaded into the field of microscopic conductors at the chip surface.

In the experiment of Jones, Vale, Sahagun, Hall, and Hinds (2003), the mirror MOT is loaded at a distance of 4 mm from the surface, which allows for a large trapping volume. A number of 10^8 ^{87}Rb atoms from a thermal dispenser source are loaded at a temperature of 50 μK. The MOT is thereafter shifted to a distance of 1.3 mm from the surface and 2×10^7 atoms are loaded into the magnetic trap. After forced evaporation, BEC is reached with 5×10^4 atoms.

In the experiment of Schneider *et al.* (2003), the mirror MOT is loaded by means of a double-MOT system. At a distance of 3 mm from the reflecting surface, 10^9 atoms are loaded within 20 s. By changing to a U-MOT within 300 ms, the cloud shifts to 2 mm distance from the surface. After optical molasses and optical pumping, 10^8 atoms are stored in the magnetic field of a macroscopic Z trap and condensation is reached with 3×10^5 atoms.

The operation of mirror MOT's is obviously restricted to reflecting chip surfaces. This can be realized by deposition of reflecting coatings onto microstructures (Reichel *et al.*, 2001; Lev, 2003) or by using reflecting metallic chip surfaces where the conductors are defined by narrow grooves in the metal. Mirror MOT's have been successfully operated with narrow grooves in the reflecting surface (Folman *et al.*, 2000; Cassettari, Hessmo, *et al.*, 2000; Jones, Vale, Sahagun, Hall, and Hinds, 2003; Vale *et al.*, 2004). In the experiment of Vale *et al.* (2004), the grooves are as large as 150 μm. This mirror MOT still collects up to 10^8 ^{87}Rb atoms at 4.5 mm distance from the surface and condensation is reached with 4×10^4 atoms in the microtrap.

3. Optical tweezers

A third method for loading microtraps makes use of optical tweezers (Gustavson *et al.*, 2002). The optical-dipole potential of a red-detuned and focused laser beam is loaded with a Bose-Einstein condensate from a conventional magnetic trap. The potential of the optical tweezers beam is subsequently moved to the microtrap and the condensate is transferred by replacing the optical potential by the magnetic potential of the microtrap.

The experimental system consists of two differentially pumped vacuum chambers. Bose-Einstein condensates of sodium with up to 2×10^6 atoms are produced in a cloverleaf magnetic trap in the production chamber. Condensates are transferred into the optical dipole potential of an infrared laser beam (1064 nm). The beam profile is filtered by a single-mode fiber, and light intensity is controlled by an acousto-optic modulator. The transfer into the optical tweezers potential is achieved by linearly increasing the 1064 nm laser power to 180 mW in 600 ms and suddenly switching off the magnetic trap. The collimated laser beam is focused by an achromatic lens of 500 mm focal length. The focus is imaged with relay optics onto the condensate. The resulting optical tweezers beam has a $1/e^2$ beam waist radius of 24 μm. It is transversally aligned to the condensate within 20 μm. With a trap depth of 11 μK, the transfer efficiency from the magnetic trap into the optical tweezers is close to 100%. The condensate is transported by translating the potential of the optical tweezers into the science chamber. The linear translation of the tweezers potential over a distance of 36 cm is realized by shifting the 500 mm lens on a mechanical translation stage. With trapezoidal acceleration and deceleration ramp, the best transport was reached for a maximum acceleration of 37 m/s^2 and a maximum velocity of 70 m/s, yielding total translation time of 7.5 s. Within the first second of translation, the laser power is reduced to 90 mW, resulting in axial and radial trap frequencies of 4 and 440 Hz, respectively. Condensates of up to 6×10^5 atoms were transported into the science chamber. The loss of atoms during transport was dominated by three-body recombination which might be reduced by using large-volume elliptical dipole traps. At its final position, the condensate is located 1 mm below a Z-shaped wire trap (1.27 mm diameter, 5 mm central length). It is loaded by linearly increasing the wire current from 0 to 2 A and simultaneously increasing a bias field to 2.9 G within 1 s. The optical trap is then turned off slowly. A transfer efficiency of nearly 100% was realized (Fig. 35). After the first demonstration, the optical tweezers method has been further optimized and condensates with up to 10^7 atoms have been transported to various microtraps located in the science chamber (Leanhardt, Chikkatur, *et al.*, 2002; Leanhardt, Gorlitz, *et al.*, 2002; Leanhardt, Pasquini, *et al.*, 2003; Leanhardt, Shin, *et al.*, 2003; Shin, Saba, Vengalatorre, *et al.*, 2004).

The method of optical tweezers allows for a flexible transfer of atoms or atomic clouds into magnetic micropotentials. The main advantages result from the trapping mechanism based on the dipole interaction that is decoupled from the magnetic microtrap. Optical tweezers offer also a large flexibility in positioning the cloud at the chip surface.

B. Condensate propagation in waveguides

1. Ballistic propagation and small perturbations

The simplest possible dynamics of a condensate in a microtrap is ballistic propagation along a waveguide. It

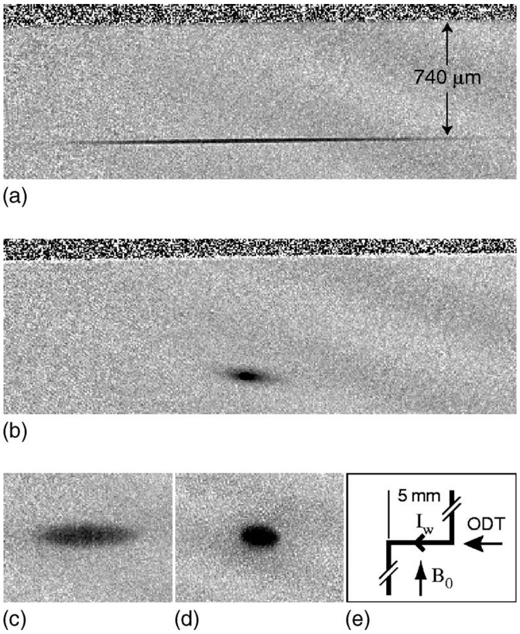

FIG. 35. Absorption images of condensates in the science chamber, side view. All images have the same scale. Condensates of $\sim 6\times 10^5$ atoms are shown in (a) optical trap and (b) wire trap. The center segment of the Z-shaped wire is visible as a dark speckled horizontal stripe and is located 740 μm above the trapped atoms. The condensate was released from (c) an optical trap after 10 ms time of flight and (d) wire trap after 23 ms time of flight. (e) Schematic of the wire trap, top view. $I_w=2$ A is the current through the wire, and $B_0=2.9$ G is the bias field. Atoms are trapped below the 5 mm long central segment of the wire, which is aligned with the optical trap axis. The supporting end segments, which provide field curvature, are truncated. From Gustavson *et al.*, 2002.

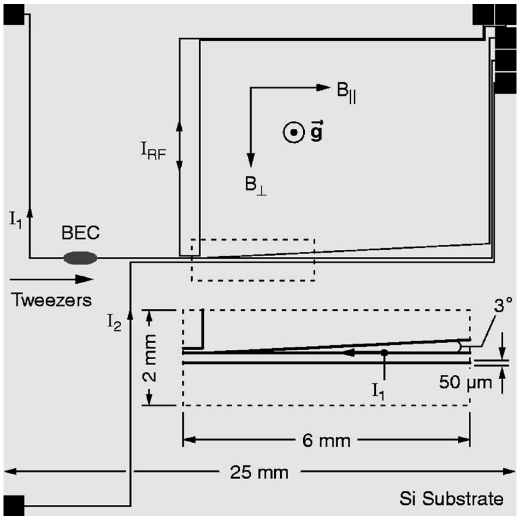

FIG. 36. Microfabricated magnetic trap and waveguide. Optical tweezers loaded a Bose-Einstein condensate into the Z-wire trap formed by currents I_1 and I_2 in conjunction with a magnetic bias field $B_{\perp}$. Lowering I_2 to zero released the condensate into a single-wire magnetic waveguide. Atom flow was from left to right. Inset: The widening of the waveguide wire in the region where another wire merges with it at a small angle. The only current flowing in the inset is I_1. The condensate was trapped above the plane of the page, and the gravitational acceleration $\vec{g}$ points out of the page. All microfabricated features are drawn to scale. From Leanhardt, Chikkatur, *et al.*, 2002.

has been studied in shallow waveguides with moderate confinement, similar to conventional traps. Surprisingly, even small deviations from purely harmonic potentials may induce significant excitations of the condensate. In two experiments such excitations have been investigated.

The influence of a local perturbation of the waveguide potential has been studied at the MIT by Leanhardt, Chikkatur, *et al.* (2002). The chip consists of 50 μm wide and 10 μm thick conductors electroplated on a silicon substrate (Fig. 36). With the two currents I_1 and I_2 turned on, a Z trap forms on the left side of the chip. A condensate with about 10^6 Na atoms in the $F=1$, $m_F=-1$ Zeeman substrate is transferred into the trap with a spatially variable optical potential (optical tweezers). After turning off I_2, the atoms are accelerated into a waveguide ($\omega_{\perp}\cong 2\pi\times 90$ Hz) where they travel with an adjustable speed between 30 and 66 mm/s. Although the corresponding translational energy largely exceeds the energy of the lowest radial excitation mode, the condensate propagates without radial excitations and in that sense is single mode. The waveguide is separated from the surface by 450 μm so that geometric imperfections of the current conductor are too small to couple the center-of-mass motion to collective excitations of the condensate. Thus, unperturbed propagation over a distance of several tens of millimeters with a high speed is possible in this regime. Next, a perturbation is introduced. It is realized by a widening of the conductor, which is caused as side effect of a Y-junction geometry (inset in Fig. 36). When the junction is not activated, i.e., with only I_1 flowing, the centroid of the current density is nevertheless deviated at the beginning and at the end of the perturbation where the second conductor geometrically merges with the main current conductor. In the deviated regions the current component parallel (antiparallel) to the bias field produces a magnetic field component parallel (antiparallel) to the offset field. The offset field is thus corrugated and atoms entering (exiting) the perturbed guiding region encounter a magnetic potential well (barrier). In the experiment the barrier height (well depth) amounts to $h\times 50$ kHz, which is comparable to the kinetic energy of the condensate. At this potential the condensate is completely reflected for velocities below 45 mm/s while for velocities above 54 mm/s full transmission is observed. The transmitted condensate features strong transverse excitations induced by the geometric perturbation at the Y junction. The excitation energy depends on the tilt angle and on the velocity of the condensate. In the experiment it reaches values of about $h\times 1$ kHz for a tilt angle of 13 mrad and a velocity of 66 mm/s. Since the excitation amplitude varies with the axial position within the condensate, it should be expected that the perturbation destroys the initially homogeneous phase of the condensate within a millisecond. This experiment shows that it is important to understand the role of collective excitations for the development of coherent atom optics with condensates in microtraps.

2. Oscillation in an anharmonic potential

A systematic study of collective excitations for the propagation of a condensate in a waveguide has been carried out at the University of Tübingen (Ott, Fortágh, Kraft, *et al.*, 2003). The condensate is placed in a waveguide far from the surface with a moderate harmonic radial potential ($\omega_r = 2\pi \times 110\ \mathrm{s}^{-1}$). The waveguide is terminated by a shallow and almost harmonic axial potential with $\omega_z = 2\pi \times 8\ \mathrm{s}^{-1}$. Additional conductors introduce a small distortion to the harmonic potential. The total axial potential is now described by a Taylor expansion including terms up to the fifth power in position. In the experiment, an axial oscillation of the condensate is started with fixed amplitudes between 0.45 mm and 0.79 mm (Fig. 37).

Within this range the correction to a strictly harmonic shape of the axial potential stays below 16%. Nevertheless, this perturbation is sufficiently strong to excite shape oscillations of the condensate with variations of the condensate aspect ratio by more than a factor of 10. Collective excitations with such unusually large amplitudes are highly nonlinear such that sum and difference frequency mixing between the collective modes are observed. The excitation mechanism can be described in the rest frame of the center-of-mass oscillation of the condensate (Ott, Fortágh, and Zimmermann, 2003). In this frame the axial trapping potential is approximately harmonic (for a short condensate), however, with a local radial trap frequency that varies by about a factor of 3 with the period of the axial center-of-mass motion. This periodic change of the local trap curvature squeezes the condensate and induces shape oscillations. This picture allows to apply the well-known scaling version of the Gross-Pitaevskii equation in the Thomas-Fermi limit (Kagan *et al.*, 1997), and numerical simulation is straightforward.

Figure 38 shows the temporal change of the aspect ratio for three different amplitudes of the center-of-mass motion. A Fourier transformation of the data reveals three distinct oscillations which can be attributed to the fundamental frequency of the center-of-mass motion, its second harmonic, and to the frequency of the lowest collective excitation eigenmode. At larger amplitudes mixing between these frequencies occurs, leading to an increasingly complex spectrum. By extending the simulation for the large-amplitude case to long-time intervals (which are experimentally inaccessible) one finds that the motion is chaotic in a sense of an exponential sensitivity to initial conditions.

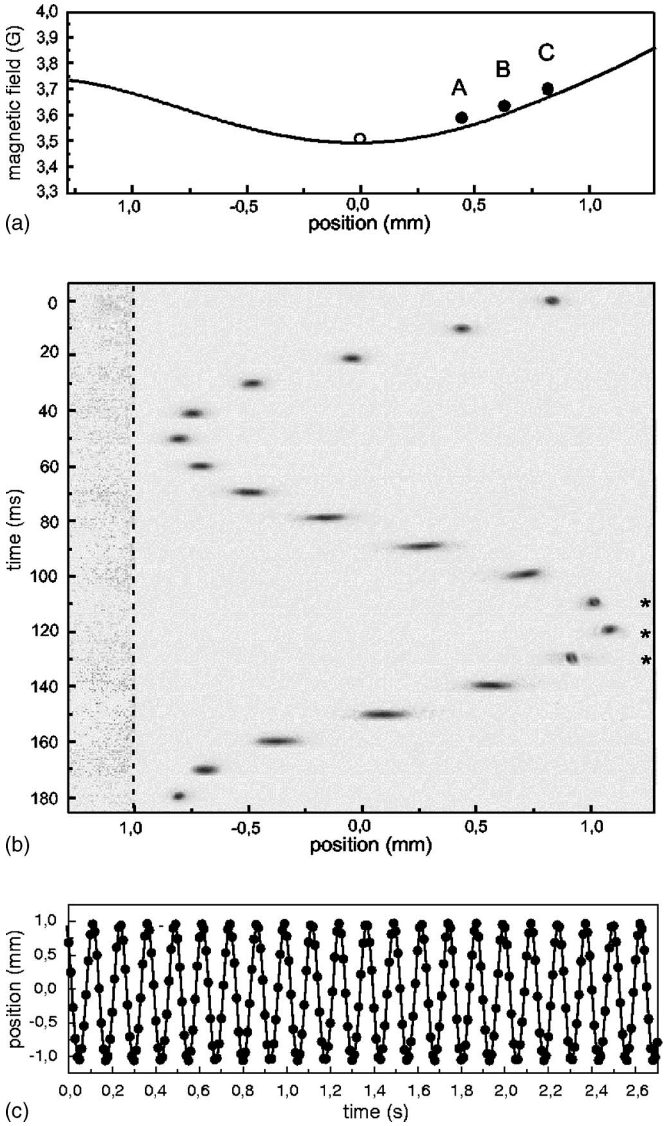

FIG. 37. Oscillation of the condensate in an anharmonic waveguide. The condensate is trapped below the microstructure that generates the magnetic field for the trapping potential. (a) Magnetic field in the trap minimum along the axial direction. The black dots indicate the starting positions *A*, *B*, and *C* of the oscillation for three different experimental series. The circle marks the initial position without displacement. (b) Absorption images of the condensate after 20 ms time of flight (series *C*, 10 ms intervals). In the time-of-flight image, the amplitude of the oscillation is enhanced with respect to oscillation in the trap (also a phase shift occurs). For condensates marked with an asterisk the size of the condensate cannot be properly determined due to the limited resolution of the absorption imaging. (c) Center-of-mass motion of the condensate (series *B*): experimental data (dots) and fit with three sinusoidal functions (line). From Ott, Fortágh, Kraft, *et al.*, 2003.

The ballistic experiments show that even small deviations from strictly harmonic potentials strongly couple the center-of-mass motion and the internal degrees of freedom of the condensate (collective excitations). Although possible in principle, full quantum control of a condensate during a ballistic propagation may thus be difficult to achieve experimentally. The problem may be circumvented for low-density condensates in the quasi-one-dimensional regime (Görlitz *et al.*, 2001). Here the atomic interaction energy is below the transverse energy

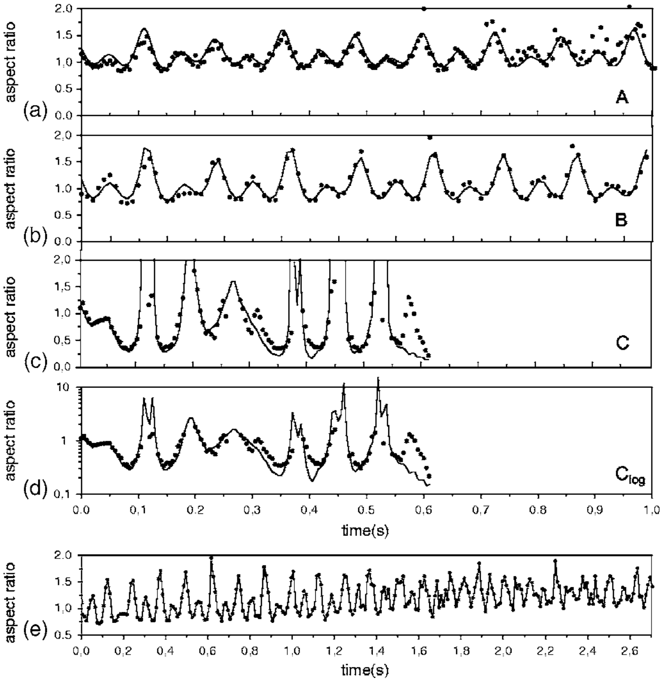

FIG. 38. Evolution of the aspect ratio of the condensate for the data series (a) A, (b) B, and (c) C (dots) and theoretical model (solid line). (d) Plot (c) with a logarithmic scale. (e) All data points of series B. From Ott, Fortágh, Kraft, *et al.*, 2003.

spacing of the trap $(ng < \hbar\omega_\perp)$ and the condensate is confined to the transversal trap ground state. In microtrap experiments this regime has been reached by releasing the condensate into a waveguide (Fortágh *et al.*, 2003). During axial expansion in the waveguide the interaction energy is transformed into kinetic energy and the transverse radius of the condensate decreases until the interaction energy falls below the energy spacing of the transverse confinement. This situation is reached typically within a few tens of milliseconds of expansion. The quasi-one-dimensional regime was achieved also in other experiments (Wildermuth, Hafferberth, Lesanovsky, Haller, *et al.*, 2005). Nevertheless, few experimental data have been published to date on the dynamics in regard to the sensitivity to potential perturbations.

C. On-chip matter-wave interferometry

Integrated matter-wave interferometry is one of the most intriguing prospective applications of magnetic microtraps and holds great promise for building high-precision inertial force and gravity sensors and complex atom optical circuits such as quantum registers. Several schemes of phase coherent manipulation, required for these applications, can be derived from a large body of experience with thermal atoms (Adams *et al.*, 1994; Berman, 1997) and quantum-degenerate gases (Bongs and Sengstock, 2004). However, chip-based matter-wave interferometry is technically demanding and has only recently become experimentally feasible. The first experiments on phase-coherent manipulation of Bose-Einstein condensates in microtraps are summarized in the remainder of this section.

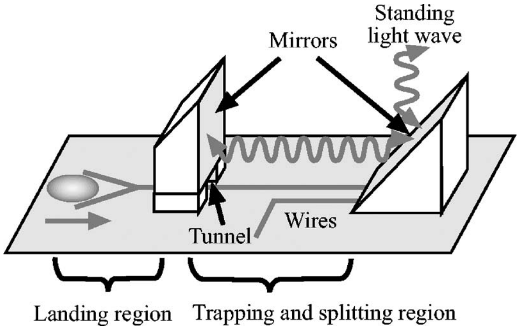

FIG. 39. Schematic drawing of the atom Michelson interferometer (not to scale). The dimensions of the chip are 5 cm $\times 2$ cm. From Wang *et al.*, 2005.

1. Atom Michelson interferometer on a chip: Magnetic waveguide with optical lattice

An atom Michelson interferometer has been demonstrated using a combination of a magnetic waveguide potential and an optical lattice potential (Wang *et al.*, 2005). Light reflected from two mirrors, attached to the chip substrate, forms an optical standing wave along the magnetic waveguide (Fig. 39). A cloud of $|F=1,m_F=-1\rangle$ ^{87}Rb atoms precooled to 0.45 μK is magnetically guided through a tunnel in the left mirror and captured in a region between the mirrors at a distance of 115 μm from the surface. By adjusting the currents of the microtrap the cloud is shifted to the location of the as-yet deactivated optical standing wave, 250 μm from the surface. Next, a condensate is generated by rf-forced evaporative cooling and kept in a harmonic trap with radial and axial trapping frequencies of $(\omega_a,\omega_r)=2\pi\times(10{,}177)$ s^{-1}.

Prior to the interferometric experiment the axial confinement is slowly ramped down within 100 ms to a frequency of $\omega_a=2\pi\times5$ s^{-1}. The interferometer is formed by a sequence of three pulsed activations of the optical potential. The optical standing-wave light field has a beam waist of 110 μm and is 7.8 GHz red detuned from the atomic resonance to minimize spontaneous emission. The first and last pulses consist of a pair of subpulses, each 20 μs of duration and separated by 63 μs. The laser power in each subpulse is 5.5 μW. This double-pulse sequence acts as an interferometric superposition of diffraction events in the Raman-Nath regime and transforms the condensate efficiently into a superposition of counterpropagating momentum states $|p=\pm2\hbar k\rangle$, with k the wave vector of the light. The two parts of the split condensate travel in opposite directions along the waveguide before a second pulse reverses their directions of propagation simultaneously. The second pulse is 150 μs in duration with a power of 6.2 μW and acts as a reflector in the Bragg regime. Upon returning to their origin, a third pulse recombines the two wave packets. The in-

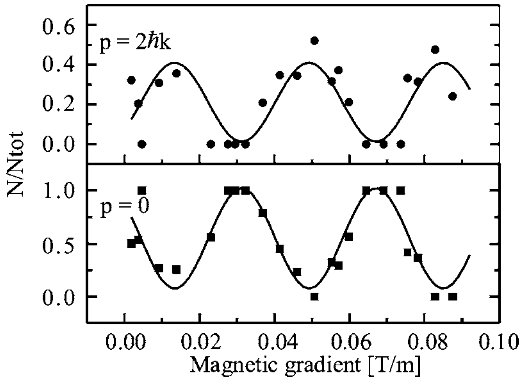

FIG. 40. Atom Michelson interferometer. Interference fringes after 1 ms propagation time in the waveguide with an axial confinement of $\omega_a = 2\pi \times 5\ \mathrm{s}^{-1}$. The differential phase shift between counterpropagating condensates is introduced by a magnetic field gradient, which is turned on for 500 μs. The average separation of clouds during the magnetic gradient pulse is 8.82 μm. From Wang *et al.*, 2005.

terferometer has two output ports. The first output port is represented by atoms having zero momentum, while the second port is represented by atoms having $|p| = 2\hbar k$. A phase shift collected during the propagation in the waveguide changes the fractional atom number in the two momentum states, which is detected by time-of-flight absorption imaging. A phase shift was experimentally accomplished by applying an axial magnetic field gradient. The uphill propagating wave acquired a larger total phase than its downhill propagating counterpart. The experimental data for 1 ms total propagation time, the time between each pulse is 0.5 ms, are shown in Fig. 40. By varying the gradient, high-contrast fringes with up to 100% visibility were detected. The maximum separation between the two packets was 12 μm, which is small compared to the full width at half maximum of the cloud of 100 μm. The contrast decreases rapidly for longer propagation times.

A similar experiment was done for condensates with a finite initial velocity along the waveguide (axial frequency of $\omega_a = 2\pi \times 5\ \mathrm{s}^{-1}$). After splitting, the two parts of the condensates climbed up the potential with different starting velocities and reached different heights. The accumulated differential phase shift thereby increases as the total propagation time increases. The best interference contrast of 20% was achieved after 10 ms propagation time, with a maximum separation of the clouds of about 120 μm. For longer propagation times the contrast rapidly decreased.

Olshanii and Dujkko (2005) calculated the fringe shift and contrast degradation in waveguide-based atom interferometers including the effect of atomic interactions. Analyzing the data of the JILA experiment they found that for the given experimental parameters and atom numbers of $N_a \sim (3-5) \times 10^3$ the fringe degradation was predominantly due to the stationary axial confinement [Fig. 41(a)]. The impact of the interactions rapidly increases with the number of atoms. As illustrated in Fig. 41(b), with 10 times more atoms the fringe degradation is dominated by the interaction. Olshanii and Dujnko identified two regimes where the fringe contrast is described by simple analytic expressions: the small interferometer regime where $v_q T \ll R$ and the large interferometer regime with $v_q T \geq R$. Here v_q is the Bragg velocity corresponding to the inverse lattice constant, T is the duration of half an interferometric cycle (time delay between the interferometric pulses), and R is the axial Thomas-Fermi radius of the condensate. In the case of a small interferometer, the destructive effect of the interactions on the fringe visibility can be compensated completely if the axial harmonic confinement is matched to the frequency of the mean field potential $\omega_{\mathrm{BEC}} = \sqrt{(4/9) g_{1\mathrm{D}} N / m R^3}$ such that $\omega_a = \sqrt{2}\omega_{\mathrm{BEC}}$. Here $g_{1\mathrm{D}}$

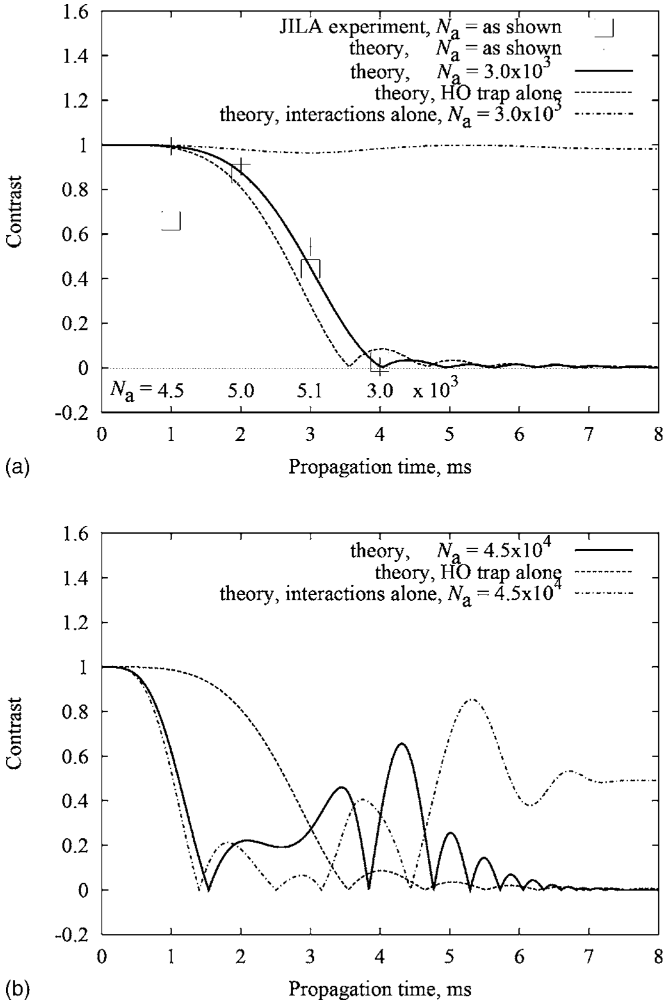

FIG. 41. Fringe visibility vs duration of the interferometric cycle corresponding to the parameters of the JILA experiment with a Michelson interferometer on a chip, using magnetic gradient as the phase element. (a) The theoretical curves correspond to $N_a = 3 \times 10^3$ atoms, according to the 4 ms point in the experiment. The theoretical predictions for the actual experimental numbers of atoms at every run are also shown. (b) The same as (a), but for $N_a = 4.5 \times 10^3$ atoms, where a reduction of the fringe contrast to 50% is expected. From Olshanii and Dunjko, 2005.

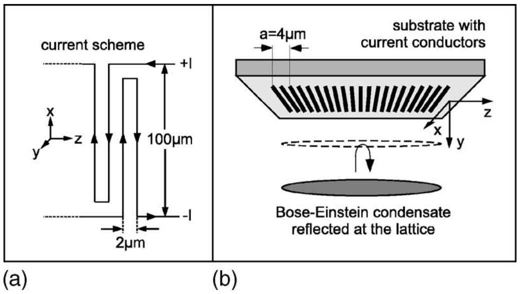

FIG. 42. Sketch of the experimental situation. (a) Current scheme of the magnetic lattice. The currents in neighboring conductors are equal and oppositely poled. (b) The condensate approaches the lattice during a vertical oscillation (y direction) in an elongated harmonic trap. After phase imprinting the condensate is released from the trapping potential. From Günther, Kraft, Kemmler, *et al.*, 2005.

is the one-dimensional coupling constant as defined by Olshanii (1998) and m is the atomic mass. In the case of large interferometers, the effect of the interactions cannot be canceled completely which sets an upper limit on the atom number involved in the interferometric process: $N \ll \hbar v_q / g_{1D}$.

2. Diffraction of a condensate from a magnetic lattice

Diffraction of a condensate from an integrated purely magnetic lattice has been reported by Günther, Kraft, Kemmler, *et al.* (2005). The lattice is produced by the magnetic field of two meandering conductors (Sec. III.B) and a magnetic waveguide potential as shown in Fig. 42. The meandering gold conductors, each 1 μm wide, 250 nm thick, and separated by 1 μm wide gaps, have been microfabricated on a 250 μm thick silicon substrate. The chip is attached to the surface of a carrier chip (Fig. 17), which is used for positioning the condensate above the meander. Operated with opposite currents, the two meandering conductors produce a periodic modulation on a magnetic waveguide potential with a lattice constant of $a=4$ μm. This potential modulation, however, decays exponentially on a length scale of $a/2\pi=630$ nm [Eq. (54)]. Thus interaction of the condensate with the magnetic lattice is only possible if the condensate is brought to a very close distance to the surface. In the experiment, this interaction is initiated by a controlled oscillation of the condensate towards the surface. The condensate is initially prepared in a shallow waveguide with oscillation frequencies of $(\omega_a, \omega_r) = 2\pi \times (16,76)$ s^{-1} at a distance of 30 μm from the chip surface. A sudden displacement of the trap center towards the lattice (up to 15 μm) excites a radial oscillation of the condensate inside the trap. The atoms interact with the lattice only for a short time (<1 ms) at the upper turning point of the oscillation. The contact with the lattice imprints an axial phase modulation onto the condensate wave function (Raman-Nath diffraction), which then consists of a superposition of discrete momentum eigenstates of the axial motion (Henkel *et al.*, 1994).

The details of phase imprinting can be summarized with a phase function $\phi(z,d)=S(d)\cos(kz+\varphi)$, which contains the potential modulation with a lattice vector $k=2\pi/a$ and a dimensionless parameter $S(d)$ that describes the amplitude of the phase modulation (Günther, Kraft, Kemmler, *et al.*, 2005; Günther *et al.*, 2006). φ characterizes a shift of the lattice position with respect to the center of the condensate. The condensate wave function directly after phase imprinting reads

$$\Psi(x,y,z) = \sqrt{n(x,y,z)}\,e^{-iS(d)\cos(kz+\varphi)}, \tag{69}$$

with $n(x,y,z)$ being the density distribution of the condensate. The relative number of atoms in the different diffraction orders is now obtained by expanding the wave function as a sum of momentum eigenfunctions of the axial motion. By exploiting the properties of the Bessel functions of first kind J_n one finds

$$\Psi(x,y,z) = \sqrt{n(x,y,z)}\sum_n e^{in(\varphi-\pi/2)} J_n(S(d))\,e^{-inkz}. \tag{70}$$

Obviously, $\Psi(x,y,z)$ consists of a discrete superposition of momentum eigenfunctions with wave vectors $k_n=nk$. The probability for an atom to be diffracted into the nth order is thus proportional to $|J_n(S(d))|^2$. As the absorption images were taken after 20 ms of ballistic expansion the measured data reveal the momentum distribution of the diffracted condensate. Up to five diffraction orders are observed with relative intensities depending on the strength of the interaction with the lattice (Fig. 43). This strength can be controlled by the amplitude of the radial oscillation. Raman-Nath diffraction is by definition a phase-coherent manipulation of a wave. The initial phase of the diffraction orders is given by Eq. (70). The intrinsic phase relation between diffraction orders together with the well-defined relative momentum of the center-of-mass motion sets promising conditions for the realization of guided matter-wave interferometers on chips. First results on this subject have been described by Günther *et al.* (2006). More detailed theoretical description of the experiments should be possible by solving the three-dimensional Gross-Pitaevskii equation. This involves extensive numerical calculations and has not yet been done.

3. Dynamical splitting of condensates with a double-well potential

Experiments on the dynamical splitting of Bose-Einstein condensates (BEC's) with a double-well potential were described by Schumm, Hofferberth, *et al.* (2005) and Shin, Sanner, *et al.* (2005). Starting with a single condensate, a growing barrier in the trap center splits the condensate into two parts. In this context it is crucial whether the splitting is associated with a predictable phase relation between the separated condensates. This may be answered by analyzing the interference pattern after recombination of the split condensates. For this purpose, the trapping potential is suddenly turned off and absorption images are taken when the condensates overlap after some time of free expansion. The

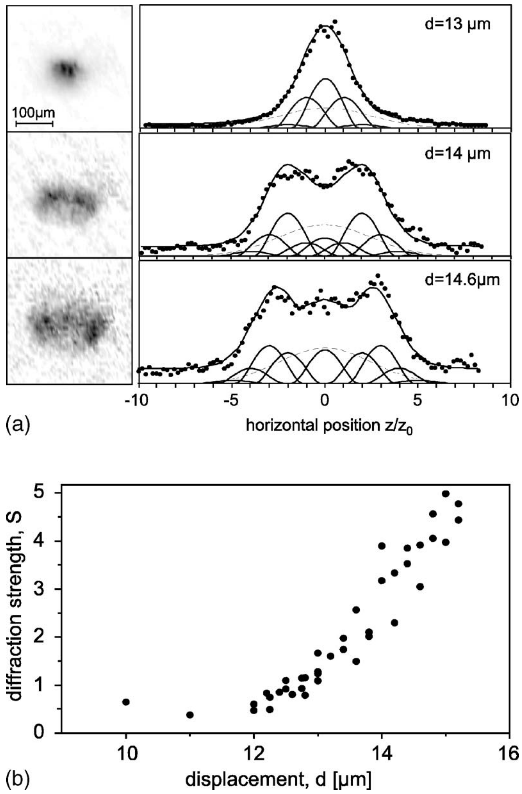

FIG. 43. Diffraction of a condensate from a magnetic lattice. (a) Absorption images and vertically integrated density profiles after $\tau=20$ ms time of ballistic expansion for three different displacements $d=13$, 14, and 14.6 μm. The distance $z_0=v_q\tau$ corresponds to one reciprocal lattice velocity v_q. The density profiles are described by the sum of up to five overlapping diffraction orders (solid line). While the relative strength of each diffraction order is given by the phase imprint parameter S, an additional Gaussian density distribution (dashed line) is used to take into account the fraction of thermal atoms. (b) The strength of phase imprinting S can be controlled, e.g., by the displacement d, initiating the oscillation towards the lattice. From Günther, Kraft, Kemmler, *et al.*, 2005.

position of the interference fringes relative to the center of the density envelope characterizes the relative phase between the condensates. If the fringes appear at the same position when the experiment is repeated, there is a deterministic phase relation between the split condensates. The spread in the position of the fringes (spread of the spatial phase) characterizes the coherence of the splitting.

The experimental setup used by Shin, Sanner, *et al.* (2005) is shown in Fig. 44. Two parallel wires separated by a distance of $d=300$ μm and both driven with a current $I_C=1.8$ A are placed in a transverse bias field B_x. This results in two magnetic waveguide potentials parallel to the chip (Sec. II.D). The waveguides merge at a critical field $B_0=\mu_0 I_C/\pi d=24$ G. The merging point is located halfway between the wires at a distance of $d/2$ from the chip surface such that interactions with the surface are avoided. The axial trapping potential ($B_y=1$ G, $f_y=13$ Hz) was carefully designed to ensure that the condensate splits perpendicular to the axial direction while keeping the two cigar-shaped parts parallel to each other. This requires two pairs of wires 1.5 mm above and 4 mm below the chip.

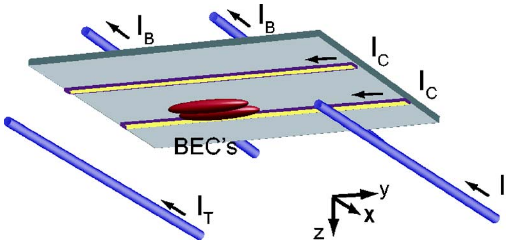

FIG. 44. (Color online) Splitting a Bose-Einstein condensate. A magnetic double-well potential is generated by two chip wires with a current I_C in combination with an external magnetic bias field. The distance between the two chip wires is 300 μm. A pair of extra wires with I_B provides the axial confinement along the y direction. A second pair with I_T is used for compensating asymmetry effects. Gravity points along the $+z$ direction. From Shin, Sanner, *et al.*, 2005.

A Bose-Einstein condensate of $|F=1, m_F=-1\rangle$ ^{23}Na atoms was loaded into the lower well of the two-wire microtrap at a 500 μm distance to the chip surface by means of optical tweezers (Sec. III.C). Subsequently, the cloud was moved up to a position 30 μm below the merging point within 1 s. Excitations were damped out within 2 s by applying a repulsive potential wall of a blue-detuned laser beam at one end of the trap and an rf shield for additional dissipation. The condensate with 8.0×10^5 atoms and a chemical potential of 1.4 ± 0.2 kHz was split by ramping $\Delta B_x=B_x-B_{x0}$ linearly from -140 to 100 ± 20 mG within 200 ms (Fig. 45). The magnetic trap was then rapidly turned off (within 20 μs), in order to prevent random perturbations. After 22 ms of free expansion the overlapping condensates generate a high-contrast interference pattern (Fig. 45), which indicates

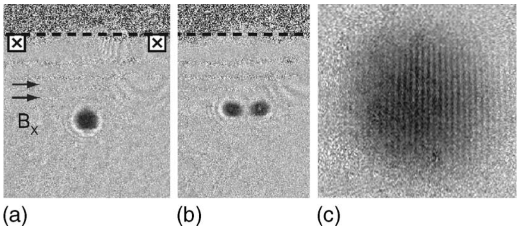

FIG. 45. Splitting of condensates. (a) Condensates were initially loaded and prepared in the bottom well of the two-wire microtrap and (b) split into two parts by increasing the external magnetic field B_x. For clarity, two condensates were split by 80 μm. The dashed line indicates the chip surface position. The currents in the chip wires flow into the page and B_x is parallel to the wire separation. Two condensates were released from the magnetic double-well potential and the matter-wave interference pattern of two condensates formed after time of flight. (c) Typical absorption image of interference fringes taken after 22 ms time of flight. The fringe spacing was 14.8 μm, corresponding to a condensate separation of 25.8 μm. From Shin, Sanner, *et al.*, 2005.

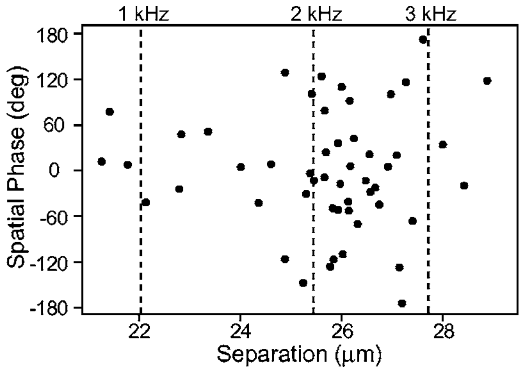

FIG. 46. Spatial phase of interference fringes. For potential barriers smaller than the chemical potential (~1.4 kHz), two condensates are phase locked and the interference pattern exhibits a predictable spatial position. Fully separated condensates produced an interference pattern with random spatial phase. The separation of two condensates d was determined from the spacing of interference fringes λ, according to the asymptotic expression $d = h\tau/m\lambda$ (Dalfovo *et al.*, 1999). Fifty repetitions of the same experiment are plotted, with the external magnetic field B_x held fixed when atoms were released. The three dashed lines indicate the separations of two wells with a barrier height of 1, 2, and 3 kHz, respectively. From Shin, Sanner, *et al.*, 2005.

that the two condensates exhibit uniform phases along their axis, perpendicular to the splitting direction.

A deterministic phase relation was observed as long as the potential barrier was smaller than the chemical potential and hence the condensates had some overlap. However, once the condensates were fully separated by the barrier the phase relation became unpredictable (Fig. 46). With faster splitting and for larger separations, even fork-shaped interference patterns appeared indicating the presence of vortices. The reason for uncontrolled excitations is the extreme sensitivity of the two-wire double-well potential to magnetic field fluctuations. Because of the vanishing harmonic confinement at the merging point, magnetic field fluctuations on the level of a few mG should be sufficient to produce significant perturbations on the double-well potential. Fast changes of the trapping potential induce mechanical perturbations of the condensate. Subsequent dissipation or coupling to collective excitation modes (Ott, Fortágh, Kraft, *et al.*, 2003; Ott, Fortágh, and Zimmermann, 2003) lead to an unpredictable relative phase of the split condensates. Extreme current stabilization and shielding of ambient magnetic field fluctuations may be necessary to achieve phase-coherent splitting with this scheme.

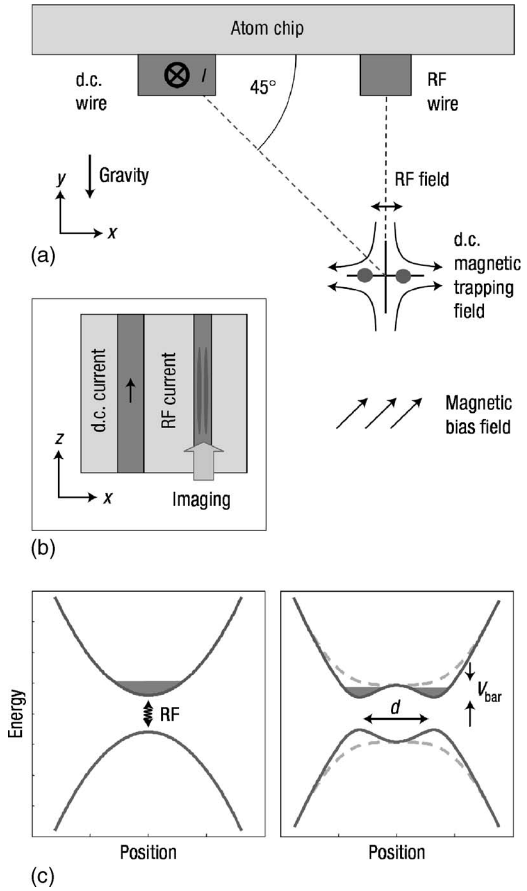

FIG. 47. Double-well potential generated by an oscillating magnetic field. (a) A straight wire carrying a static (dc) current (~1 A) is used to trap a BEC directly below a second wire carrying an rf current (~60 mA at 500 kHz). The dc wire has a width of 50 μm and is separated by 80 μm from the rf wire (width 10 μm). Placing the trap 80 μm below the chip surface at the indicated position allows for symmetric horizontal splitting. (b) Top view of the chip: An elongated BEC is transversely split. (c) Left: the rf magnetic field couples different atomic spin states (only two are shown for simplicity). Right: Under the influence of the rf field with a frequency below the Larmor frequency at the trap minimum (~1 G) the initial dc trapping potential is deformed into a double-well potential. Also shown is the slight relaxation of the trap in the vertical (y) direction (dashed line), and the splitting along the horizontal (x) direction, with a well separation d and potential barrier height V_{bar} (solid line). Adapted from Schumm, Hofferberth, *et al.*, 2005.

In another experiment, Schumm, Hofferberth, *et al.* (2005) realized a double-well potential by means of rf-controlled adiabatic potentials (Sec. II.D.7). A standard magnetic microtrap with harmonic confinement is formed by the fields of a single-current carrying wire (dc wire), a bias field, and an axial offset field (Sec. II.B). The bias field is tilted by 45° relative to the chip surface such that the symmetry axes of the two-dimensional quadrupole, responsible for the radial confinement, are parallel and perpendicular to the chip surface, respectively [Fig. 47(a)]. The trap is positioned 80 μm above an independent rf wire, parallel to the long axis of the trap. Driven with an alternating current, the rf wire creates an oscillating field that generates an adiabatic potential by coupling a high-field-seeking to a low-field-seeking state. Controlling the frequency and magnitude of the oscillating field, a single-well magnetic trap can be continuously transformed into a double-well potential. Given the geometry in Fig. 47, the trap splits horizontally. The scheme exploits the inhomogeneous coupling that depends on the relative orientation of the oscillating field vector and the static magnetic field. The latter defines the local quantization axis for the atomic spin such that the coupling is strongest for perpendicular static and the oscillating fields. Since the rf magnetic field vector oscillates parallel to the (horizontal) x axis, it is perpendicular to the trapping field at each position along the y axis. The rf coupling is thus homogeneous along the y direction and leads to a slight relaxation of the vertical confinement [Fig. 47(c)]. Along the horizontal x direction the situation is different. The coupling is strongest at the trap center, where the magnetic trapping field is dominated by offset field B_{off} along the z axis. The coupling reduces for larger distances to the trap center, where the static field is dominated by an x component. This spatial variation of the rf coupling breaks the rotational symmetry of the trap and allows for the formation of a double-well potential.

The experiments were done with highly anisotropic (aspect ratio ~400), quasi-one-dimensional condensates ($\mu \sim \hbar\omega_\perp$), containing up to 10^5 $|F=2, m_F=2\rangle$ ^{87}Rb atoms. The trap was characterized by the radial oscillation frequency $\omega_\perp = 2\pi \times 2.1$ kHz and an offset field of ~1 G. For splitting a condensate into parts separated by up to 6 μm, the frequency of the rf magnetic field was held constant at ~500 kHz, which is below the Larmor frequency at the trap center (~700 kHz for 1 G), and its amplitude was continuously increased from zero to a final value, corresponding to a current in the rf wire of 60–70 mA. Larger cloud separations of up to 80 μm have been reached by raising the rf up to 4 MHz.

The coherence properties of the splitting process have been analyzed for cloud separations between ~3 and ~5.5 μm (center-to-center distance). For larger separations, the interference pattern, detected after 14 ms time of flight, was not resolved by the imaging system. For separations smaller than 3.4 μm a constant relative phase of the condensates was observed. This was due to tunnel coupling between the two wells. For distances larger than ~3.4 μm, the potential barrier was sufficiently high to suppress tunnel coupling and a deterministic evolution of the relative phase was observed (Fig. 48). The phase evolution is due to any imbalance of the double-well potential. Its sign was successfully controlled by changing the relative height of the two wells.

A randomization of the relative phase was observed to occur on the time scale of 2.5 ms after the splitting was complete, independent of the splitting distance. A possible explanation of this loss of phase relation is the longitudinal phase diffusion inside the individual quasi-one-dimensional condensates (Whitlock and Bouchoule, 2003). Detailed experiments were done for a splitting speed of ~0.6 μm/ms (speed of well separation). For splitting times shorter than 2 ms the spread of the spatial phase distribution stays below the expectation for randomized phases by more than three standard deviations [Fig. 48(c)]. Within these limits, the data show an increase in phase spread and a related loss of average contrast [Figs. 48(a) and 48(b)]. For a fast splitting of 1.4 μm/ms, the relative phase evolution was found to be nonrandom within the observed splitting range (3–5.5 μm well separation).

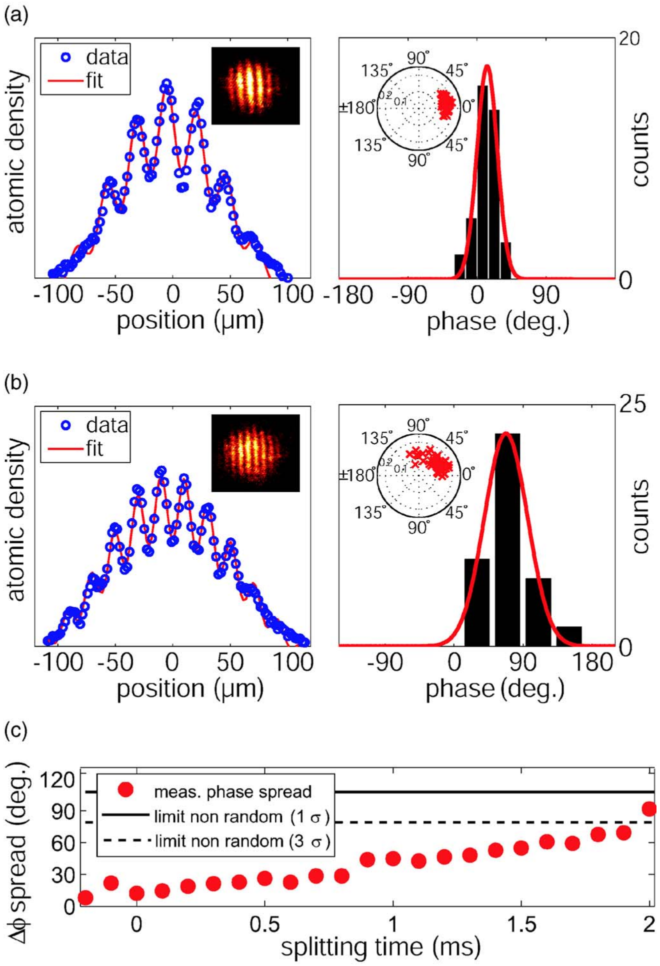

FIG. 48. (Color online) Coherence of the splitting is examined by analyzing matter-wave interference. (a) Interference pattern 0.1 ms after the splitting for a cloud separation of $d = 3.4$ μm. Tunneling through the barrier is inhibited. (b) Interference pattern 0.8 ms after the splitting for a cloud separation of $d = 3.85$ μm. Left: A cosine function with a Gaussian envelope is fitted to the profiles derived from the two-dimensional images (insets). Right: Contrast and relative phase for 40 realizations of the same experiment are plotted in a polar diagram (inset). A histogram of the same data shows a narrow distribution of the differential phase ($\sigma = 13°$) directly after separating the clouds and a slightly broadened distribution ($\sigma = 28°$) some time later. (c) The spread of the spatial phase is shown for different stages of the splitting process. The relative phase of the condensates shows a nonrandom behavior in the first 2 ms of the splitting. Adapted from Schumm, Hofferberth, *et al.*, 2005.

It will be interesting to study further the splitting of quasi-one-dimensional and three-dimensional condensates in order to learn more about their suitability for the construction of on-chip interferometers. Adiabatic potentials seem to allow for well controlled, robust, and smooth methods for splitting condensates. For a more recent experiment see Jo *et al.* (2006).

V. ATOMS IN THE PROXIMITY OF THE MICROTRAP SURFACE

The development of microtraps is motivated by numerous promising applications in matter-wave interferometry, precision force measurement, low-dimensional physics, and quantum information processing. These proposals require coherence and full quantum control over the internal and external states of atoms. Full quantum control over the motion of ultracold atoms of mass m and an energy uncertainty ΔE requires potentials that vary on the length scale $\lambda \approx h/(m\Delta E)^{1/2}$, typically a micron or less. Since a smaller λ allows for a larger ΔE, the atomic dynamics in an integrated circuit can be faster in a miniaturized potential due to the energy-time uncertainty principle. Strongly confining potentials are routinely created using standing-wave optical fields but they can also be realized in magnetic microtraps at small distances $d \leq \lambda$ from the miniaturized field sources. However, at such small distances from the surface the atom can no longer be treated as an isolated system.

Atoms interact with fluctuations of the electromagnetic field which are substantially modified in the vicinity of a trap surface. This leads to several important effects. Magnetic field fluctuations can induce transitions between internal spin states, leading to internal decoherence and finally to the loss of the atom because only low-field-seeking states are confined in the magnetic trap. Magnetic field fluctuations also lead to fluctuations in the trap position, causing heating and decoherence of the center-of-mass motion if transitions between vibrational states of the trap are involved.

Fluctuations of the electromagnetic field are also responsible for the Lamb shift of the atomic ground state. The modification of the field in close proximity to a dielectric material leads to a spatial variation of the Lamb shift and gives rise to attractive forces between the atom and surface, known as van der Waals and Casimir-Polder forces.

Besides these fundamental interactions, experiments with ultracold atoms have to face technical effects in the vicinity of the microstructure surface. It has been observed that ultracold clouds break up into fragments along the length of a current carrying wire as a result of corrugated trapping potentials. Due to geometrical imperfections of real microfabricated wires, the current exhibits small transversal components that produce a spatially modulated magnetic field. The importance of this effect depends on the wire quality, and it has been observed even for large atom-surface separations. Corrugations due to electrostatic patch potentials produced by alkali-metal atoms adsorbed onto the chip surface have also been observed.

A. Decoherence of internal spin states and atom loss due to magnetic field fluctuations

1. Transition rate between internal spin states

Let us consider an atom with total spin F, which is the sum of the electron spin, orbital angular momentum, and nuclear spin. The matrix elements of the magnetic moment are given by

$$\boldsymbol{\mu} = \langle f|\hat{\mu}|i\rangle = \langle f|\mu_B g_F \hat{F}|i\rangle, \tag{71}$$

where $\hat{\mu}$ is the magnetic moment operator, μ_B is the Bohr magneton, $\hat{F}$ is the total spin operator, g_F is the corresponding g factor, and $|i\rangle$ and $|f\rangle$ are internal spin states $|F,m_F\rangle$ of the atom, characterized by the total spin F and the magnetic quantum number m_F. In a magnetic field B, the $|F,m_F\rangle$ spin states are nondegenerate. The energy spitting, given by the Zeeman interaction, is

$$\hbar\omega_{if} = g_F \mu_B |B|. \tag{72}$$

Here ω_{if} is the Larmor frequency. Fluctuations of the magnetic field at the frequency ω_{if} couple spin states, leading to decoherence and atom loss in a conservative magnetic trap where only low-field-seeking states are trapped. In free space, where magnetic field fluctuations are due to thermal blackbody radiation, this loss mechanism is negligible, as we will see below. Close to a metallic surface, however, the magnetic field noise is significantly increased which sets important constraints on the design of microtraps.

The effect of the surface on magnetic field fluctuations can be interpreted in two ways. In the language of quantum electrodynamics, the absorption of blackbody radiation by the metal surface leads to dissipation and hence to additional fluctuations of the field. Alternatively, one can consider the surface as an electrical resistance at a finite temperature. Thermally induced currents therefore fluctuate in the surface (Johnson noise). The electromagnetic near-field radiation associated with these currents results in increased fluctuations of the electromagnetic field close to the surface. These two pictures can be shown to be equivalent, and the choice of one over the other is usually made only to simplify calculations. For magnetic microtraps the enhanced losses close to the surface due to Johnson-noise-induced spin flips were predicted by Henkel *et al.* (1999) and experimentally first observed by Jones, Vale, Sahagun, Hall, and Hinds (2003).

An important characteristic of thermally induced magnetic near-field noise is its frequency spectrum which depends on the properties of the metallic surface. The fluctuations are related to the imaginary part of the complex permittivity $\varepsilon(\mathbf{r},\omega)$, which characterizes the dissipation in the metal. In the relevant frequency range, much lower than the resonance frequency of surface excitations (for metals the plasma frequency $\sim 10^{13}$ Hz), the relation between the permittivity ε and resistivity ρ is $\varepsilon \approx i/\varepsilon_0\rho\omega = i2/k^2\delta^2$. The skin depth

$$\delta = \sqrt{2\varepsilon_0\rho\omega}/k = \sqrt{2\rho/\mu_0\omega} \tag{73}$$

is the characteristic length scale on which an electromagnetic wave entering the metal is damped. It is the skin depth that determines the spectral distribution of the electromagnetic near field. For thin layers $h \ll \delta$, the magnetic field fluctuations have the white noise spectrum of Johnson noise. In thick layers, damping becomes relevant and the spectrum is different. The skin depth is an important parameter in scaling laws for spin-state transitions above a surface.

The transition rate $\Gamma^B_{i\to f}(\mathbf{r})$ of internal spin states in the presence of magnetic field radiation is given by Fermi's golden rule

$$\Gamma^B_{i\to f}(\mathbf{r}) = \sum_{\alpha,\beta=x,y,z} \frac{\langle i|\hat{\mu}_\alpha|f\rangle\langle f|\hat{\mu}_\beta|i\rangle}{\hbar^2} S^{\alpha\beta}_B(\mathbf{r},\omega_{fi}), \tag{74}$$

where we used the Cartesian coordinates α and β and the components $\hat{\mu}_\alpha$ and $\hat{\mu}_\beta$ of the magnetic moment operator (Henkel *et al.*, 1999; Rekdal *et al.*, 2004). The spectral density of the magnetic field,

$$S^{\alpha\beta}_B(\mathbf{r},\omega_{fi}) = \int_{-\infty}^{\infty} d\tau \langle B_\alpha(\mathbf{r},t+\tau)B_\beta(\mathbf{r},t)\rangle e^{i\omega_{fi}\tau}, \tag{75}$$

is taken at the position $\mathbf{r}$ of the atom and the transition frequency ω_{if} (Larmor frequency). It is convenient to take the quantization axis z parallel to B_{off}, the magnetic offset field in the center of the harmonic trap. The matrix elements of the magnetic moment operator are then calculated using $\langle f|\hat{\mu}_\alpha|i\rangle = \mu_B g_F \langle f|\hat{F}_\alpha|i\rangle$ and the operators $\hat{F}_\pm = \hat{F}_x \pm i\hat{F}_y$, with their algebraic property

$$\hat{F}_\pm|F,m_F\rangle = \sqrt{F(F+1) - m_F(m_F \pm 1)}|F,m_{F\pm1}\rangle,$$

$$\hat{F}_z|F,m_F\rangle = m_F|F,m_F\rangle. \tag{76}$$

The spin matrix elements are

$$\langle f|\hat{F}_x|i\rangle = \frac{1}{2}(\langle f|\hat{F}_+|i\rangle + \langle f|\hat{F}_-|i\rangle),$$

$$\langle f|\hat{F}_y|i\rangle = \frac{i}{2}(\langle f|\hat{F}_-|i\rangle - \langle f|\hat{F}_+|i\rangle),$$

$$\langle f|\hat{F}_z|i\rangle = m_F\delta_{fi}. \tag{77}$$

For example, for ^{87}Rb the squares of the matrix elements entering the loss rate at the $|F,m_F\rangle = |2,2\rangle \to |2,1\rangle$ transition are $|\langle 2,1|\hat{F}_x|2,2\rangle|^2 = |\langle 2,1|\hat{F}_y|2,2\rangle|^2 = 1$ and $|\langle 2,1|\hat{F}_z|2,2\rangle|^2 = 0$.

Now, we calculate the lifetime $\tau = 1/\Gamma^B_{i\to f}$ of a spin state. The spectral density of the magnetic field in free space is given by the thermal blackbody radiation spectrum

$$S^{\alpha\beta}_{B,\text{Bb}}(\mathbf{r},\omega) = S^{\alpha\beta}_{B,\text{Bb}}(\omega)\,\delta_{\alpha\beta} = \frac{\mu_0\hbar\,\omega^3}{3\pi c^3}(n_{\text{th}}+1), \tag{78}$$

where $n_{\text{th}} = 1/(e^{\hbar\omega/k_BT}-1)$ is the Bose-Einstein distribution of the electromagnetic field modes. Blackbody radiation is uncorrelated, and $S^{\alpha\beta}_{B,\text{Bb}}(\omega)$ is diagonal. At zero temperature $n_{\text{th}} = 0$, the field is due to zero-temperature vacuum fluctuations (spontaneous radiation) and the resulting spin-state lifetime is

$$\tau_0 = \frac{1}{\Gamma^B_{i\to f}} = \frac{3\pi\hbar c^3}{\mu_0\omega^3 \sum_{\alpha=x,y,z} \mu_B^2 g_F^2 |\langle f|\hat{F}_\alpha|i\rangle|^2}. \tag{79}$$

For finite temperatures $n_{\text{th}} \gg 0$, and thermal radiation dominates. The corresponding lifetime in free space is $\tau_{\text{Bb}} = \tau_0/(n_{\text{th}}+1)$ (Purcell, 1946). Blackbody radiation has very little power at the Larmor frequency of atoms confined in magnetic traps, making loss and decoherence effects correspondingly small. For the above transition of ^{87}Rb, at the Larmor frequency $\omega/2\pi = 400$ kHz and room temperature, the lifetime τ_{Bb} is about 4×10^{18} s which is approximately the age of the Universe (Scheel *et al.*, 2005).

The presence of a surface enters into the above calculations as a modification of the spectral density tensor $S^{\alpha\beta}_B(\mathbf{r},\omega_{fi})$ of magnetic field fluctuations. Calculation of the spin-flip lifetime for a given conductor geometry therefore reduces to calculating the correct $S^{\alpha\beta}_B(\mathbf{r},\omega_{fi})$. A calculation of the magnetic field fluctuations above a metal surface was done by Varpula and Poutanen (1984) by incoherently summing up the field contributions of thermally induced currents (Johnson noise), characterized by the current dipole spectral density $4k_BT/\rho$ per unit volume. In the context of microtraps, Henkel and Pötting (2001) used this method for deriving scaling laws for various conductor geometries. Another method involving the application of the fluctuation dissipation theorem on the magnetic field itself (Agarwal, 1975) has been used by several authors for calculating magnetic noise above microtrap surfaces (Henkel *et al.*, 1999, 2003; Rekdal *et al.*, 2004; Henkel, 2005; Scheel *et al.*, 2005). In this framework, the magnetic Green's tensor is calculated above the metal surface whose imaginary part, multiplied by the thermal occupation number of photons, is proportional to the field's spectral density $S^{\alpha\beta}_B(\mathbf{r},\omega) = 2\hbar(n_{\text{th}}+1)\text{Im}\,G_{\alpha\beta}(\mathbf{r},\omega)$. The Green's tensor $G_{\alpha\beta}(\mathbf{r},\omega)$ describes the magnetic field of an oscillating pointlike magnetic dipole at the position of the atom. The total field then is described by the sum of the magnetic field in free space plus the field reflected from the metal surface. For calculating the reflected field, the free-space dipole field is expanded in plane waves and Fresnel reflection coefficients are applied for each incident wave: see, e.g., Henkel *et al.* (1999). The resulting Green's tensor characterizes the modification of the radiation in the near field of the surface. All information on the dielectric (absorbing) matter is contained, via the permittivity $\varepsilon(\mathbf{r},\omega)$, in the Green's tensor of the classical problem. The problem reduces to finding the Green's tensor for a given conductor geometry.

There are straightforward routines to numerically calculate the Green's tensor for different geometries. Rekdal *et al.* (2004) calculated the radiation field for a cylindrical geometry and found good agreement with the experimental data published by Jones, Vale, Sahagun, Hall, and Hinds (2003). The same authors reported the analysis for the data taken by Lin *et al.* (2004) above a thin conducting layer (Scheel *et al.*, 2005).

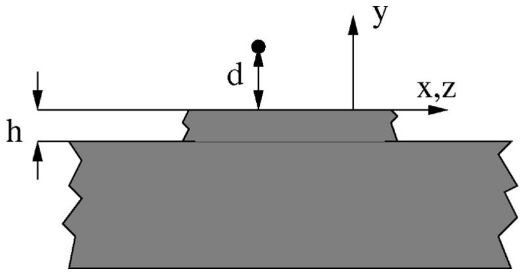

FIG. 49. Schematic of the geometry of microstructures as used for calculations of the lifetime by Scheel *et al.* (2005). A plane metallic layer of thickness h lies parallel to the (x,z) plane above a nonmetallic substrate. The atom is located in vacuum at a distance d from the surface. From Scheel *et al.*, 2005.

2. Spin-flip limited lifetime and decoherence near surfaces

Analytical results for the spin-flip limited lifetime near surfaces have been derived in several regimes that are distinguished by the relationship between three independent length scales: the thickness of the metal h, the atom-surface distance d, and the skin depth δ (Fig. 49) (Agarwal, 1975; Henkel *et al.*, 1999, 2003; Henkel and Pötting, 2001; Rekdal *et al.*, 2004, 2006; Henkel, 2005; Scheel *et al.*, 2005). The results as given by Scheel *et al.* (2005) are summarized as follows:

$$\tau=\left(\frac{8}{3}\right)^2\frac{\tau_0}{n_{\mathrm{th}}+1}\left(\frac{\omega}{c}\right)^3\times\begin{cases}\dfrac{d^4}{3\delta}, & \delta\ll d,h\\[2ex] \dfrac{\delta^2 d}{2}, & \delta,h\gg d\\[2ex] \dfrac{\delta^2 d^2}{2h}, & \delta\gg d\gg h.\end{cases}\qquad(80)$$

The first two equations describe the lifetime above a thick slab and the third equation the case of a thin film, which is the case for most microtraps in use today. Since τ_0 contains the factor $(c/\omega)^3$, the Larmor frequency enters the lifetime only through the expression for the skin depth.

Scheel *et al.* (2005) discussed the lifetime of an atom at a distance of 50 μm from a metal surface as a function of the skin depth in some detail. The results of numerical calculations for a thin metal layer and a thick metal slab are plotted in Fig. 50. At a Larmor frequency of 500 kHz, the skin depth for metals such as copper or aluminum is on the order of 100 μm. Under these conditions the lifetime at a distance of 50 μm is significantly longer above a thin metal film ($h=1$ μm) than above bulk metal. In addition, the lifetime exhibits a minimum at a skin depth on the order of $\delta_{\min}\approx\sqrt{hd}$ for a thin film and $\delta_{\min}\approx d$ for a thick slab. Thus atom-surface distances similar in magnitude to the skin depth have to be avoided. This has important consequences for the micron-scale structures required for matter-wave interferometers and many quantum information processing schemes.

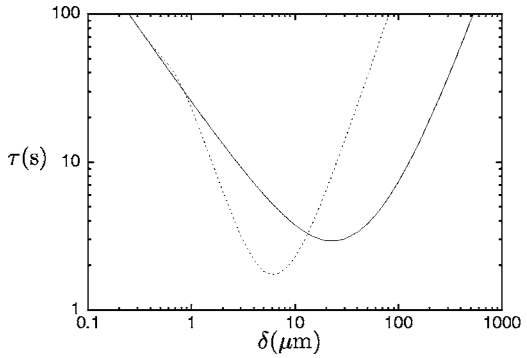

FIG. 50. Lifetime τ as a function of skin depth δ with the atom-surface distance fixed at 50 μm. Solid line, infinitely thick surface. Dotted line, 1 μm thick surface. The calculation was done for a spin-flip frequency of 560 kHz and a temperature of 300 K. From Scheel *et al.*, 2005.

The use of superconducting wires, e.g., niobium at $T\approx4$ K with a skin depth of 1 μm or less, could boost the spin relaxation time to 10^3 s, at tens of microns away from the surface. This significant enhancement of the lifetime is due to the small value of n_{th} and the small skin depth (Henkel, 2005; Scheel *et al.*, 2005). The spin decoherence time above superconducting surfaces (bulk materials) has been investigated also by Skagerstam *et al.* (2006).

Decoherence of spatial superposition states of atoms due to thermally induced spin-flip transitions were investigated by Henkel and Pötting (2001), Henkel *et al.* (2003), and Fermani *et al.* (2006). There are analytic and numeric solutions quantifying the coherence time and coherence length for experimentally relevant scenarios. In the most recent article, Fermani *et al.* (2006) considered the atom magnetically trapped at a distance d to a dielectric surface. The atom is coherently split into a double-well potential to a lateral separation l where tunneling is inhibited. This scenario is particularly interesting when spatial coherence is used to encode quantum information. Analytic results found for small lateral separations l predict that the spatial coherence decreases quadratically with l and inversely proportional to d^2. For large lateral separations and the case of thick metal layers, numerical solutions predict that the coherence length, defined to be the separation after which the coherence decays to half its initial value, converges to d.

3. Experimental results

Measurements on the spin relaxation loss in the near field of metallic surfaces have been reported by Jones, Vale, Sahagun, Hall, and Hinds (2003) for a cylindrical wire, by Harber *et al.* (2003) for a thick metal slab, and by Lin *et al.* (2004) for a thin metal film. Coherence lifetimes of internal spin states have been measured by Treutlein *et al.* (2004).

Cylindrical wire geometry. Jones, Vale, Sahagun, Hall, and Hinds (2003) measured the lifetime of an ultracold $|F=2,m_F=2\rangle$ ^{87}Rb cloud undergoing $|F,m_F\rangle=|2,2\rangle\rightarrow|2,1\rangle\rightarrow|2,0\rangle$ transitions in the near field of a cylindrical wire of 500 μm diameter. The wire itself consists of a central core of Cu with 185 μm radius, a 55 μm Al layer,

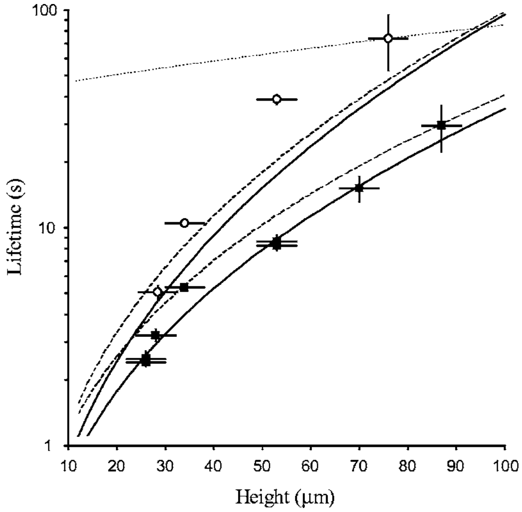

FIG. 51. Lifetime of trapped atoms versus distance from the Al surface of the cylindrical wire with 500 μm diameter. Solid squares (open circles), measurements with spin-flip frequency $\omega/2\pi=560$ kHz ($\omega/2\pi=1.8$ MHz). Solid (dashed) lines, calculated lifetimes above a thick slab of copper (aluminum) for these two spin-flip frequencies. Dotted line, expected scaling for technical noise. From Jones, Vale, Sahagun, Hall, and Hinds (2003). See also reanalysis of the exact conductor geometry by Rekdal *et al.* (2004).

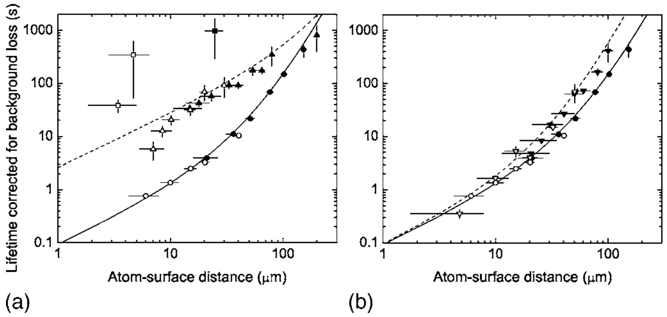

FIG. 52. Inferred lifetimes near the surfaces after subtraction of the background loss. (a) Resistivity dependence: Copper (circles), titanium (triangles), and silicon (squares) at $\omega/2\pi=1.80$ MHz. Open and solid symbols represent measurements made with condensates and normal clouds, respectively. Solid (dashed) line indicates lifetimes predicted for copper (titanium), based on numerical integration of Eq. (22) of Henkel *et al.* (1999). The dotted line, plotted for copper, shows the closed-form interpolation suggested by Henkel *et al.* (1999). (b) Larmor frequency dependence near copper: $\omega/2\pi=1.80$ MHz (circle) and $\omega/2\pi=6.24$ MHz (triangle). Solid (dashed) line indicates lifetimes predicted for $\omega/2\pi=1.80$ MHz ($\omega/2\pi=6.24$ MHz). From Harber *et al.*, 2003.

and a 10 μm thick ceramic sheath. The lifetime due to background collisions was about 100 s. Data points were taken over a range of distances between 27 and 90 μm from the surface of the metal, for two different Larmor frequencies: $\omega/2\pi=1.8(1)$ MHz and $\omega/2\pi=560(10)$ kHz. The lifetime exhibited a strong dependence on the distance to the surface, decreasing by an order of magnitude over the entire range (Fig. 51). These data showed that the lifetime was limited by Johnson-noise-induced spin flips. The solid (dashed) curves in Fig. 51 are numerical calculations using the equations of Henkel *et al.* (1999) for a thick plane slab of Cu (Al) and the given frequencies. For the same height, atoms with a lower spin-flip frequency have a lower lifetime. The expected scaling of the lifetime for technical noise is indicated by the dotted line, arbitrarily placed to pass through one of the data points. As experimentally verified by Leanhardt, Shin, *et al.* (2003), for any residual radio-frequency current in the wire, the resulting field would vary as $1/r$, giving a lifetime proportional to r^2. The observed height dependence is clearly much stronger. Also, spin flips induced by radio frequency pickup cause a loss rate proportional to the rf power at the spin-flip frequency, which would lead to a constant ratio of lifetimes for different spin-flip frequencies, not the observed height dependent ratio. The data have been reanalyzed by Rekdal *et al.* (2004), solving the spin relaxation rate for the double-layer cylindrical wire. The results of this more detailed calculation are in excellent agreement with the measured data.

Thick slab geometry. Experimental results on the spin relaxation rate above thick substrates have been given by Harber *et al.* (2003). Using thermal clouds and Bose-Einstein condensates of ^{87}Rb atoms in the $|F=1,m_F=-1\rangle$ state, the lifetime was measured above three different substrate materials: copper, titanium, and silicon, with corresponding resistivities of $1.67(8)\times10^{-8}$ Ω m, $4.88(24)\times10^{-7}$ Ω m, and >1 Ω m and thicknesses of 1 mm. The results for spin-flip frequencies $\omega/2\pi=1.8$ and 6.24 MHz are shown in Fig. 52. The background-gas-limited lifetime ($\tau_{\mathrm{BG}}=120$ s) has been subtracted from the measured lifetime as $\tau=(1/\tau_{\mathrm{meas}}-1/\tau_{\mathrm{BG}})^{-1}$ to yield the surface-limited lifetime τ. The lifetime over copper drops significantly faster than over titanium, which has a resistivity 28 times larger than copper. Over silicon, no statistically significant lifetime reduction was observed for atom surface separations >10 μm. The data were compared with numerical calculations of the lifetime following the theory derived by Henkel *et al.* (1999). Taking into account that the loss occurs via the $|F,m_F\rangle=|1,-1\rangle\rightarrow|1,0\rangle$ transition; there was good agreement between theory and experiment. At the shortest atom-surface distances, the measured lifetimes appeared to drop anomalously. This effect was also seen over silicon and this was attributed to a possible impact of the Casimir-Polder force.

Thin metal layer. Lin *et al.* (2004) measured the lifetime of a 1 μK cold thermal cloud of ^{87}Rb in the $|F=2,m_F=2\rangle$ state above a thin conductor with 2.15(20) μm thickness and 10 μm width. The conductor material was copper that was coated with thin layers of Ti (40 nm), Pd (50 nm), and Au (100 nm). The atoms were confined in a magnetic trap with $B_{\mathrm{off}}=0.57$ G offset field; thus, the skin depth ($\delta=103$ μm) at the transition frequency was much larger than the film thickness. In this case the magnetic field noise spectrum is frequency

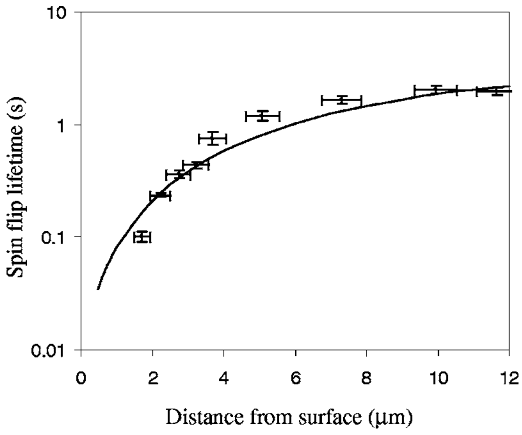

FIG. 53. Lifetime τ as a function of distance from the surface of a thin metal layer, for $B_{\text{off}}=0.57$ G (Lin *et al.*, 2004). Line: Calculated lifetime using a skin depth of 103 μm, a temperature of 400 K, and a spin-flip frequency of 400 kHz. For distances larger than 10 μm, the lifetime is limited by background gas collisions. Adapted from Lin *et al.*, 2004 and Scheel *et al.*, 2005.

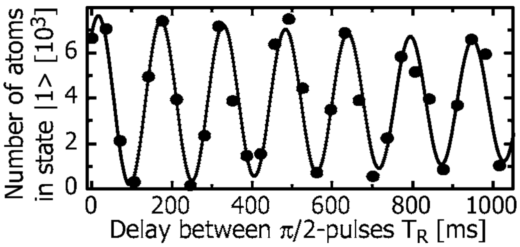

FIG. 54. Ramsey spectroscopy of the $|0\rangle \leftrightarrow |1\rangle$ transition with atoms held at a distance $d=9$ μm from the surface of a silver foil of 250 nm thickness. An exponentially damped sine fit to the Ramsey fringes yields a $1/e$ coherence lifetime of $\tau_c = 2.8 \pm 1.6$ s. Each data point corresponds to a single shot of the experiment. From Treutlein *et al.*, 2004.

independent. The lifetime data plotted in Fig. 53 show the characteristic spin relaxation loss when approaching the metal surface. For distances larger than 10 μm, the distance-independent one-body loss rate of $\gamma=0.4$ s^{-1} limited the lifetime. The data are compared with the numerical results of Scheel *et al.* (2005). The calculation just below 10 μm gives a slightly lower lifetime because the metal wire was only 10 μm wide, rather than being infinitely wide as supposed by the theory. At lower heights, where the infinite width is a good approximation, theory and experiment are in good agreement. Furthermore, Lin *et al.*, 2004 found the lifetime $\tau(d)$ measured for $B_{\text{off}}=1.5$ G and hence a transition frequency 3 times larger was compatible with a white noise spectrum for field noise within a 40% margin of error. In comparison, above a dielectric (Si coated with 1 μm Si_3N_4), a constant lifetime of 3.5 s was measured for $d > 2.5$ μm.

Decoherence time of a superposition of internal spin states. Treutlein *et al.* (2004) created coherent superpositions of two hyperfine ground states of ^{87}Rb, $|F=1, m_F=-1\rangle \equiv |0\rangle$ and $|F=2, m_F=1\rangle \equiv |1\rangle$, and performed Ramsay spectroscopy to determine the coherence lifetime. The atoms were initially prepared in state $|0\rangle$, in a magnetic microtrap characterized by $(\omega_x, \omega_y, \omega_z,)=2\pi \times (50,350,410)$ s^{-1} and $B_{\text{off}} \sim 3.23$ G. For this magnetic field, the two states $|0\rangle$ and $|1\rangle$ experience the same first-order Zeeman shift and the remaining field dependence of the corresponding transition frequency ν_{10} is minimized. The coupling of $|0\rangle$ and $|1\rangle$ was achieved by a two photon microwave–radio-frequency transition. The microwave frequency ν_{mw} was tuned to be 1.2 MHz above the transition frequency from $|0\rangle$ to the intermediate state $|F=2, m_F=0\rangle$, and was phased locked to the radio frequency ν_{rf}. By applying the two photon drive for variable time and detecting the atoms in state $|1\rangle$, a Rabi oscillation with a resonant two-photon Rabi frequency of $\sim$0.5 kHz was observed. The measurements were carried out in a microtrap generated by a current carrying gold wire of 50 μm width and 7 μm thickness. The wire was fabricated on an aluminum nitride substrate and was covered by an epoxy layer of 34 μm and an upper silver foil layer of 250 nm thickness. The silver foil, which was attached to allow operation of the mirror MOT, turns out to be the main source of thermally induced magnetic field noise close to the surface and is therefore important when investigating decoherence at small surface-atom separations. For Ramsey spectroscopy, atoms in state $|0\rangle$ were held in the measurement trap for a time T_H before a first $\pi/2$ pulse created the superposition of $|0\rangle$ and $|1\rangle$. After a delay T_R, a second $\pi/2$ pulse was applied, and the resulting state was probed. Time-domain Ramsey fringes were recorded by varying T_R while keeping $\Delta_R = \nu_{\text{mw}} + \nu_{\text{rf}} - \nu_{10}$ fixed ($\Delta R \ll \nu_{10} \approx 6.8$ GHz). Alternatively, frequency-domain Ramsey fringes were recorded by scanning Δ_R with constant T_R. To distinguish loss of population from loss of coherence $T_H + T_R$ was kept constant during the Ramsey scan. Figure 54 shows time-domain fringes at $d=9$ μm distance to the silver mirror surface. The number of atoms detected in state $|1\rangle$ oscillates at the frequency difference $\Delta_R = 6.4$ Hz, while the interference contrast decays with a coherence lifetime of $\tau_c = 2.8 \pm 1.6$ s.

Frequency-domain Ramsay scans with $T_R = 50$ ms and $T_R = 1$ s were repeated at distances d between 5 and 130 μm to the mirror surface. The contrast $C(T_R)$ was 85–100 % for $T_R = 50$ ms and 60–85 % for $T_R = 1$ s. Within experimental error, the contrast was independent of the atom-surface distance. However, it was dependent on the cloud temperature ($T \sim 0.2$–0.7 μK) and density [$n \sim (1-5) \times 10^{12}$ cm^{-3}], and thus decoherence was attributed to the residual differential Zeeman shift and density-dependent collisional shift of ν_{10} across the cloud. The lifetime of the atomic cloud was measured to decrease from 11 s for $d > 20$ μm to 1.6 s for $d=5$ μm, which is in agreement with Eq. (80). No measurement data were taken below 5 μm, where magnetic field fluctuations significantly limited the magnetic trap lifetime.

The results described above show that the impact of magnetic field noise near metallic surfaces is well understood and has been demonstrated experimentally. By taking these results into account, low-noise magnetic microtraps can be designed and constructed. In order to keep long magnetic trap and coherence lifetimes, metal surfaces close to the atomic cloud should be avoided and conductors for the manipulation of the cloud should be kept as thin and narrow as possible.

B. Excitation of vibrational states, decoherence, and heating

As well as decoherence and loss due to transitions between internal states, magnetic field fluctuations can also lead to heating and decoherence by driving transitions between the motional states of the trapped atoms. Here, rather than the Larmor frequency, it is the trap frequency Ω that sets the relevant frequency scale. Fluctuations of the equilibrium trap position at the resonance frequency Ω excite transitions to neighboring quantum states, from n to $n\pm1$. Fluctuations of the field curvature at 2Ω induce transitions from n to $n\pm2$ (parametric excitation).

The transition rates can be calculated using time-dependent perturbation theory, in a similar way to the calculations described above for internal states. The rate equation is given in terms of the matrix elements of the coupled vibrational states and the spectral density of the fluctuations at the transition frequency, as described by Gehm *et al.* (1998). The transition is always connected to energy transfer and leads to heating.

In microtrap experiments, low-frequency magnetic field fluctuations, responsible for transitions between center-of-mass quantum states, originate either from thermally excited currents in the substrate (Johnson noise) or from technical noise. Technical noise is predominantly homogeneous over the extension of the trap whereas Johnson noise produces a spatially inhomogeneous field distribution, resulting in different transition rate for the two cases. Henkel *et al.* (2003) investigated the case of a waveguide potential along a current carrying wire and derived an estimation for the transition rate $\Gamma_{0\to1}$ due to fluctuations of the driving current (technical noise):

$$\begin{aligned}\Gamma_{0\to1} &= \frac{M\Omega^3}{2\hbar}S_h(\Omega)\\ &\sim 3\ \mathrm{s}^{-1}\ (\mathrm{M/amu})\\ &\quad\times(\Omega/2\pi\times100\ \mathrm{kHz})^3\\ &\quad\times\frac{I/A}{(B_{\mathrm{bias}}/G)^2}\frac{S_I(\Omega)}{SN_I}. \end{aligned}\tag{81}$$

Here M is the atomic mass, I the wire current, B_{bias} the bias field for the waveguide as in Sec. II.B, and $S_h(\omega)$ the spectrum of the trap-position fluctuations, related to the spectrum of the current noise $S_I(\omega)$, both defined similar to Eq. (75). The current noise is divided by the spectrum of the shot noise $SN_I = eI \approx 0.16\ (\mathrm{nA}^2/\mathrm{Hz})\times(I/A)$, with e the charge quantum. Fluctuations in the trap position due to technical noise can be reduced by correlating the currents in the wire with those producing the bias fields (Estève *et al.*, 2005). The trap curvature, however, then fluctuates with a spectral density of $S_\Omega(\omega)$. Henkel *et al.* (2003) estimated the order of magnitude of the transition rate $\Gamma_{0\to2}$ for this parametric excitation to be

$$\begin{aligned}\Gamma_{0\to2} &= \frac{1}{2}S_\Omega(2\Omega)\\ &\sim 3\times10^{-8}\ \mathrm{s}^{-1}\frac{(\Omega/2\pi\times100\ \mathrm{kHz})^2}{(I/A)}\frac{S_I(2\Omega)}{SN_I},\end{aligned}\tag{82}$$

which is substantially smaller than the rate $\Gamma_{0\to1}$ above. In comparison, the transition rate due to thermally excited magnetic near-field noise (*Johnson noise*) above a metallic half space is estimated by

$$\begin{aligned}&\Gamma_{0\to1,\mathrm{Johnson\ noise}}\\ &\quad\approx\frac{1\ \mathrm{s}^{-1}(\mu/\mu_B)^2[T_S/(300\ \mathrm{K})]}{(\mathrm{M/amu})(\Omega/2\pi\times100\ \mathrm{kHz})(\rho/\rho_{\mathrm{Cu}})(d/\mu\mathrm{m})^3}.\end{aligned}\tag{83}$$

Here μ is the magnetic moment of the atom, μ_B the Bohr magneton, T_S the substrate temperature, and ρ the resistivity of the metal substrate related to ρ_{Cu}, the resistivity of copper. The estimation follows within its range of validity $d \ll \delta(\omega)$ the power law $1/d^3$, where $\delta(\omega)$ is again the skin depth. It shows that at a distance of $d = 1\ \mu\mathrm{m}$ above a room-temperature copper surface, the ground-state excitation rate, e.g., for rubidium atoms in a trap with $\Omega/2\pi = 10$ kHz is on the order of $0.1\ \mathrm{s}^{-1}$, which is about two orders of magnitude smaller than typical transitions rates calculated for internal spin states under the same conditions.

Schroll *et al.* (2003) calculated the decoherence of the atomic motion in a waveguide potential due to thermal current fluctuations in the one-dimensional conductor used for creating the waveguide. Spatial decoherence along the 1D waveguide axis appears due to transitions between transverse trap states. The equation for the atomic density matrix was derived which describes decoherence and equilibrium effects in multiple-wire traps. Single- and two-wire guides are explicitly discussed. For the single-wire guide, the decoherence rate was found to scale as $\Gamma \propto 1/r_0^4$, with r_0 the distance between wire and trap center. For 10 μm atom-surface separation, a decoherence rate of $\Gamma \approx 0.03\ \mathrm{s}^{-1}$ has been derived. Since the potential fluctuations are correlated over a length scale of r_0, the decoherence rate Γ is a function of the relative coordinate along the waveguide axis.

As yet, no experimental results are available on heating due to Johnson noise.

C. Dispersion forces

Fluctuations of the electromagnetic field interact with charged particles and induce virtual electronic transitions in atoms. The corresponding energy shifts are known as Lamb shifts. In the vicinity of a dielectric surface (e.g., a conducting plate), the spectral density of the fluctuating field is substantially modified for frequencies below $\sim c/d$ (d the distance to the surface), resulting in a spatially varying Lamb shift. The gradient of the Lamb shift gives rise to an attractive force. Since the atom is in its ground state, virtual excitation exists only for a time on the order of $\lambda/2\pi c$ or less, in accordance with the uncertainty principle. λ is the wavelength of the resonance transitions involved which for alkali-metal atoms is predominantly the wavelength of the $D1$ and $D2$ lines, placing a distance limit of the order of $\lambda/2\pi$ on the short-range *van der Waals* interaction. The van der Waals interaction is a result of the instantaneous response of the surface to virtual dipole oscillations of the atom and is described by a power law $U_{\mathrm{vW}} \propto 1/d^3$. Outside that range, $d \gg \lambda/2\pi$, retardation has to be included due to the finite speed of light. The potential becomes weaker and approaches for asymptotically large distances the power law $U_{\mathrm{CP}} \propto 1/d^4$, known as the long range Casimir-Polder interaction (Casimir and Polder, 1948; Buhmann, Ho, and Welsch, 2004; Buhmann, Knöll, and Welsch, 2004).

A precise measurement of the Casimir-Polder force using a magnetically trapped ^{87}Rb Bose-Einstein condensate has been reported by Harber *et al.* (2005). The force gradient perpendicular to the surface of a fused silica substrate was detected by the change of the frequency of the center-of-mass oscillation of a condensate. The Casimir-Polder force was detected at relatively large cloud-surface separations of the order of $\sim 5\ \mu$m. A related theory has been given by Antezza *et al.* (2005). The temperature dependence of the Casimir-Polder force has been recently measured by Obrecht *et al.* (2006).

1. Limitation of the trap depth

In the context of microtraps, it has been shown experimentally that the impact of the Casimir-Polder potential lowers the trap depth and the trap disappears at a finite distance d when approaching the surface (Lin *et al.*, 2004). Ultracold thermal atoms at temperatures of $2.1\ \mu$K and $4.6\ \mu$K and Bose-Einstein condensates at $T_c/2$ were held in a magnetic microtrap with $\omega_r/2\pi = 3.6$ kHz for 15 ms at different distances d above a Si_3N_4 substrate surface. The number of atoms remaining in the trap was measured with the result that thermal clouds exhibit loss at larger distances than the condensate and the latter vanished at a finite distance $d = 1\ \mu$m (Fig. 55). The loss process was modeled as a sudden loss of the Boltzmann tail of the thermal momentum distribution as atoms are brought near the surface, in conjunction with 1D evaporation. The remaining fraction after sudden loss is given by $F = 1 - e^{-\eta}$ with $\eta = U_0/k_B T$, where $U_0(d)$ is the Casimir-Polder force-limited trap depth (Fig. 55, inset). The Casimir-Polder potential was accounted for using the equation $U_{\mathrm{CP}} = -C_4/d^4$, with the coefficient $C_4 = \psi(\varepsilon) 3\hbar c \alpha / 32\pi^2 \varepsilon_0$, where $\alpha = 5.25 \times 10^{-39}$ F m^2 is the rubidium polarizability and $\psi(\varepsilon) = 0.46(5)$ is a dimensionless numerical factor following the lines of the theory in Yan *et al.* (1997) for the dielectric constant $\varepsilon = 4.0(8)$ of the Si_3N_4 surface. The calculated fraction of atoms remaining is plotted as solid lines in Fig. 55. For comparison, the dashed lines show the calculated fraction in the absence of any surface potential ($C_4 = 0$). The measurement in combination with the 1D evaporation model implies a 66% confidence range for C_4 between 1.2×10^{-56} and 41×10^{-56} J m^4, which includes the nominal value $C_4 = 8.2 \times 10^{-56}$ J m^4, suggesting that the Casimir-Polder potential limited the trap depth, and consequently the lifetime, at small distances $d \leq 2\ \mu$m from the dielectric surface.

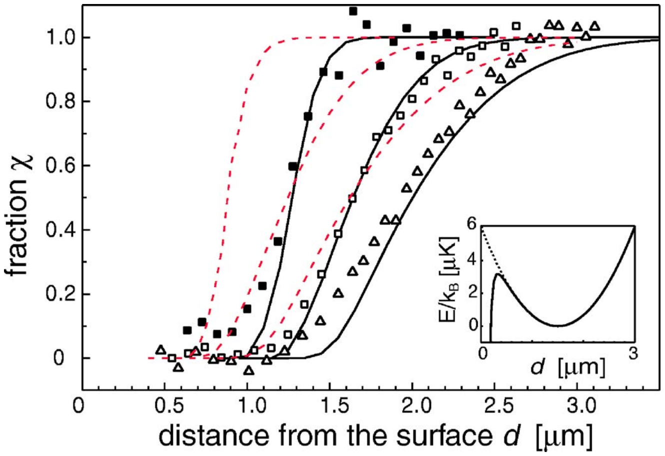

FIG. 55. (Color online) Remaining atom fraction χ in a trap at distance d from the dielectric surface for a condensate (solid squares), and for thermal clouds at $2.1\ \mu$K (open squares) and $4.6\ \mu$K (triangles). The solid (dashed) lines are calculated with (without) Casimir-Polder potential for the condensate, the $2.1\ \mu$K and $4.6\ \mu$K clouds (left to right). Inset: The trapping potential for $C_4 = 8.2 \times 10^{-56}$ J m^4 (solid line) and $C_4 = 0$ (dotted line). From Lin *et al.*, 2004.

2. Quantum reflection

Quantum reflection of ultracold atoms from the attractive potential of a solid surface has been studied by Pasquini *et al.* (2004). Extremely dilute Bose-Einstein condensates of ^{23}Na, with peak density 10^{11}–10^{12} atoms/cm^3, confined in a weak gravitomagnetic trap (Leanhardt, Pasquini, *et al.*, 2003) were reflected at normal incidence from a silicon surface. Reflection probabilities of up to 20% were observed for incident velocities of 1–8 mm/s. The reflection probability agrees qualitatively with the prediction for quantum reflection from the attractive Casimir-Polder potential (Fig. 56). A quantum mechanical treatment of an atom-surface collision reveals that the atom is reflected from the purely attractive surface potential if the potential energy changes abruptly on a length scale set by the quantum mechanical wavelength. The condition for significant reflection is that the local particle wave number normal to the surface, $k_{\perp} = \sqrt{k_{\infty}^2 - 2mU/\hbar^2}$, change by more than $k_{\perp}$ over a distance $1/k_{\perp}$. Here $k_{\infty} = mv_{\perp}/\hbar$ is the normal wave number of the atom far from the surface, with $v_{\perp}$ the normal incident velocity. The reflection

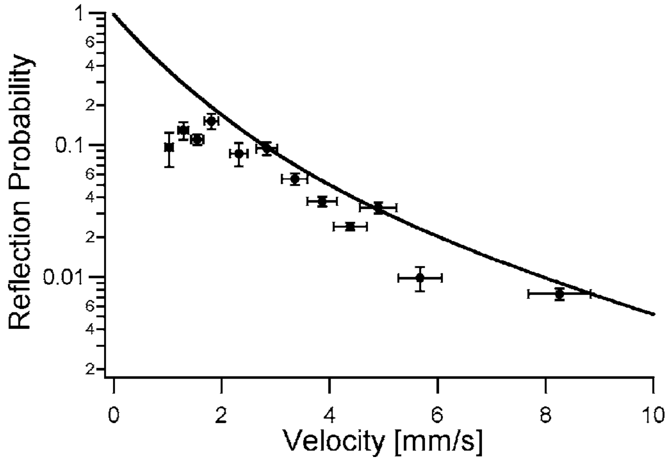

FIG. 56. Reflection probability vs incident velocity. Data were collected in a magnetic trap with trap frequencies $2\pi \times (3.3, 2.5, 6.5)\ \mathrm{s}^{-1}$. Incident and reflected atoms were averaged over several shots. Vertical error bars show the standard deviation of the mean of six measurements. Horizontal error bars reflect the uncertainty in deducing $v_\perp$. The solid curve is a numerical calculation for individual atoms incident on a conducting surface. From Pasquini *et al.*, 2006.

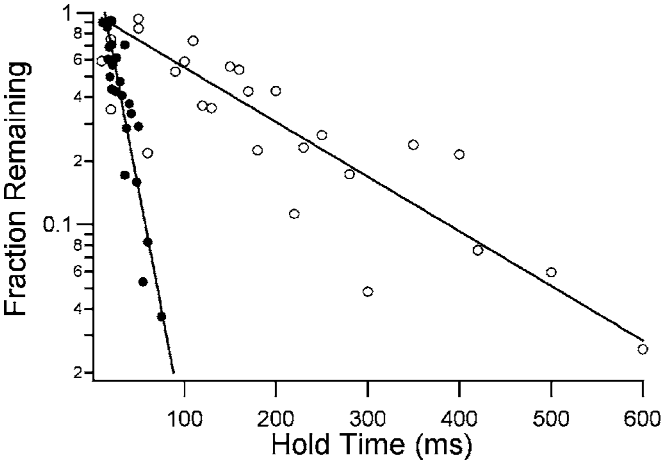

FIG. 57. Lifetime in the Si surface trap. Solid (open) circles show the remaining atom fraction vs time for a $2\pi \times (9,9,6.5)\ \mathrm{s}^{-1}$ $[2\pi \times (3.3,2.5,6.5)\ \mathrm{s}^{-1}]$ trapping potential with an initial atom number 3×10^4 $[9 \times 10^4]$. The solid line exponential fit gives a lifetime of 23 ms (170 ms) for the high- (low-) frequency trap geometry. The lifetime for atoms confined far from the surface exceeded 20 s for either geometry. From Pasquini *et al.*, 2004.

probability R tends to unity as the incident velocity tends to zero, $R \approx 1 - 4\beta_4 m v_\perp / \hbar$, where β_4 is the length scale associated with the coefficient $C_4 = \beta_4^2 \hbar^2 / 2m$. A high probability for quantum reflection therefore requires low incident velocity or weak attraction to the surface. In the limit of zero incident velocity, a surface acting as an ideal atom mirror could be used to construct a physical container for ultracold atoms and Bose-Einstein condensates.

Pasquini *et al.* (2004) examined the feasibility of confining atoms with solid surfaces. Atoms were held in a magnetic trap divided in half by a vertical silicon surface. Figure 57 shows the remaining fraction of atoms in the trap as a function of hold time for two different magnetic trap parameters $(\omega_\perp, \omega_y, \omega_z) = 2\pi \times (9, 9, 6.5)\ \mathrm{s}^{-1}$ and $2\pi \times (3.3, 2.5, 6.5)\ \mathrm{s}^{-1}$. Here $\omega_\perp$ is the horizontal trap frequency perpendicular to the surface, ω_y the horizontal trap frequency parallel to the surface, and ω_z the vertical trap frequency. The lifetime for the high- (low-) frequency trap was 23 ms (170 ms). In comparison the lifetime far from the surface exceeded 20 s. The loss of atoms was attributed to scattering with the surface and adsorption. Fluctuating magnetic fields could also induce losses (see previous section); however, in the particular experiment with $B_{\mathrm{off}} \sim 10$ G, a corresponding spin-flip frequency of ~ 7 MHz and an average distance to the surface of 15 μm, the decay rate was calculated to be negligible of less than 0.1 μHz. To estimate the effect of quantum reflection on the lifetime, the incident velocity of the atoms was taken to be proportional to the speed of sound $c = \sqrt{gn/m}$, which is related to the interaction energy in the condensate (Dalfovo *et al.*, 1999). Here $g = 4\pi\hbar^2 a/m$ is the coupling parameter associated with the atom-atom interaction and a is the s-wave scattering length. The atom loss rate from the surface was expressed as $dN/dt \propto -nSc(1-R)$, where S is the contact area between surface and condensate. The lifetime is then expressed as $\tau_L = -N/(dN/dt) = \chi T_\perp / (1-R)$, where χ is an undetermined numerical parameter independent of the trap frequency and $T_\perp = 2\pi/\omega_\perp$ is the trap period. Comparing the ratio $\tau_L / T_\perp$ for the two trap frequencies, χ cancels out. Assuming a reflection probability for the high-frequency trap of $R_h = 0$ gives a value for $R_l = 60\%$. A more reasonable assumption of $R_h = 20\%$ gives a value for $R_l = 70\%$.

Effects of the atomic interaction on the quantum reflection of Bose-Einstein condensates on solid surfaces were theoretically studied by Scott *et al.* (2005). For low incident velocities they find that the standing wave formed from the superposition of the incident and reflected waves generates dynamical excitations (solitons and vortex rings) that disrupt the condensate. This disruption could explain the anomalously low reflection in the experiment of Pasquini *et al.* (2004).

In a more recent work Pasquini *et al.* (2006) reported on quantum reflection of condensates on a pillared silicon surface. At low incident velocities (0.5–2.5 mm/s), reflection probabilities up to 60% were observed which are significantly enhanced as compared to previous results on a flat silicon surface. The experiment illuminates that the Casimir-Polder potential can be custom designed by structuring the surface. Similarly, a sequence of different surface layers could be used for shaping this potential.

In earlier experimental work, the long-range Casimir-Polder potential was measured by deflecting an atomic beam with low transversal velocity in a micron-sized parallel-plate cavity (Sukenik *et al.*, 1993) and was utilized for mirrors for atomic beams at grazing incidence (Shimizu, 2001), reflective diffraction gratings (Shimizu and Fujita, 2002a), and the realization of a hologram based on quantum reflection (Shimizu and Fujita, 2002a).

D. Disordered potential

1. Patch effect

When working with ultracold atoms near surfaces, it is likely that some of the atoms will become stuck to the surface. Depending on the substrate, it is possible for electrons in the adatom and the substrate to redistribute themselves, leading to nonzero electric fields from initially neutral objects. Magnetically trapped atoms brought near to a polarized surface will experience an attractive potential according to $U_{\mathrm{dip}}(r)=-(\alpha/2)E_{\mathrm{dip}}(r)^2$, where α is the ground-state dc polarizability of the atom [for ^{87}Rb ($\alpha=5.25\times10^{-39}$ F m$^2\cong79.6$ mHz/(V cm)^2] and $E_{\mathrm{dip}}(r)$ is the dipolar field at the distance r from the surface. The spatial scaling of $E_{\mathrm{dip}}(r)$ depends on the distribution of dipoles. For a pointlike dipole $E_{\mathrm{dip}}\sim1/r^3$, for a line distribution of dipoles $E_{\mathrm{dip}}\sim1/r^2$, and for a two-dimensional distribution $E_{\mathrm{dip}}\sim1/r$. This attractive force can limit the trap depth towards the surface (McGuirk *et al.*, 2004); for certain numbers and distributions of adatoms, this potential can become larger than the Casimir-Polder force discussed before. In addition, the small electric fields in close proximity to a nonuniform distribution of polarized adatoms can have large gradients that can corrugate the trapping potential.

McGuirk *et al.* (2004) measured the electric fields from polarized ^{87}Rb adsorbates on silicon, titanium, and BK7 glass surfaces in the range of 5–30 μm from the surface. Different amounts of rubidium were deposited on the substrate by successively moving Bose-Einstein condensates containing 5×10^5 atoms into the surface. Due to the elongated shape of the magnetic trap $(\omega_a,\omega_r)=2\pi\times(5.6,216)$ s^{-1}, the deposition resulted in a line-shaped distribution of adatoms. Even for the largest number of deposited atoms (200×10^5) the surface coverage was at most only a few percent of a monolayer. In order to measure the electric dipole field, nearly pure condensates containing $\sim10^5$ atoms were positioned at the desired distance to the surface and excited into a transverse dipole oscillation. With excitation lifetimes of several seconds ($Q\sim10^4$), the trap frequency was measured with high accuracy. The electrostatic potential of surface dipoles shifts the frequency of the trap. In order to amplify the electrostatic potential, McGuirk *et al.* (2004) applied an external field E_{app} normal to the surface, resulting in a total electric potential of $U_{\mathrm{el}}(r)=-(\alpha/2)|\mathbf{E}_{\mathrm{app}}+\mathbf{E}_{\mathrm{dip}}(r)|^2$. If the applied field is significantly larger than the surface dipole field, the effective potential is $U_{\mathrm{el}}(r)\approx-\alpha\mathbf{E}_{\mathrm{app}}\cdot\mathbf{E}_{\mathrm{dip}}(r)$. The net effect is that any surface-related field is amplified but also the spatial scaling of the resulting potential changes. The measured surface field E_{dip} as a function of deposited atoms is plotted in Fig. 58 (E_{dip} corresponds to E_{surface} in the figure). The inset shows the trap frequency as a function of applied voltage before and after one condensate was deposited. From these data and the distance dependence $1/r^{2.3}$ for Ti and $1/r^2$ measured without E_{app} for Si, consistent with a spatial distribution of adatoms between a point distribution and a line of dipoles, the authors derive the dipole moment of stuck ^{87}Rb atoms to be $\sim1\times10^{-29}$ C m on Si and Ti and 5–10 times smaller on glass. Substrates in which atom-surface bonds polarize are those with work functions comparable to or greater than the ionization energy of the adatom. For ^{87}Rb this is 4.2 eV, as compared to the work functions of Si (4.8 eV) and Ti (4.3 eV).

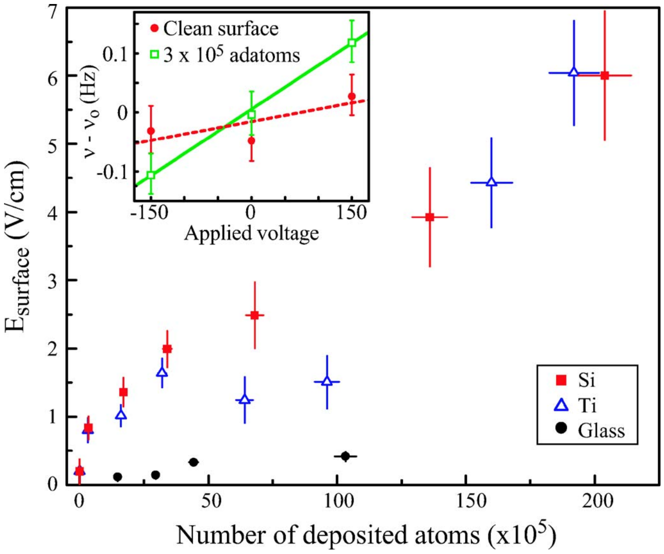

FIG. 58. (Color online) Surface-based electric field E_{dip} ($=E_{\mathrm{surface}}$) as a function of atoms stuck to the surface. Si (squares) and Ti (triangles) exhibit similar behavior, roughly increasing linearly with adsorbate number, while the glass substrate (circles) shows only a small effect of adsorbates. The distance between the center of the magnetic trap and the surface is fixed to 10 μm. Vertical error bars denote statistical errors only and do not represent systematic uncertainties, notably uncertainties in E_{app} and in the power law of E_{dip}. Inset: A typical plot of frequency vs voltage before (circles) and after (squares) one condensate has deposited on Ti ($\nu_0=216.5$ Hz). There is a measurable effect from the adsorption of just one condensate. The lines are weighted fits to extract the frequency shift per applied voltage. From McGuirk *et al.*, 2004.

McGuirk *et al.* (2004) also proposed the systematic deposition of adsorbates in order to generate potential structures on the surface. Alternatively, this work showed that ultracold atoms confined in a harmonic trap can be used to sensitively detect electrostatic forces.

2. Fragmentation

Microtraps realized by current carrying wires exhibit magnetic potential corrugations which can be traced to imperfections of the conductor geometry. Fluctuations of the wire shape, position, and impurities cause local deviations of the current flow from the ideal linear current path within the conductor. Resulting distortions of the current distort the magnetic trapping field. The spatial distribution of magnetically trapped atoms measures sensitively the field profile along the conductor. Especially, the field component along the axial offset field B_{off}, which is in general parallel to the conductor. This component modulates the potential minimum. It has been observed in numerous experiments that ultracold atomic clouds that are brought sufficiently close to a current carrying conductor break up into fragments (Fortágh, Ott, Kraft, *et al.*, 2002; Kraft *et al.*, 2002; Leanhardt, Chikkatur, *et al.*, 2002; Jones, Vale, Sahagun, Hall, and Hinds, 2003; Leanhardt, Shin, *et al.*, 2003; Estève *et al.*, 2004; Vale *et al.*, 2004; Wildermuth, Hofferberth, Lesanovsky, Groth, *et al.*, 2005; Wildermuth, Hofferberth, Lesanovsky, Haller, *et al.*, 2005).

Fragmentation was observed very soon after achieving Bose-Einstein condensation in microtraps. First experimental data characterizing the potential roughness were taken with thermal clouds expanding in waveguide potentials at close distances to current carrying wires (Fortágh, Ott, Kraft, *et al.*, 2002). Clouds of ^{87}Rb atoms ($N \sim 10^6$) at a temperature of 1 μK were initially prepared in the microtrap at different distances d to an electroplated conductor (30 μm width, 2.5 μm height, and 25 mm length). Subsequently, axial confinement was turned off within 400 ms and the cloud was allowed to expand axially in a waveguide, generated by the magnetic field of the wire, a homogeneous bias field perpendicular to the wire, and a homogeneous axial offset field. This configuration allowed undisturbed propagation at distances further than $d=300$ μm from the wire. At smaller distances, however, the atomic density distribution became modulated, demonstrating that the waveguide potential exhibits a significant waviness (Fig. 59). The potential modulation appeared to be almost periodic with approximately 250–300 μm spacing between minima. Bose-Einstein condensates were used to resolve further potential structures with a spacing of 110 μm at $d=100$ μm and 50 μm at $d=50$ μm. The potential minima were stationary in time and the observed spacing of minima was similar for seven conductors of different widths (3–30 μm) on the same chip. Qualitatively similar results were obtained for the axial density modulations and distance scaling behavior above a straight cylindrical copper wire of 90 μm diameter (Fortágh, Ott, Kraft, *et al.*, 2002; Kraft *et al.*, 2002; Fortágh *et al.*, 2003) and on electroplated conductors of 50 μm width and 10 μm height (Leanhardt, Chikkatur, *et al.*, 2002), producing a quasiperiodic distribution of potential minima with a spacing of 100–150 μm at $d=55$ μm.

The origin of fragmentation being a spatially altering magnetic field component was proven by Kraft *et al.* (2002). In expansion experiments as shown in Fig. 59, potential minima and maxima were interchanged when the offset field B_{off} was inverted. This is a unique signature for an axial magnetic field modulation B_{mod}, which is due to the fact that the magnetic trapping potential arises from the absolute value of the total field $|\pm B_{\mathrm{off}} + B_{\mathrm{mod}}(z)|$. Any other potential modulation (electrostatic or gravitational) would not be sensitive to the orientation of the offset field B_{off}. This result was confirmed by Leanhardt, Shin, *et al.* (2003), by holding a condensate in an optical dipole trap and an offset field B_{off}, at a close distance to a wire: Fragmentation appeared only when current was applied to the conductor. The magnitude of the spatially varying axial field component $|B_{\mathrm{mod}}|$ was measured by Kraft *et al.* (2002) and Jones, Vale, Sahagun, Hall, Eberlein, *et al.* (2003). Kraft *et al.* (2002) positioned condensates above a maximum of the altering field by shifting the position of the trap center and measured the chemical potential when the condensate was split into two parts. For $I=0,9$ A in a cylindrical wire (90 μm diameter) and 109 μm distance to the center of the conductor (16.5 G bias field), the axial field component was measured to be 3.7 mG, which was about three orders of magnitude smaller than the regular azimuthal field of the wire. It has been shown that the decay of $|B_{\mathrm{mod}}|$ over the distance from the wire is, in the range of 80–110 μm, well approximated by an exponential decay. Jones, Vale, Sahagun, Hall, Eberlein, *et al.* (2003) derived $|B_{\mathrm{mod}}|$ from the thermal distribution of atoms in an elongated trap. The axial distribution $\rho(z)$ of a thermal

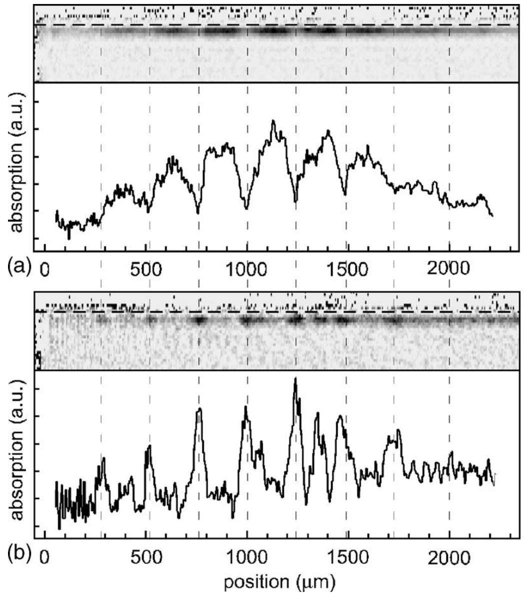

FIG. 59. Fragmentation of an ultracold cloud of ^{87}Rb atoms in a magnetic waveguide potential of an electroplated conductor (30 μm width, 2.5 μm height, and 25 mm length). The conductor is indicated by the horizontal dashed line. (a) The atoms were prepared in a waveguide by ramping down the axial confinement of the magnetic trap within 400 ms. The current in the microfabricated conductor was 0.045 A. With a bias field of $B_{\mathrm{bias}}=2$ G, the waveguide is formed at a distance of 45 μm from the surface. The offset field B_{off} parallel to the conductor was 1.3 G. The vertical dashed lines mark the position of the potential maxima. In (b) the atoms were initially prepared in the same trap as in (a). Next, the orientation of the offset field was flipped within 1 ms. Further 50 ms later, the atoms were located at the positions of previous potential maxima. The position of the potential minima changed with the direction of the offset which proves that the axial potential modulation is due to an axial magnetic field modulation. From Kraft *et al.*, 2002.

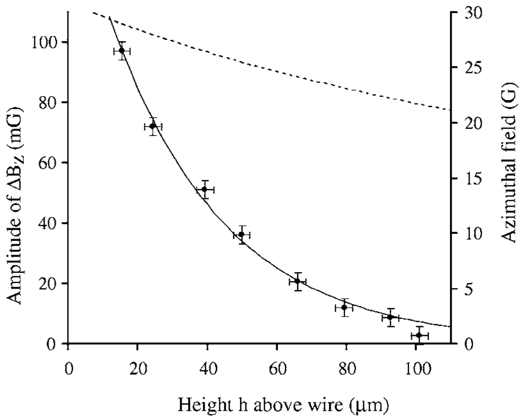

FIG. 60. Magnetic fields vs height h above the conductor surface ($h=y-\delta$, with the radius of the conductor $\delta=250\ \mu\text{m}$) above a wire carrying 3.7 A. Data points, amplitude of the anomalous magnetic field variation ΔB_z (B_{mod} in the text). Solid curve, best fit of the modified Bessel function $aK_1[2\pi(h+\delta)]/\lambda$, in which a, δ, and λ were allowed to vary freely as fitting parameters. This has $\lambda=217\pm 10\ \mu\text{m}$ and $\delta=251\pm 12\ \mu\text{m}$. Dashed curve, the (usual) azimuthal field referred to the auxiliary ordinate on the right. From Jones, Vale, Sahagun, Hall, Eberlein, *et al.*, 2003.

cloud is related to the confining potential $U(z)=\mu|\pm B_{\text{off}}(z)+B_{\text{mod}}(z)|$ by the Boltzmann factor $\rho(z)\propto e-U(z)/k_BT$. Here the axial offset field $B_{\text{off}}(z)$ had a curvature corresponding to an axial confinement of 26–27 Hz oscillation frequency. The axial density distribution was measured for eight different distances, in the range of 257–347 μm to the center of a wire ($\delta=250\ \mu\text{m}$ radius) carrying a current of 3.7–5 A, and with a constant bias field of 29 G. Fragmentation was observed with a characteristic period of $2\pi/k=230\ \mu\text{m}$. The temperature of the cloud (5.8–7.8 μK) was measured for each data set by fitting a parabola to $-\ln \rho(z)$. The value of $\mu B_{\text{mod}}(z)/k_BT$, and hence the amplitude of $B_{\text{mod}}(z)$, was derived from the difference between $-\ln \rho(z)$ and the harmonic fit. The scaling of $B_{\text{mod}}(z)\propto I$ (Kraft *et al.*, 2002) was used to normalize $B_{\text{mod}}(z)$, taken at different distances and currents, to a current of 3.7 A. The decay of the magnetic field component $B_{\text{mod}}(z)$ over the distance y to the wire center has been found to fit well with the modified Bessel function of second kind $K_1(ky)\propto \exp(-ky)/\sqrt{ky}$ (Fig. 60). The observation is thus consistent with helical or a horizontally meandering current paths along the conductor.

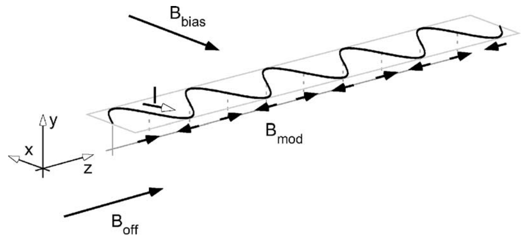

FIG. 61. Horizontally meandering current path and axial field modulation $B_{\text{off}}+B_{\text{mod}}$.

It is instructive to analyze the waveguide potential below a meandering current path as shown in Fig. 61. In a homogeneous bias field B_{bias}, the waveguide center follows an elliptical helix: while the horizontal position of the waveguide follows the horizontal excursion of the current, the vertical position is shifted up and down where the z component of the current rises and decreases, respectively. The most significant effect is, however, the axial potential modulation due to the magnetic field component parallel to the conductor. For a current of 1 A, a horizontal excursion of 50 nm (sine amplitude), and a meander wavelength of 220 μm, the amplitude of the axially altering magnetic field at a distance of $d=100\ \mu\text{m}$ ($B_{\text{bias}}=20$ G) to the conductor is $B_{\text{mod}}=4$ mG. The axial offset field B_{off} is periodically increased and decreased by this value. For ^{87}Rb atoms in the $|F=2,m_F=2\rangle$ hyperfine ground state, the corresponding modulation depth is $k_BT=2\mu_BB_{\text{mod}}=k_B\times 540$ nK. The horizontal position changes by ±50 nm and the vertical by ±50 pm only. Both are negligible for fragmentation.

A microscopic calculation given by Wang *et al.* (2004) explains the magnetic field roughness above a wire with random shape and position fluctuations of the wire. It is shown that, even when the wire fluctuations have no intrinsic length scale, the disordered magnetic potential in the waveguide is a Gaussian correlated random potential with a correlation function that is strongly peaked at a finite wave vector and vanishes for small and large wave vectors. The characteristic length scale is set by the atom-wire distance d. Starting from deviations of the wire's left/right boundaries from their ideal positions, Wang *et al.* (2004) derived that the leading order random potential $\delta U(d,0,z)$ comes from the axial component of the magnetic field $\delta B(d,0,z)$. To this order, only position fluctuations of the wire contribute (meandering of the center line of current flow). The correlation function of the fluctuating part of the potential

$$\Delta_k(d)=\int dz e^{ik(z-z')}\langle \delta U(d,0,z)\delta U(d,0,z')\rangle$$

is calculated which describes the appearance of characteristic periods at different distances to the wire and the scaling of the potential with the Bessel function. The theoretical model quantitatively explains experimental data; the decrease of the characteristic period of the fragments for smaller atom-wire separations and the distance scaling of the potential depth with the Bessel function.

In Fig. 62 the correlation function $\Delta_k(d)$ is plotted for white noise fluctuations of the wire center position. It peaks at $k_0\approx 1.3/d$ and vanishes at $k=0$ and $k=\infty$, showing a characteristic length scale d. Long-wavelength fluctuations are suppressed because a uniform shift of the random potential does not lead to a parallel z component of the magnetic field. In the inset in Fig. 62 it is demonstrated how the random magnetic potential is modified when wire fluctuations have an intrinsic length scale $1/k_1$. When wire fluctuations are short ranged

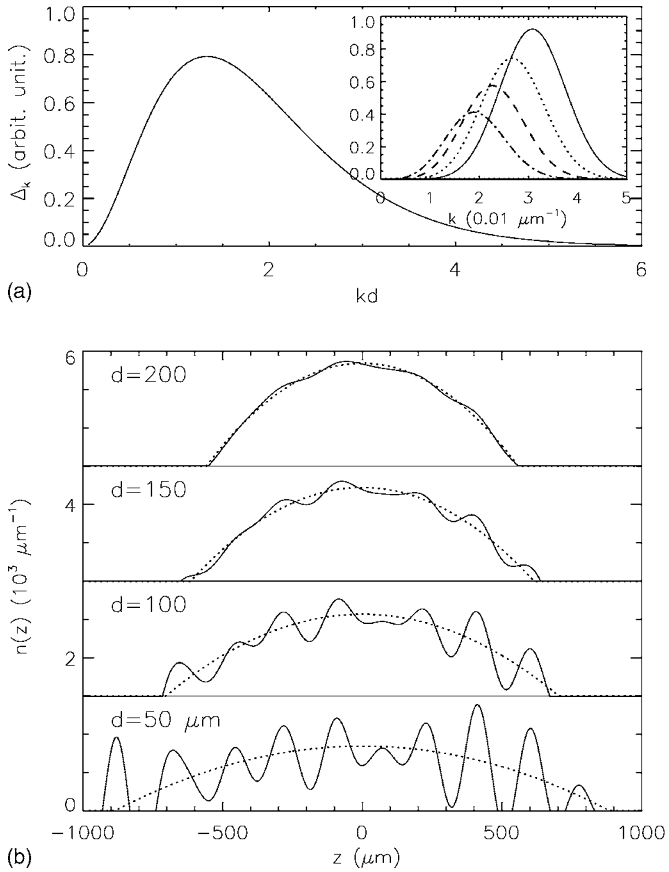

FIG. 62. Correlation function of random magnetic potentials and calculated condensate density profiles. (a) Correlation functions of the random magnetic potential in a microtrap Δ_k, assuming white noise fluctuations of the wire position. Inset, Δ_k when the wire fluctuations have an intrinsic length scale: $F_k \propto (e^{-(k-k1)^2\eta_1^2}+e^{-(k+k1)^2\eta_1^2})$. Here $2\pi/k_1=200\ \mu\text{m}$, $\eta_1=100\ \mu\text{m}$, and the disorder average over the wire position fluctuations f^+ is $\langle f^+(z)f^+(z)\rangle_{\text{dis}}=(0.1\ \mu\text{m})^2$. Solid to dash-dotted lines correspond to $d=50$, 100, 150, and 200 μm, respectively. (b) Condensate density profiles with parameters chosen to be close to the values used in the experiments of Leanhardt, Chikkatur, *et al.* (2002); Leanhardt, Shin, *et al.* (2003). Dotted lines are the results without random potential. From Wang *et al.*, 2004.

$(k_1 d \gg 1)$, the potential fluctuations remain peaked close to $k_0 \sim 1.3/d$ and the length scale of the random potential is set by the atom-wire separation. When wire fluctuations are longer ranged $(k_1 d < 1)$, k is then peaked at $k \sim k_1$ and the random potential tracks wire fluctuations. A linear relation between the condensate height and the length scale of the fragmentation was observed by Fortágh, Ott, Kraft, *et al.* (2002) and Leanhardt, Chikkatur, *et al.* (2002). Figure 62(b) shows the calculated condensate density profiles for 10^6 sodium atoms in the Thomas-Fermi approximation using wire fluctuations taken from the distributions of the inset in Fig. 62(a). The fragmentation appears for $d \leq 100\ \mu$m; cf. Leanhardt, Chikkatur, *et al.* (2002). It is noted that the profiles obtained by a white noise potential [i.e., $\Delta_k(d)=\text{const}$] do not have a characteristic length scale and are very different from the above results and experiments.

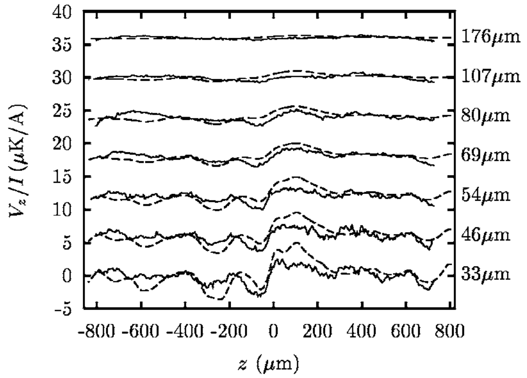

FIG. 63. Rough potentials normalized to the current in the wire for different heights from the wire. Solid lines, potentials measured using cold atomic clouds. Dashed lines, potentials calculated from the measured geometric roughness of the edges of the wire. The different curves have been shifted by 6 μK/A for clarity. From Estève *et al.*, 2004.

In a quantitative experimental study, Estève *et al.* (2004) proved that the magnetic field roughness observed in microtraps is due to geometric imperfections of the conductor. Measurements of the potential corrugation using cold trapped atoms have been compared with the potential computed from the measurement of the wire edge roughness which was measured with a scanning electron microscope. The leading order of the potential roughness above the electroplated conductor (50 μm width, 4.5 μm thickness) could be explained by edge fluctuations of the wire. The potential roughness was measured with atoms at different distance to the wire with a temperature chosen on the same order as the potential variations ($T \cong 0.4\ \mu$K for 170 μm and $T \cong 2.2\ \mu$K for 33 μm from the wire). The longitudinal potential variation was derived from the axial density distribution of atoms in the trap, similar to Jones, Vale, Sahagun, Hall, *et al.* (2003). In Fig. 63 the varying part of the potential is plotted after subtraction of the harmonic confinement and normalization to a constant current of 1 A (solid lines). The scanning tunneling microscope (SEM) image of the same conductor (Fig. 21) shows edge fluctuations with characteristic length scales of about 100 nm and also 60–1000 μm. Axial magnetic field components arising from displacements of the center line of the conductor have been calculated based on wire edge fluctuations (Wang *et al.*, 2004). The calculated potential (dashed line in Fig. 63) not only gives spectra that are consistent with the potential deduced from the atomic density but also spatial profiles that correlate very well with the experimental results.

Fluctuations of the wire geometry are related to the fabrication of the wire. They are significantly smaller, for example, in evaporated conductors than in electroplated conductors (Figs. 20 and 21 vs Fig. 22). For a given fabrication technology edge fluctuations are expected to be independent of the wire width W_0. Thus assuming a white noise spectrum, the normalized potential roughness U_{rms}/I varies as $1/W_0^{5/2}$ for fixed ratio d/W_0, d being the distance to the wire (Wang *et al.*, 2004; Schumm, Estève, *et al.*, 2005a). For $d \ll W_0$, variations of the conductor thickness and inhomogeneities of the material gain influence. Related measurements have been done with quasi-one-dimensional condensates at close distances ($\sim$10 μm) to the surface of a current carrying wire of 100 μm width (Wildermuth, Hofferberth, Lesanovsky, Haller, *et al.*, 2005). The density distribution of the cloud was imaged directly in the trap. Data taken at different lateral positions were used to reconstruct the two-dimensional magnetic field profile (magnetic landscape) above the wire which is related to current distribution in the wire.

A possible way to reduce potential roughness in a microtrap may be the splitting of conductors into parallel segments such that fluctuations of the magnetic field of each average out. Another way using time-orbiting potentials has been proposed by Kraft *et al.* (2002). On the other hand, the experiments described above demonstrate that ultracold paramagnetic atoms confined in magnetic traps are suitable for direction sensitive magnetic field measurements and are capable of resolving potential energies on the order of the thermal energy ($\mu|B| \approx k_B T$) and the chemical potential ($\mu|B| \approx \mu_{\mathrm{chem}}$). Moreover, disordered potentials as observed in microtraps above fabricated current conductors are discussed as promising environment for studying quantum dynamics in disordered systems.

VI. PERSPECTIVES

The field of magnetic microtraps has rapidly grown during the last five years, mainly triggered by the successful generation of Bose-Einstein condensates in microtraps in 2001. Since then, many of the basic questions have been worked out. Reliable techniques for loading atoms into microtraps are available, and today Bose-Einstein condensates, degenerate Fermi gases, and their mixtures are routinely studied in microtraps throughout the world. The interaction of atoms with chip surfaces has been investigated, and the limits of trapping and manipulating atoms in microtraps can now be estimated more accurately. The field has also benefited from a rapid development of technology. Methods have been demonstrated for miniaturizing the complete experimental apparatus (Du *et al.*, 2004), and it is feasible to construct portable, battery-powered, microchip-based devices. A variety of additional on-chip elements that go beyond simple magnetic guiding have been proposed and demonstrated, nourishing the vision of an on-chip laboratory for atomic quantum systems. This includes complex microfabricated trapping geometries (Grabowski and Pfau, 2003; Günther, Kemmler, Kraft, *et al.*, 2005), the integration of various field generating elements on the chip such as permanent magnets (Barb *et al.*, 2005; Sinclair *et al.*, 2005; Ghanbari *et al.*, 2006; Hall *et al.*, 2006), electrodes for applying electrostatic forces (Krüger *et al.*, 2003; Shevchenko *et al.*, 2004), optical fields (Barnett *et al.*, 2000; Cornelussen *et al.*, 2002; Hammes *et al.*, 2003; Shin, Saba, Pasquini, *et al.*, 2004; Shin, Saba, Schirotzek, *et al.*, 2004; Shin, Jan, *et al.*, 2005; Wang *et al.*, 2005), and optical microtraps based on microlenses (Brikl *et al.*, 2001; Dumke *et al.*, 2002). Proposals for hybrid quantum systems which combine ultracold atoms with superconductors, have been put forward by Hyafil *et al.* (2004), Sorensen *et al.* (2004), Henkel (2005), and Scheel *et al.* (2005). In view of this impressive inventory of methods and techniques one may speculate that the field of magnetic microtraps described in this article will rapidly develop into a new quantum technology of chip-based "microatomics."

For future research, three main topics can be identified. The interaction between atoms and the chip surface has already been studied to some extent. The principles of operation of novel types of magnetic field microscopes can be derived from experiments where ultracold clouds show fragmentation in the vicinity of the surface (Fortágh, Ott, Kraft, *et al.*, 2002a; Kraft *et al.*, 2002; Leanhardt, Chikkatur, *et al.*, 2002; Jones, Vale, Sahagun, Hall, Eberlein, *et al.*, 2003; Wildermuth, Hofferberth, Lesanovsky, Haller, *et al.*, 2005) and alternatively by nanopositioning condensates with conveyor belts: tiny deviations from the expected position (Günther, Kemmler, Kraft, *et al.*, 2005) or the lifetime of the cloud (Lin *et al.*, 2004) provides information about surface forces. Furthermore, by monitoring the atomic oscillation frequency inside the trap, electrostatic (McGuirk *et al.*, 2004) and dispersion forces (Harber *et al.*, 2005) can be measured with extreme precision. Besides these first realizations of surface microscopes, even sensitive measurements of hypothetical short-range correction to, e.g., gravitational forces have been proposed (Dimopoulos and Geraci, 2003). One can even envisage ultracold chemistry on a chip where reactions are controlled by incident matter waves (Jorgensen and Kosloff, 2003, 2004).

A second topic involves single-atom physics on a chip. It is conceivable to use Bose-Einstein condensates or Fermi gases as reservoirs and coherent sources for atoms (Fortágh *et al.*, 2004). Atoms extracted on demand (Mohring *et al.*, 2005) can be guided and coherently manipulated by means of various integrated elements on the chip. One can even think about controlled entanglement of strings of atoms using Y junctions on a microchip (Dorner *et al.*, 2003). These scenarios may turn out to be promising candidates for integrated quantum information processing in the not so far future (Jaksch *et al.*, 1999, 2000; Calarco *et al.*, 2000; Schmiedmayer *et al.*, 2002; Griessner *et al.*, 2005). Such experiments will most likely require suitable schemes for detecting single atoms (Mabuchi *et al.*, 1996; Münstermann *et al.*, 1999; Öttl *et al.*, 2005). The realization of on-chip single-atom detectors is thus subject of current research (Horak *et al.*, 2003; Long *et al.*, 2003; Lev *et al.*, 2004; Ericson *et al.*, 2005; Trupke *et al.*, 2005; Haase *et al.*, 2006). First experimental success has been reported by Teper *et al.* (2006). Furthermore, exciting physics may be expected if Rydberg atoms can be manipulated and trapped in magnetic waveguide potentials (Lesanovsky *et al.*, 2004, 2005a).

Finally, microtraps offer intriguing perspectives for the investigation of quantum gases in various model potentials, such as periodic potentials, waveguide potentials with strong radial confinement, disordered potentials, and other more complex geometries. First examples of matter-wave interference with Bose-Einstein condensates in microtraps have been treated in Sec. IV.C. These experiments could be the starting point for constructing interferometric sensor chips for forces, accelerations, and rotations. Besides such applications, strongly anisotropic microtraps may offer a fruitful laboratory for studying fundamental physics of one-dimensional quantum gases. One-dimensional traps have been realized in optical lattice potentials [see, e.g., Greiner *et al.* (2001), Henning *et al.* (2003), Kinoshita *et al.* (2004)]; however, elongated microtrap potentials hold promise for a continuous transformation from 3D to 1D with access to the dimensional crossover (Das, 2002; Gerbier, 2004). Under 1D conditions, the atom-atom interaction becomes increasingly important for small densities and the Tonks-Girardeau regime may be entered where atoms are strongly correlated (Kinoshita *et al.*, 2004, 2005; Paredes *et al.*, 2004; Reichel and Thywissen, 2004). A complete 1D Mach-Zehnder-type interferometer with optical couplers has been proposed by Girardeau *et al.* (2002). Here, the interacting 1D Bose gas is mapped to a noninteracting 1D Fermi gas (boson-fermion duality in 1D). The loss of coherence due to atomic interaction has been studied by Chen and Egger (2003) in the Tonks-Girardeau regime and in the 1D Thomas-Fermi limit at higher densities. Other proposed topics which exploit the specific properties of microtraps include the existence of long-range order in 1D (Fischer, 2002), the sonic analogy of Hawking radiation (Giovanazzi *et al.*, 2004), nonlinear transport of condensates through a quantum dot (Paul, Ritcher, and Schlagheck, 2005) and through waveguides with disorder (Paul, Leboeuf, *et al.*, 2005), solitons in 1D (Schumayer and Apagyi, 2004), Thomas-Fermi Tonks-Giradeau crossover (Dunjko *et al.*, 2001), Tonks-Giradeau gas in a ring trap (Das, Girardeau, and Wright, 2002), degenerate Fermi gases in 1D (Wonneberger, 2001; Xu *et al.*, 2001; Xianlong and Wonneberger, 2002, 2004; Xianlong *et al.*, 2003; Artemenko *et al.*, 2004), and Fermi-Bose mixtures in 1D (Das, 2003).

This sampling of possible topics already shows the fascinating perspectives for microtraps in basic research as well as for applications. It will be exciting to watch the progress of the field during the next decade.

ACKNOWLEDGMENTS

The authors thank Andreas Günther, Matt Jones, Stefan Scheel, and Chris Vale for helpful comments on the manuscript. Financial support from the Deutsche Forschungsgemeinschaft, Landesstiftung Baden-Württemberg, and European Union is gratefully acknowledged.

REFERENCES

Adams, C. S., M. Sigel, and J. Mlynek, 1994, "Atom optics," Phys. Rep. **240**, 143–210.

Agarwal, G. S., 1975, "Quantum electrodynamics in the presence of dielectrics and conductors. I. Electromagnetic-field response functions and black-body fluctuations in finite geometries," Phys. Rev. A **11**, 230–242.

Anderson, B. P., and M. A. Kasevich, 2001, "Loading a vapor-cell magneto-optic trap using light-induced atom desorption," Phys. Rev. A **63**, 023404.

Andersson, E., T. Calarco, R. Folman, M. Andersson, B. Hessmo, and J. Schmiedmayer, 2002, "Multimode interferometer for guided matter waves," Phys. Rev. Lett. **88**, 100401.

Antezza, M., L. P. Pitaevskii, and S. Stringari, 2005, "New asymptotic behavior of the surface-atom force out of thermal equilibrium," Phys. Rev. Lett. **95**, 113202.

Artemenko, S. N., G. Xianlong, and W. Wonneberger, 2004, "Friedel oscillations in a gas of interacting one-dimensional fermionic atoms confined in a harmonic trap," J. Phys. B **37**, S49–S58.

Atutov, S. N., R. Calabrese, V. Guidi, B. Mai, A. G. Rudavets, E. Scansani, L. Tomassetti, V. Biancalana, A. Burchianti, C. Marinelli, E. Mariotti, L. Moi, and S. Veronesi, 2003, "Fast and efficient loading of a Rb magneto-optical trap using light-induced atomic desorption," Phys. Rev. A **67**, 053401.

Aubin, S., S. Myrskog, M. H. T. Extavour, L. J. LeBlanc, D. McKay, A. Stummer, and J. H. Thywissen, 2006, "Rapid sympathetic cooling to Fermi degeneracy on a chip," Nat. Phys. **2**, 384–387.

Barb, I., R. Gerritsma, Y. T. Xing, J. B. Goedkoop, and R. J. C. Spreeuw, 2005, "Creating Ioffe-Pritchard micro-traps from permanent magnetic film with in-plane polarization," Eur. Phys. J. D **35**, 75–79.

Barnett, A. H., S. P. Smith, M. Olshanii, K. S. Johnson, A. W. Adams, and M. Prentiss, 2000, "Substrate-based atom waveguide using guided two-color evanescent light fields," Phys. Rev. A **61**, 023608.

Berman, P., 1997, *Atom Interferometry* (Academic, London).

Birkl, G., F. B. J. Buchkremer, R. Dumke, and W. Ertmer, 2001, "Atom optics with microfabricated optical elements," Opt. Commun. **191**, 67–81.

Bloch, I., M. Köhl, M. Greiner, T. W. Hänsch, and T. Esslinger, 2001, "Optics with an atom laser beam," Phys. Rev. Lett. **87**, 030401.

Blumel, R., and K. Dietrich, 1991, "Quantum states of neutrons bound in the magnetic field of a rectilinear current," Phys. Rev. A **43**, 22–28.

Boesten, H. M. J. M., A. J. Moerdijk, and B. J. Verhaar, 1996, "Dipolar decay in two recent Bose-Einstein condensation experiments," Phys. Rev. A **54**, R29–R32.

Bongs, K., and K. Sengstock, 2004, "Physics with coherent matter waves," Rep. Prog. Phys. **67**, 907–963.

Bortolotti, D. C. E., and J. L. Bohn, 2004, "Wave mechanics of a two-wire atomic beam splitter," Phys. Rev. A **69**, 033607.

Bromley, M. W. J., and B. D. Esry, 2003, "Propagation of ultracold atoms through bends in waveguides," Phys. Rev. A **68**, 043609.

Bromley, M. W. J., and B. D. Esry, 2004, "Classical aspects of ultracold atom wave packet motion through microstructured waveguide bends," Phys. Rev. A **69**, 053620.

Buhmann, S. Y., T. D. Ho, and D.-G. Welsch, 2004, "The van der Waals energy of atomic systems near absorbing and dispersing bodies," J. Opt. B: Quantum Semiclassical Opt. **6**, S127–S135.

Buhmann, S. Y., L. Knöll, and D.-G. Welsch, 2004, "Casimir-Polder forces: A nonperturbative approach," Phys. Rev. A **70**, 052117.

Burt, E. A., R. W. Ghrist, C. J. Myatt, M. J. Holland, E. A. Cornell, and C. E. Wieman, 1997, "Coherence, correlations, and collisions: What one learns about Bose-Einstein condensates from their decay," Phys. Rev. Lett. **79**, 337–340.

Calarco, T., E. A. Hinds, D. Jaksch, J. Schmiedmayer, J. I. Cirac, and P. Zoller, 2000, "Quantum gates with neutral atoms: Controlling collisional interactions in time-dependent traps," Phys. Rev. A **61**, 022304.

Casimir, H. B. G., and D. Polder, 1948, "The influence of retardation on the London-van der Waals forces," Phys. Rev. **73**, 360–372.

Cassettari, D., A. Chenet, R. Folman, A. Haase, B. Hessmo, P. Krüger, T. Maier, S. Schneider, T. Calarco, and J. Schmiedmayer, 2000, "Micromanipulation of neutral atoms with nanofabricated structures," Appl. Phys. B: Lasers Opt. **70**, 721–730.

Cassettari, D., B. Hessmo, R. Folman, T. Maier, and J. Schmiedmayer, 2000, "Beam splitter for guided atoms," Phys. Rev. Lett. **85**, 5483–5487.

Chen, S., and R. Egger, 2003, "Destruction of interference by many-body interactions in cold atomic Bose gases," Phys. Rev. A **68**, 063605.

Colombe, Y., E. Knyazchyan, O. Morizot, B. Mercier, V. Lorent, and H. Perrin, 2004, "Ultracold atoms confined in rf-induced two-dimensional trapping potentials," Europhys. Lett. **67**, 593–599.

Cornell, E. A., C. Monroe, and C. E. Wieman, 1991, "Multiply loaded, ac magnetic trap for neutral atoms," Phys. Rev. Lett. **67**, 2439–2442.

Cornell, E. A., and C. E. Wieman, 2002, "Nobel Lecture: Bose-Einstein condensation in a dilute gas, the first 70 years and some recent experiments," Rev. Mod. Phys. **74**, 875–893.

Cornelussen, R. A., A. H. van Amerongen, B. T. Wolschrijn, R. J. C. Spreeuw, and H. B. van Linden van den Heuvell, 2002, "Cold trapped atoms detected with evanescent waves," Eur. Phys. J. D **21**, 347–351.

Courteille, P. W., B. Deh, J. Fortágh, A. Günther, S. Kraft, C. Marzok, S. Slama, and C. Zimmermann, 2006, "Highly versatile atomic microtraps generated by multifrequency magnetic field modulation," J. Phys. B **39**, 1055–1064.

Dalfovo, F., S. Giorgini, L. P. Pitaevskii, and S. Stringari, 1999, "Theory of Bose-Einstein condensation in trapped gases," Rev. Mod. Phys. **71**, 463–512.

Das, K. K., 2002, "Highly anisotropic Bose-Einstein condensates: Crossover to lower dimensionality," Phys. Rev. A **66**, 053612.

Das, K. K., 2003, "Bose-Fermi mixtures in one dimension," Phys. Rev. Lett. **90**, 170403.

Das, K. K., M. D. Girardeau, and E. M. Wright, 2002, "Interference of a thermal Tonks gas on a ring," Phys. Rev. Lett. **89**, 170404.

Davis, T. J., 2002, "2D magnetic traps for ultra-cold atoms: a simple theory using complex numbers," Eur. Phys. J. D **18**, 27–36.

Dekker, N. H., C. S. Lee, V. Lorent, J. H. Thywissen, S. P. Smith, M. Drndic, R. M. Westervelt, and M. Prentiss, 2000, "Guiding neutral atoms on a chip," Phys. Rev. Lett. **84**, 1124–1127.

Denschlag, J., D. Cassettari, A. Chenet, S. Schneider, and J. Schmiedmayer, 1999, "A neutral atom and a wire: towards mesoscopic atom optics," Appl. Phys. B: Lasers Opt. **69**, 291–301.

Denschlag, J., D. Cassettari, and J. Schmiedmayer, 1999, "Guiding neutral atoms with a wire," Phys. Rev. Lett. **82**, 2014–2017.

Dimopoulos, S., and A. A. Geraci, 2003, "Probing submicron forces by interferometry of Bose-Einstein condensed atoms," Phys. Rev. D **68**, 124021.

Dorner, U., P. Fedichev, D. Jaksch, M. Lewenstein, and P. Zoller, 2003, "Entangling strings of neutral atoms in 1D atomic pipeline structures," Phys. Rev. Lett. **91**, 073601.

Dowling, J. P., and J. Gea-Banacloche, 1996, Adv. At., Mol., Opt. Phys. **37**, 1.

Drndic, M., K. S. Johnson, J. H. Thywissen, M. Prentiss, and R. M. Westervelt, 1998, "Micro-electromagnets for atom manipulation," Appl. Phys. Lett. **72**, 2906–2908.

Drndic, M., G. Zabow, C. S. Lee, J. H. Thywissen, K. S. Johnson, M. Prentiss, R. M. Westervelt, P. D. Featonby, V. Savalli, L. Cognet, K. Helmerson, N. Westbrook, C. I. Westbrook, W. D. Phillips, and A. Aspect, 1999, "Properties of microelectromagnet mirrors as reflectors of cold Rb atoms," Phys. Rev. A **60**, 4012–4015.

Du, S., M. B. Squires, L. Czaia, R. A. Saravanan, V. M. Bright, Y. Imai, J. Reichel, T. W. Hänsch, and D. Z. Anderson, 2004, "Atom chip Bose-Einstein condensation in a portable vacuum cell," Phys. Rev. A **70**, 053606.

Dumke, R., M. Volk, T. Müther, F. B. J. Buchkremer, G. Birkl, and W. Ertmer, 2002, "Micro-optical realization of arrays of selectively addressable dipole traps: A scalable configuration for quantum computation with atomic qubits," Phys. Rev. Lett. **89**, 097903.

Dunjko, V., V. Lorent, and M. Olshanii, 2001, "Bosons in cigar-shaped traps: Thomas-Fermi regime, Tonks-Girardeau regime, and in between," Phys. Rev. Lett. **86**, 5413–5416.

Ericson, S., M. Trupke, H. F. Powell, D. Sahagun, C. D. J. Sinclair, E. A. Curtis, B. E. Sauer, E. A. Hinds, Z. Moktadir, C. O. Gollasch, and M. Kraft, 2005, "Integrated optical components on atom chips," Eur. Phys. J. D **35**, 135–139.

Esry, B. D., C. H. Greene, and J. P. Burke, Jr., 1999, "Recombination of three atoms in the ultracold limit," Phys. Rev. Lett. **83**, 1751–1754.

Estéve, J., C. Aussibal, T. Schumm, C. Figl, D. Mailly, I. Bouchoule, C. I. Westbrook, and A. Aspect, 2004, "Role of wire imperfections in micromagnetic traps for atoms," Phys. Rev. A **70**, 043629.

Estève, J., T. Schumm, J.-B. Trebbia, I. Bouchoule, and A. Aspect, 2005, "Realizing a stable double-well potential on an atom chip," Eur. Phys. J. D **35**, 141–146.

Fedichev, P. O., M. W. Reynolds, and G. V. Shlyapnikov, 1996, "Three-body recombination of ultracold atoms to a weakly bound *s* level," Phys. Rev. Lett. **77**, 2921–2924.

Fermani, R., S. Scheel, and P. L. Knight, 2006, "Spatial decoherence near metallic surfaces," Phys. Rev. A **73**, 032902.

Fischer, U. R., 2002, "Existence of long-range order for trapped interacting bosons," Phys. Rev. Lett. **89**, 280402.

Folman, R., P. Krüger, D. Cassettari, B. Hessmo, T Maier, and J. Schmiedmayer, 2000, "Controlling cold atoms using nanofabricated surfaces: Atom chips," Phys. Rev. Lett. **84**, 4749–4752.

Folman, R., P. Krüger, J. Denschlag, C. Henkel, and J. Schmiedmayer, 2002, "Microscopic atom optics: From wires to an atom chip," Adv. At., Mol., Opt. Phys. **48**, 263–356.

Fortágh, J., A. Grossmann, T. W. Hänsch, and C. Zimmermann, 1998, "Fast loading of a magneto-optical trap from a pulsed thermal source," J. Appl. Phys. **84**, 6499–6501.

Fortágh, J., A. Grossmann, C. Zimmermann, and T. W. Hänsch, 1998, "Miniaturized wire trap for neutral atoms," Phys. Rev. Lett. **81**, 5310–5313.

Fortágh, J., S. Kraft, A. Günther, Ch. Trück, Ph. Wicke, and C. Zimmermann, 2004, "Perspectives of ultracold atoms trapped in magnetic micro potentials," Opt. Commun. **243**, 45–56.

Fortágh, J., H. Ott, A. Grossmann, and C. Zimmermann, 2000, "Miniaturized magnetic guide for neutral atoms," Appl. Phys. B: Lasers Opt. **70**, 701–708.

Fortágh, J., H. Ott, S. Kraft, A. Günther, and C. Zimmermann, 2002, "Surface effects in magnetic microtraps," Phys. Rev. A **66**, 041604.

Fortágh, J., H. Ott, S. Kraft, A. Günther, and C. Zimmermann, 2003, "Bose-Einstein condensates in magnetic waveguides," Appl. Phys. B: Lasers Opt. **76**, 157–163.

Fortágh, J., H. Ott, G. Schlotterbeck, C. Zimmermann, B. Herzog, and D. Wharam, 2002, "Microelectromagnets for trapping and manipulating ultracold atomic quantum gases," Appl. Phys. Lett. **81**, 1146–1148.

Frisch, R., and E. Segrè, 1933, Z. Phys. 610.

Gehm, M. E., K. M. O'Hara, T. A. Savard, and J. E. Thomas, 1998, "Dynamics of noise-induced heating in atom traps," Phys. Rev. A **58**, 3914–3921.

Gerbier, F., 2004, "Quasi-1D Bose-Einstein condensates in the dimensional crossover regime," Europhys. Lett. **66**, 771–777.

Ghanbari, S., T. D. Kieu, A. Sidorov, and P. Hannaford, 2006, "Permanent magnetic lattices for ultracold atoms and quantum degenerate gases," J. Phys. B **39**, 847–860.

Giovanazzi, S., C. Farrell, T. Kiss, and U. Leonhardt, 2004, "Conditions for one-dimensional supersonic flow of quantum gases," Phys. Rev. A **70**, 063602.

Girardeau, M. D., K. K. Das, and E. M. Wright, 2002, "Theory of a one-dimensional double-X- junction atom interferometer," Phys. Rev. A **66**, 023604.

Görlitz, A., J. M. Vogels, A. E. Leanhardt, C. Raman, T. L. Gustavson, J. R. bo-Shaeer, A. P. Chikkatur, S. Gupta, S. Inouye, T. Rosenband, and W. Ketterle, 2001, "Realization of Bose-Einstein condensates in lower dimensions," Phys. Rev. Lett. **87**, 130402.

Grabowski, A., and T. Pfau, 2003, "A lattice of magneto-optical and magnetic traps for cold atoms," Eur. Phys. J. D **22**, 347–354.

Greiner, M., I. Bloch, O. Mandel, T. W. Hänsch, and T. Esslinger, 2001, "Bose-Einstein condensates in 1D and 2D optical lattices," Appl. Phys. B: Lasers Opt. **73**, 769–772.

Griessner, A., A. J. Daley, D. Jaksch, and P. Zoller, 2005, "Fault-tolerant dissipative preparation of atomic quantum registers with fermions," Phys. Rev. A **72**, 032332.

Groth, S., P. Krüger, S. Wildermuth, R. Folman, T. Fernholz, J. Schmiedmayer, D. Mahalu, and I. Bar-Joseph, 2004, "Atom chips: Fabrication and thermal properties," Appl. Phys. Lett. **85**, 2980.

Günther, A., M. Kemmler, S. Kraft, C. J. Vale, C. Zimmermann, and J. Fortágh, 2005, "Combined chips for atom-optics," Phys. Rev. A **71**, 063619.

Günther, A., S. Kraft, M. Kemmler, D. Koelle, R. Kleiner, C. Zimmermann, and J. Fortágh, 2005, "Diffraction of a Bose-Einstein condensate from a magnetic lattice on a micro chip," Phys. Rev. Lett. **95**, 170405.

Günther, A., S. Kraft, C. Zimmermann, and J. Fortágh, 2006, "Atom interferometer based on phase coherent splitting of Bose-Einstein condensates with an integrated magnetic grating," e-print cond-mat/0603631.

Gustavson, T. L., A. P. Chikkatur, A. E. Leanhardt, A. Görlitz, S. Gupta, D. E. Pritchard, and W. Ketterle, 2002, "Transport of Bose-Einstein condensates with optical tweezers," Phys. Rev. Lett. **88**, 020401.

Haase, A., D. Cassettari, B. Hessmo, and J. Schmiedmayer, 2001, "Trapping neutral atoms with a wire," Phys. Rev. A **64**, 043405.

Haase, A., B. Hessmo, and J. Schmiedmayer, 2006, "Detecting magnetically guided atoms with an optical cavity," Opt. Lett. **31**, 268–270.

Hall, B. V., S. Whitlock, F. Scharnberg, P. Hannaford, and A. Sidorov, 2006, "A permanent magnetic film atom chip for Bose-Einstein condensation," J. Phys. B **39**, 27–36.

Hammes, M., D. Rychtarik, B. Engeser, H.-C. Nägerl, and R. Grimm, 2003, "Evanescent-wave trapping and evaporative cooling of an atomic gas at the crossover to two dimensions," Phys. Rev. Lett. **90**, 173001.

Hänsel, W., P. Hommelhoff, T. W. Hänsch, and J. Reichel, 2001, "Bose-Einstein condensation on a microelectronic chip," Nature (London) **413**, 498–501.

Hänsel, W., J. Reichel, P. Hommelhoff, and T. W. Hänsch, 2001a, "Trapped-atom interferometer in a magnetic microtrap," Phys. Rev. A **64**, 063607.

Hänsel, W., J. Reichel, P. Hommelhoff, and T. W. Hänsch, 2001b, "Magnetic conveyor belt for transporting and merging trapped atom clouds," Phys. Rev. Lett. **86**, 608–611.

Harber, D. M., J. M. McGuirk, J. M. Obrecht, and E. A. Cornell, 2003, "Thermally induced losses in ultra-cold atoms magnetically trapped near room-temperature surfaces," J. Low Temp. Phys. **133**, 229–238.

Harber, D. M., J. M. Obrecht, J. M. McGuirk, and E. A. Cornell, 2005, "Measurement of the Casimir-Polder force through center-of-mass oscillations of a Bose-Einstein condensate," Phys. Rev. A **72**, 033610.

Hau, L. V., J. A. Golovchenko, and M. M. Burns, 1995, "Supersymmetry and the binding of a magnetic atom to a filamentary current," Phys. Rev. Lett. **74**, 3138–3140.

Henkel, C., 2005, "Magnetostatic field noise near metallic surfaces," Eur. Phys. J. D **35**, 59–67.

Henkel, C., J.-Y. Courtois, and A. Aspect, 1994, "Atomic diffraction by a thin phase grating," J. Phys. II **4**, 1955–1974.

Henkel, C., P. Krüger, R. Folman, and J. Schmiedmayer, 2003, "Fundamental limits for coherent manipulation on atom chips," Appl. Phys. B: Lasers Opt. **76**, 173–182.

Henkel, C., and S. Pötting, 2001, "Coherent transport of matter waves," Appl. Phys. B: Lasers Opt. **72**, 73–80.

Henkel, C., S. Pötting, and M. Wilkens, 1999, "Loss and heating of particles in small and noisy traps," Appl. Phys. B: Lasers Opt. **69**, 379–387.

Henning, M., T. Stöferle, M. Köhl, and T. Esslinger, 2003, "Exciting collective oscillations in a trapped 1D gas," Phys. Rev. Lett. **91**, 250402.

Hess, H. F., 1986, "Evaporative cooling of magnetically trapped and compressed spin-polarized hydrogen," Phys. Rev. B **34**, 3476–3479.

Hess, H. F, G. P. Kochanski, J. M. Doyle, N. Masuhara, D. Kleppner, and T. J. Greytak, 1987, "Magnetic trapping of spin-polarized atomic hydrogen," Phys. Rev. Lett. **59**, 672–675.

Hijmans, T. W., O. J. Luiten, I. D. Setija, and J. T. M. Walraven, 1989, "Optical cooling of atomic hydrogen in a magnetic trap," J. Opt. Soc. Am. B **6**, 2235–2243.

Hinds, E. A., 1999, "Controlling cold atoms above a magnetic reflector," Philos. Trans. R. Soc. London, Ser. A **357**, 1409–1420.

Hinds, E. A., and C. Eberlein, 2000, "Quantum propagation of neutral atoms in a magnetic quadrupole guide," Phys. Rev. A **61**, 033614.

Hinds, E. A., and I. G. Hughes, 1999, "Magnetic atom optics: Mirrors, guides, traps, and chips for atoms," J. Phys. D **32**, R119–R146.

Hinds, E. A., C. J. Vale, and M. G. Boshier, 2001, "Two-wire waveguide and interferometer for cold atoms," Phys. Rev. Lett. **86**, 1462–1465.

Holmes, M. E., M. Tscherneck, P. A. Quinto-Su, and N. P. Bigelow, 2004, "Isotopic difference in the heteronuclear loss rate in a two-species surface trap," Phys. Rev. A **69**, 063408.

Hommelhoff, P., W. Hänsel, T. Steinmetz, T. W. Hänsch, and J. Reichel, 2005, "Transporting, splitting and merging of atomic ensembles in a chip trap," New J. Phys. **7**, 1–17.

Horak, P., B. G. Klappauf, A. Haase, R. Folman, J. Schmiedmayer, P. Domokos, and E. A. Hinds, 2003, "Possibility of single-atom detection on a chip," Phys. Rev. A **67**, 043806.

Hyafil, P., J. Mozley, A. Perrin, J. Tailleur, G. Nogues, M. Brune, J. M. Raimond, and S. Haroche, 2004, "Coherence-preserving trap architecture for long-term control of giant Rydberg atoms," Phys. Rev. Lett. **93**, 103001.

Jaaskelainen, M., and S. Stenholm, 2002a, "Reflection of matter waves in potential structures," Phys. Rev. A **66**, 053605.

Jaaskelainen, M., and S. Stenholm, 2002b, "Adiabatic propagation in potential structures," Phys. Rev. A **66**, 023608.

Jaaskelainen, M., and S. Stenholm, 2003, "Localization in splitting of matter waves," Phys. Rev. A **68**, 033607.

Jaksch, D., H.-J. Briegel, J. I. Cirac, C. W. Gardiner, and P. Zoller, 1999, "Entanglement of atoms via cold controlled collisions," Phys. Rev. Lett. **82**, 1975–1978.

Jaksch, D., J. I. Cirac, P. Zoller, S. L. Rolston, R. Cote, and M. D. Lukin, 2000, "Fast quantum gates for neutral atoms," Phys. Rev. Lett. **85**, 2208–2211.

Jo, G.-B., Y. Shin, S. Will, T. A. Pasquini, C. V. Saba, W. Ketterle, D. E. Pritchard, M. Vengalattore, and M. Prentiss, 2006, "Long phase coherence time and number squeezing of two Bose-Einstein condensates on an atom chip," e-print cond-mat/0608585.

Jones, M. P. A., C. J. Vale, D. Sahagun, B. V. Hall, C. C. Eberlein, B. E. Sauer, K. Furusawa, D. Richardson, and E. A. Hinds, 2003, "Cold atoms probe the magnetic field near a wire," J. Phys. B **37**, L15–L20.

Jones, M. P. A., C. J. Vale, D. Sahagun, B. V. Hall, and E. A. Hinds, 2003, "Spin coupling between cold atoms and the thermal fluctuations of a metal surface," Phys. Rev. Lett. **91**, 080401.

Jorgensen, S., and R. Kosloff, 2003, "Two-pulse atomic coherent control spectroscopy of Eley-Rideal reactions: An application of an atom laser," J. Chem. Phys. **119**, 149–160.

Jorgensen, S., and R. Kosloff, 2004, "Pulse-shaping algorithm of a coherent matter-wave-controlling reaction dynamics," Phys. Rev. A **70**, 015602.

Kagan, Y., E. L. Surkov, and G. V. Shlyapnikov, 1997, "Evolution of a Bose gas in anisotropic time-dependent traps," Phys. Rev. A **55**, R18–R21.

Kasper, A., S. Schneider, H. C. vom Hagen, M. Bartenstein, B. Engeser, T. Schumm, I. Bar-Joseph, R. Folman, L. Feenstra, and J. Schmiedmayer, 2003, "A Bose-Einstein condensate in a microtrap," J. Opt. B: Quantum Semiclassical Opt. **5**, S143–S149.

Ketterle, W., 2002, "Nobel Lecture: When atoms behave as waves: Bose-Einstein condensation and the atom laser," Rev. Mod. Phys. **74**, 1131–1151.

Ketterle, W., and D. E. Pritchard, 1992, "Trapping and focusing ground state atoms with static fields," Appl. Phys. B: Photophys. Laser Chem. **54**, 403–406.

Ketterle, W., and N. J. van Druten, 1996, "Evaporative cooling of atoms," Adv. At., Mol., Opt. Phys. **37**, 181–236.

Key, M., I. G. Hughes, W. Rooijakkers, B. E. Sauer, E. A. Hinds, D. J. Richardson, and P. G. Kazansky, 2000, "Propagation of cold atoms along a miniature magnetic guide," Phys. Rev. Lett. **84**, 1371–1373.

Key, M., W. Rooijakkers, and E. A. Hinds, 2000, "Transport of cold atoms in a miniature guide," New J. Phys. **2**, 25.1–25.6.

Kinoshita, T., T. Wenger, and D. S. Weiss, 2004, "Observation of a one-dimensional Tonks-Girardeau gas," Science **305**, 1125–1128.

Kinoshita, T., T. Wenger, and D. S. Weiss, 2005, "Local pair correlations in one-dimensional Bose gases," Phys. Rev. Lett. **95**, 190406.

Kraft, S., A. Günther, H. Ott, D. Wharam, C. Zimmermann, and J. Fortágh, 2002, "Anomalous longitudinal magnetic field near the surface of copper conductors," J. Phys. B **35**, L469–L474.

Kraft, S., A. Günther, Ph. Wicke, B. Kasch, C. Zimmermann, and J. Fortágh, 2005, "Atom-optical elements on micro chips," Eur. Phys. J. D **35**, 119–123.

Krüger, P., X. Luo, M. W. Klein, K. Brugger, A. Haase, S. Wildermuth, S. Groth, I. Bar-Joseph, R. Folman, and J. Schmiedmayer, 2003, "Trapping and manipulating neutral atoms with electrostatic fields," Phys. Rev. Lett. **91**, 233201.

Kugler, K.-J., W. Paul, and U. Trinks, 1978, "A magnetic storage ring for neutrons," Phys. Lett. **72**, 422–424.

Lau, D. C., A. I. Sidorov, G. I. Opat, R. J. McLean, W. J. Rowlands, and P. Hannaford, 1999, "Reflection of cold atoms from an array of current-carrying wires," Eur. Phys. J. D **5**, 193–199.

Leanhardt, A. E., A. P. Chikkatur, D. Kielpinski, Y. Shin, T. L. Gustavson, W. Ketterle, and D. E. Pritchard, 2002, "Propagation of Bose-Einstein condensates in a magnetic waveguide," Phys. Rev. Lett. **89**, 040401.

Leanhardt, A. E., A. Görlitz, A. P. Chikkatur, D. Kielpinski, Y. Shin, D. E. Pritchard, and W. Ketterle, 2002, "Imprinting vortices in a Bose-Einstein condensate using topological phases," Phys. Rev. Lett. **89**, 190403.

Leanhardt, A. E., T. A. Pasquini, M. Saba, A. Schirotzek, Y. Shin, D. Kielpinski, D. E. Pritchard, and W. Ketterle, 2003, "Cooling Bose-Einstein condensates below 500 picokelvin," Science **301**, 1513–1515.

Leanhardt, A. E., Y. Shin, A. P. Chikkatur, D. Kielpinski, W. Ketterle, and D. E. Pritchard, 2003, "Bose-Einstein condensates near a microfabricated surface," Phys. Rev. Lett. **90**, 100404.

Leanhardt, A. E., Y. Shin, D. Kielpinski, D. E. Pritchard, and W. Ketterle, 2003, "Coreless vortex formation in a spinor Bose-Einstein condensate," Phys. Rev. Lett. **90**, 140403.

Lesanovsky, I., and P. Schmelcher, 2004, "Spectral properties and lifetimes of neutral spin-1/2 fermions in a magnetic guide," Phys. Rev. A **70**, 063604.

Lesanovsky, I., and P. Schmelcher, 2005a, "Selected aspects of the quantum dynamics and electronic structure of atoms in magnetic microtraps," Eur. Phys. J. D **35**, 31–42.

Lesanovsky, I., and P. Schmelcher, 2005b, "Spectral properties and lifetimes of neutral fermions and bosons in a magnetic quadrupole trap," Phys. Rev. A **71**, 032510.

Lesanovsky, I., J. Schmiedmayer, and P. Schmelcher, 2004, "Rydberg atoms in a magnetic guide," Phys. Rev. A **70**, 043409.

Lesanovsky, I., J. Schmiedmayer, and P. Schmelcher, 2005, "Rydberg atoms in a magnetic quadrupole field," J. Phys. B **38**, S151–S170.

Lesanovsky, I., T. Schumm, S. Hofferberth, L. M. Andersson, P. Krüger, and J. Schmiedmayer, 2006, "Adiabatic radio frequency potentials for the coherent manipulation of matter waves," Phys. Rev. A **73**, 033619.

Lesanovsky, I., S. Hofferberth, J. Schmiedmayer, and P. Schmelcher, 2006, "Manipulation of ultracold atoms in dressed adiabatic radio-frequency potentials," Phys. Rev. A **74**, 033619.

Lev, B., 2003, "Fabrication of micro-magnetic traps for cold neutral atoms," Quantum Inf. Comput. **3**, 450–464.

Lev, B., K. Srinivasan, P. Barclay, O. Painter, and H. Mabuchi, 2004, "Feasibility of detecting single atoms using photonic bandgap cavities," Nanotechnology **15**, 556–561.

Lin, Y., I. Teper, C. Cheng, and V. Vuletic, 2004, "Impact of the Casimir-Polder potential and Johnson noise on Bose-Einstein condensate stability near surfaces," Phys. Rev. Lett. **92**, 050404.

Liu, N., W. Gao, and J. Yin, 2002, "Magnetic guiding of cold neutral atoms using a V-shaped current-carrying conductor," Eur. Phys. J. D **19**, 137–145.

Long, R., T. Rom, W. Hänsel, T. W. Hänsch, and J. Reichel, 2005, "Long distance magnetic conveyor for precise positioning of ultracold atoms," Eur. Phys. J. D **35**, 125–133.

Long, R., T. Steinmetz, P. Hommelhoff, W. Hänsel, T. W. Hänsch, and J. Reichel, 2003, "Magnetic microchip traps and single-atom detection," Philos. Trans. R. Soc. London, Ser. A **361**, 1375–1389.

Lovelace, R. V. E., C. Mehanian, T. J. Tommila, and D. M. Lee, 1985, "Magnetic confinement of a neutral gas," Nature (London) **318**, 30–36.

Mabuchi, H., Q. A. Turchette, M. S. Chapman, and H. J. Kimble, 1996, "Real-time detection of individual atoms falling through a high-finesse optical cavity," Opt. Lett. **21**, 1393–1395.

Masuhara, N., J. M. Doyle, J. C. Sandberg, D. Kleppner, T. J. Greytak, H. F. Hess, and G. P. Kochanski, 1988, "Evaporative cooling of spin-polarized atomic hydrogen," Phys. Rev. Lett. **61**, 935–938.

McGuirk, J. M., D. M. Harber, J. M. Obrecht, and E. A. Cornell, 2004, "Alkali-metal adsorbate polarization on conducting and insulating surfaces probed with Bose-Einstein condensates," Phys. Rev. A **69**, 062905.

Migdall, A. L., J. V. Prodan, W. D. Phillips, T. H. Bergeman, and H. J. Metcalf, 1985, "First observation of magnetically trapped neutral atoms," Phys. Rev. Lett. **54**, 2596–2599.

Moerdijk, A. J., H. M. J. M. Boesten, and B. J. Verhaar, 1996, "Decay of trapped ultracold alkali atoms by recombination," Phys. Rev. A **53**, 916–920.

Mohring, B., M. Bienert, F. Haug, G. Morigi, W. P. Schleich, and M. G. Raizen, 2005, "Extracting atoms on demand with lasers," Phys. Rev. A **71**, 053601.

Müller, D., D. Z. Anderson, R. J. Grow, P. D. D. Schwindt, and E. A. Cornell, 1999, "Guiding neutral atoms around curves with lithographically patterned current-carrying wires," Phys. Rev. Lett. **83**, 5194–5197.

Müller, D., E. A. Cornell, M. Prevedelli, P. D. D. Schwindt, W. Ying-Ju, and D. Z. Anderson, 2001, "Magnetic switch for integrated atom optics," Phys. Rev. A **63**, 041602.

Müller, D., E. A. Cornell, M. Prevedelli, P. D. D. Schwindt, A. Zozulya, and D. Z. Anderson, 2000, "Waveguide atom beam splitter for laser-cooled neutral atoms," Opt. Lett. **25**, 1382–1384.

Münstermann, P., T. Fischer, P. W. H. Pinkse, and G. Rempe, 1999, "Single slow atoms from an atomic fountain observed in a high-finesse optical cavity," Opt. Commun. **159**, 63–67.

Obrecht, J. M., R. J. Wild, M. Antezza, L. P. Pitaevskii, S. Stringari, and E. A. Cornell, 2006, "Measurement of the temperature dependence of the Casimir-Polder force," e-print cond-mat/0608074.

Olshanii, M., 1998, "Atomic scattering in the presence of an external confinement and a gas of impenetrable bosons," Phys. Rev. Lett. **81**, 938–941.

Olshanii, M., and V. Dunjko, 2005, "Interferometry in dense nonlinear media and interaction-induced loss of contrast in microfabricated atom interferometers," e-print cond-mat/0505358.

Opat, G. I., S. J. Wark, and A. Cimmino, 1992, "Electric and magnetic mirrors and gratings for slowly moving neutral atoms and molecules," Appl. Phys. B: Photophys. Laser Chem. **54**, 396–402.

Ott, H., J. Fortágh, S. Kraft, A. Günther, D. Komma, and C. Zimmermann, 2003, "Nonlinear dynamics of a Bose-Einstein condensate in a magnetic waveguide," Phys. Rev. Lett. **91**, 040402.

Ott, H., J. Fortágh, G. Schlotterbeck, A. Grossmann, and C. Zimmermann, 2001, "Bose-Einstein condensation in a surface microtrap," Phys. Rev. Lett. **87**, 230401.

Ott, H., J. Fortágh, and C. Zimmermann, 2003, "Dynamics of a Bose-Einstein condensate in an anharmonic trap," J. Phys. B **36**, 2817–2822.

Öttl, A., S. Ritter, M. Köhl, and T. Esslinger, 2005, "Correlations and counting statistics of an atom laser," Phys. Rev. Lett. **95**, 090404.

Paredes, B., A. Widera, V. Murg, O. Mandel, S. Fölling, I. Cirac, G. V. Shlyapnikov, T. W. Hänsch, and I. Bloch, 2004, "Tonks-Girardeau gas of ultracold atoms in an optical lattice," Nature (London) **429**, 277–281.

Pasquini, T. A., M. Saba, G. Jo, Y. Shin, W. Ketterle, and D. E. Pritchard, 2006, "Low velocity quantum reflection of Bose-Einstein condensates," e-print cond-mat/0603463.

Pasquini, T. A., Y. Shin, C. Sanner, M. Saba, A. Schirotzek, D. E. Pritchard, and W. Ketterle, 2004, "Quantum reflection from a solid surface at normal incidence," Phys. Rev. Lett. **93**, 223201.

Paul, W., 1990, "Electromagnetic traps for charged and neutral particles," Rev. Mod. Phys. **62**, 531–540.

Paul, T., P. Leboeuf, N. Pavloff, K. Richter, and P. Schlagheck, 2005, "Nonlinear resonant transport of Bose-Einstein condensates through waveguides with disorder," Phys. Rev. A **72**, 063621.

Paul, T., K. Richter, and P. Schlagheck, 2005, "Nonlinear resonant transport of Bose-Einstein condensates," Phys. Rev. Lett. **94**, 020404.

Pron'ko, G. P., and Y. Stroganov, 1977, "A new example of the quantum mechanical problem involving latent symmetry," Zh. Eksp. Teor. Fiz. **72**, 2048–2054.

Purcell, E. M., 1946, "Spontaneous emission probabilities at radio frequencies," Phys. Rev. **69**, 681.

Reichel, J., 2002, "Microchip traps and Bose-Einstein condensation," Appl. Phys. B: Lasers Opt. **74**, 469–487.

Reichel, J., W. Hänsel, and T. W. Hänsch, 1999, "Atomic micromanipulation with magnetic surface traps," Phys. Rev. Lett. **83**, 3398–3401.

Reichel, J., W. Hänsel, P. Hommelhoff, and T. W. Hänsch, 2001, "Applications of integrated magnetic microtraps," Appl. Phys. B: Lasers Opt. **72**, 81–89.

Reichel, J., and J. H. Thywissen, 2004, "Using magnetic chip traps to study Tonks-Girardeau quantum gases," J. Phys. IV **116**, 265–274.

Rekdal, P. K., S. Scheel, P. L. Knight, and E. A. Hinds, 2004, "Thermal spin flips in atom chips," Phys. Rev. A **70**, 013811.

Richmond, J. A., B. P. Cantwell, S. N. Chormaic, D. C. Lau, A. M. Akulshin, and G. I. Opat, 2002, "Magnetic guide for neutral atoms," Phys. Rev. A **65**, 033422.

Rooijakkers, W., 2004, "Mapping a cloud of ultra-cold atoms onto a miniature storage ring," Appl. Phys. B: Lasers Opt. **78**, 719–724.

Rosenbusch, P., B. V. Hall, I. G. Hughes, C. V. Saba, and E. A. Hinds, 2000a, "Manipulation of cold atoms by an adaptable magnetic reflector," Appl. Phys. B: Lasers Opt. **70**, 709–720.

Rosenbusch, P., B. V. Hall, I. G. Hughes, C. V. Saba, and E. A. Hinds, 2000b, "Manipulation of cold atoms using a corrugated magnetic reflector," Phys. Rev. A **61**, 031404.

Rubbmark, J. R., M. M. Kash, M. G. Littman, and D. Kleppner, 1981, "Dynamical effects at avoided level crossings: A study of the Landau-Zener effect using Rydberg atoms," Phys. Rev. A **23**, 3107–3117.

Scheel, S., P. K. Rekdal, P. L. Knight, and E. A. Hinds, 2005, "Atomic spin decoherence near conducting and superconducting films," Phys. Rev. A **72**, 042901.

Schmiedmayer, J., 1992, unpublished.

Schmiedmayer, J., 1995a, "A wire trap for neutral atoms," Appl. Phys. B: Lasers Opt. **60**, 169–179.

Schmiedmayer, J., 1995b, "Guiding and trapping a neutral atom on a wire," Phys. Rev. A **52**, R13–R16.

Schmiedmayer, J., R. Folman, and T. Calarco, 2002, "Quantum information processing with neutral atoms on an atom chip," J. Mod. Opt. **49**, 1375–1388.

Schneider, S., A. Kasper, C. Hagen, M. Bartenstein, B. Engeser, T. Schumm, I. Bar-Joseph, R. Folman, L. Feenstra, and J. Schmiedmayer, 2003, "Bose-Einstein condensation in a simple microtrap," Phys. Rev. A **67**, 023612.

Schroll, C., W. Belzig, and C. Bruder, 2003, "Decoherence of cold atomic gases in magnetic microtraps," Phys. Rev. A **68**, 043618.

Schumayer, D., and B. Apagyi, 2004, "Stability of static solitonic excitations of two-component Bose-Einstein condensates in finite range of interspecies scattering length a_{12}," Phys. Rev. A **69**, 043620.

Schumm, T., J. Estève, C. Figl, J.-B. Trebbia, C. Aussibal, H. Nguyen, D. Mailly, I. Bouchoule, C. I. Westbrook, and A. Aspect, 2005, "Atom chips in the real world: The effect of wire corrugation," Eur. Phys. J. D **32**, 171–180.

Schumm, T., S. Hofferberth, L. M. Andersson, S. Wildermuth, S. Groth, I. Bar-Joseph, J. Schmiedmayer, and P. Kruger, 2005, "Matter-wave interferometry in a double well on an atom chip," Nat. Phys. **1**, 57–62.

Schwindt, P. D. D., E. A. Cornell, T. Kishimoto, W. Ying-Ju, and D. Z. Anderson, 2005, "Efficient loading of a magnetic waveguide on an atom chip," Phys. Rev. A **72**, 023612.

Scott, R. G., A. M. Martin, T. M. Fromhold, and F. W. Sheard, 2005, "Anomalous quantum reflection of Bose-Einstein condensates from a silicon surface: The role of dynamical excitations," Phys. Rev. Lett. **95**, 073201.

Shevchenko, A., T. Lindvall, I. Tittonen, and M. Kaivola, 2004, "Microscopic electrooptical atom trap on an evanescent-wave mirror," Eur. Phys. J. D **28**, 273–276.

Shimizu, F., 2001, "Specular reflection of very slow metastable neon atoms from a solid surface," Phys. Rev. Lett. **86**, 987–990.

Shimizu, F., and J. Fujita, 2002a, "Giant quantum reflection of neon atoms from a ridged silicon surface," J. Phys. Soc. Jpn. **71**, 5–8.

Shimizu, F., and J. I. Fujita, 2002b, "Reflection-type hologram for atoms," Phys. Rev. Lett. **88**, 123201.

Shin, Y., G.-B. Jo, M. Saba, T. A. Pasquini, W. Ketterle, and D. E. Pritchard, 2005, "Optical weak link between two spatially separated Bose-Einstein condensates," Phys. Rev. Lett. **95**, 170402.

Shin, Y., M. Saba, T. A. Pasquini, W. Ketterle, D. E. Pritchard, and A. E. Leanhardt, 2004, "Atom interferometry with Bose-Einstein condensates in a double-well potential," Phys. Rev. Lett. **92**, 050405.

Shin, Y., M. Saba, A. Schirotzek, T. A. Pasquini, A. E. Leanhardt, D. E. Pritchard, and W. Ketterle, 2004, "Distillation of Bose-Einstein condensates in a double-well potential," Phys. Rev. Lett. **92**, 150401.

Shin, Y., M. Saba, M. Vengalattore, T. A. Pasquini, C. Sanner, A. E. Leanhardt, M. Prentiss, D. E. Pritchard, and W. Ketterle, 2004, "Dynamical instability of a doubly quantized vortex in a Bose-Einstein condensate," Phys. Rev. Lett. **93**, 160406.

Shin, Y., C. Sanner, G.-B. Jo, T. A. Pasquini, M. Saba, W. Ketterle, D. E. Pritchard, M. Vengalattore, and M. Prentiss, 2005, "Interference of Bose-Einstein condensates split with an atom chip," Phys. Rev. A **72**, 021604.

Silber, C., S. Günther, C. Marzok, B. Deh, P. W. Courteille, and C. Zimmermann, 2005, "Quantum-degenerate mixture of fermionic lithium and bosonic rubidium gases," Phys. Rev. Lett. **95**, 170408.

Sinclair, C. D. J., E. A. Curtis, I. Llorente-Garcia, J. A. Retter, B. V. Hall, S. Ericson, and E. A. Hinds, 2005, "Bose-Einstein condensation on a permanent-magnet atom chip," e-print physics/0503619.

Skagerstam, B.-S., U. Hohenester, A. Eiguren, and P. K. Rekdal, 2006, "Spin decoherence in superconducting atom chips," Phys. Rev. Lett. **97**, 070401.

Söding, J., D. Guery-Odelin, P. Desbiolles, F. Chevy, H. Inamori, and J. Dalibard, 1999, "Three-body decay of a rubidium Bose-Einstein condensate," Appl. Phys. B: Lasers Opt. **69**, 257–261.

Sorensen, A. S., C. H. van der Wal, L. I. Childress, and M. D. Lukin, 2004, "Capacitive coupling of atomic systems to mesoscopic conductors," Phys. Rev. Lett. **92**, 063601.

Spreeuw, R. J. C., C. Gerz, L. S. Goldner, W. D. Phillips, S. L. Rolston, C. I. Westbrook, M. W. Reynolds, and I. F. Silvera, 1994, "Demonstration of neutral atom trapping with microwaves," Phys. Rev. Lett. **72**, 3162–3165.

Stickney, J. A., and A. A. Zozulya, 2002, "Wave-function recombination instability in cold-atom interferometers," Phys.

Rev. A **66**, 053601.

Stickney, J. A., and A. A. Zozulya, 2003, "Influence of nonadiabaticity and nonlinearity on the operation of cold-atom beam splitters," Phys. Rev. A **68**, 013611.

Stickney, J. A., and A. A. Zozulya, 2004, "Decrease in the visibility of the interference fringes in a cold-atom accelerometer," Phys. Rev. A **69**, 063611.

Sukenik, C. I., M. G. Boshier, S. Cho, V. Sandoghdar, and E. A. Hinds, 1993, "Measurement of the Casimir-Polder force," Phys. Rev. Lett. **70**, 560–563.

Sukumar, C. V., and D. M. Brink, 1997, "Spin-flip transitions in a magnetic trap," Phys. Rev. A **56**, 2451–2454.

Teper, I., Y.-J. Lin, and V. Vuletic, 2006, "Resonator-aided single-atom detection on a microfabricated chip," e-print cond-mat/0603675.

Thywissen, J. H., M. Olshanii, G. Zabow, M. Drndic, K. S. Johnson, R. M. Westervelt, and M. Prentiss, 1999, "Microfabricated magnetic waveguides for neutral atoms," Eur. Phys. J. D **7**, 361–367.

Treutlein, P., P. Hommelhoff, T. Steinmetz, T. W. Hänsch, and J. Reichel, 2004, "Coherence in microchip traps," Phys. Rev. Lett. **92**, 203005.

Trupke, M., E. A. Hinds, S. Erikson, E. A. Curtis, Z. Moktadir, E. Kukharenka, and M. Kraft, 2005, "Microfabricated high-finesse optical cavity with open access and small volume," Appl. Phys. Lett. **87**, 211106.

Vale, C. J., B. Upcroft, M. J. Davis, N. R. Heckenberg, and H. Rubinsztein-Dunlop, 2004, "Foil-based atom chip for Bose-Einstein condensates," J. Phys. B **37**, 2959–2967.

Varpula, T., and T. Poutanen, 1984, "Magnetic field fluctuations arising from thermal motion of electric charge in conductors," J. Appl. Phys. **55**, 4015–4021.

Vuletic, V., T. Fischer, M. Praeger, T. W. Hänsch, and C. Zimmermann, 1998, "Microscopic magnetic quadrupole trap for neutral atoms with extreme adiabatic compression," Phys. Rev. Lett. **80**, 1634–1637.

Wang, D.-W., M. D. Lukin, and E. Demler, 2004, "Disordered Bose-Einstein condensates in quasi-one-dimensional magnetic microtraps," Phys. Rev. Lett. **92**, 076802.

Wang, Y.-J., D. Z. Anderson, V. M. Bright, E. A. Cornell, Q. Diot, T. Kishimoto, M. Prentiss, R. A. Saravanan, S. R. Segal, and W. Saijun, 2005, "Atom Michelson interferometer on a chip using a Bose-Einstein condensate," Phys. Rev. Lett. **94**, 090405.

Weiner, J., V. S. Bagnato, S. Zilio, and P. S. Julienne, 1999, "Experiments and theory in cold and ultracold collisions," Rev. Mod. Phys. **71**, 1–85.

Weinstein, J. D., and K. G. Libbrecht, 1995, "Microscopic magnetic traps for neutral atoms," Phys. Rev. A **52**, 4004–4009.

Whitlock, N. K., and I. Bouchoule, 2003, "Relative phase fluctuations of two coupled one-dimensional condensates," Phys. Rev. A **68**, 053609.

Wildermuth, S., S. Hofferberth, I. Lesanovsky, S. Groth, I. Bar-Joseph, P. Krüger, and J. Schmiedmayer, 2005, "Sensing electric and magnetic fields with Bose-Einstein Condensates," e-print cond-mat/0512520.

Wildermuth, S., S. Hofferberth, I. Lesanovsky, E. Haller, L. M. Andersson, S. Groth, I. Bar-Joseph, P. Krüger, and J. Schmiedmayer, 2005, "Bose-Einstein condensates microscopic magnetic-field imaging," Nature (London) **435**, 440–490.

Wonneberger, W., 2001, "Luttinger-model approach to interacting one-dimensional fermions in a harmonic trap," Phys. Rev. A **63**, 063607.

Xianlong, G., F Gleisberg, F. Lochmann, and W. Wonneberger, 2003, "Treatment of backscattering in a gas of interacting fermions confined to a one-dimensional harmonic atom trap," Phys. Rev. A **67**, 023610.

Xianlong, G., and W. Wonneberger, 2002, "Two-component Fermi gas in a one-dimensional harmonic trap," Phys. Rev. A **65**, 033610.

Xianlong, G., and W. Wonneberger, 2004, "Phase theory and critical exponents for the Tomonaga-Luttinger model with harmonic confinement," J. Phys. B **37**, 2363–2377.

Xu, L. F., J. P. Yin, and Y. Z. Wang, 2001, "A proposal for guiding and trapping of cold atoms in the AC field of current-carrying wires," J. Chin. Chem. Soc. (Taipei) **48**, 549–553.

Yan, Z.-C., A. Dalgarno, and J. F. Babb, 1997, "Long-range interactions of lithium atoms," Phys. Rev. A **55**, 2882–2887.

Zobay, O., and B. M. Garraway, 2000, "Controllable double waveguide for atoms," Opt. Commun. **178**, 93–101.

Zobay, O., and B. M. Garraway, 2001, "Two-dimensional atom trapping in field-induced adiabatic potentials," Phys. Rev. Lett. **86**, 1195–1198.

Zobay, O., and B. M. Garraway, 2004, "Atom trapping and two-dimensional Bose-Einstein condensates in field-induced adiabatic potentials," Phys. Rev. A **69**, 023605.